POLITECNICO DI MILANO

Facoltà di Ingegneria Industriale

Corso di Laurea in
Ingegneria Aeronautica

Buckling analyses of composite laminated panels with delamination

Relatrice: Prof. Chiara BISAGNI

Tesi di Laurea di:
David ALBIOL Matr. 706811

Anno Accademico 2009-2010

als meus pares, Manel i Mercè,
i a la meva germana, Olga.

Abstract

Buckling response of composite laminated panels with an artificial delamination was numerically investigated.

Implementation of the finite-element models required a previous study on the simulation of fracture mechanisms under general mixed-mode loading conditions with the use of cohesive elements. To pursue this aim, a methodology based on numerical analyses and parametric studies of the DCB (Double Cantilever Beam) and ENF (End Notched Flexure) tests on AS4/PEEK laminates was developed. Comparison to available experimental data enabled to determine a reduced set of parameters which, controlling the response of cohesive elements and the variable discretization pattern over the model, provided a good compromise between accuracy and computational cost in both single-mode delamination cases.

Validation of the obtained set of parameters took place through the simulation of the MMB (Mixed-Mode Bending) test at three different mode ratios. Good agreement with experimental measurements found in literature suggested extending the usage of the found set in more complex problems, such as delamination buckling of a damaged HTA/6376C plate, whose fracture-related properties are comparable to those of AS4/PEEK. Through a careful definition of the geometric imperfection, the adopted nonlinear static approach showed to yield predictions of the failure load in good agreement with experimental results reported in literature.

Finally, a qualitative study was conducted about the reduction of compressive strength caused by delaminations of different sizes, shapes and through-the-thickness locations within an AS4/PEEK panel. Conclusions showed to be consistent with similar previous works conducted by other authors, evidencing a reduction of the compressive strength with the delamination size and depth. On the contrary, no significant influence of the delamination shape (circular or square) was observed.

Keywords: delamination, buckling, composite laminated panels, cohesive elements, compressive strength.

Sommario

Il presente lavoro di tesi riguarda l'analisi numerica del fenomeno del buckling in laminati piani in composito danneggiati.

La simulazione dei meccanismi di frattura in prossimità del fronte di delaminazione è stata affrontata tramite l'impiego di elementi coesivi sull' interfaccia interlaminare complanare allo scollamento. La messa a punto dei modelli ad elementi finiti per la corretta simulazione del danneggiamento progressivo e l'avanzamento della delaminazione in generiche condizioni di modo misto ha richiesto un'attenta taratura del modello coesivo così come un'opportuna definizione della discretizzazione spaziale. A questo scopo, è stata impostata una procedura fondata sulla realizzazione di simulazioni numeriche ed analisi parametriche delle prove DCB (*Double Cantilever Beam*) ed ENF (*End Notched Flexure*) su provini in AS4/PEEK. Le analisi di sensitività sono state eseguite per le seguenti variabili: rigidezza iniziale degli elementi coesivi (*penalty stiffness*), dissipazione viscosa introdotta al fine di risolvere i problemi di convergenza presenti nei materiali a comportamento *softening*, dimensione degli elementi all'interno della zona di processo lungo la direzione di propagazione della delaminazione e rateo di transizione della densità della mesh attraverso i limiti della zona di processo. I modelli sono stati approntati attraverso il confronto dei risultati dei diversi studi parametrici con i dati sperimentali reperiti in letteratura, cercando di giungere ad un giusto compromesso tra accuratezza e costo computazionale.

La validazione del set di parametri ottenuto è avvenuta sulla base della simulazione della prova MMB (*Mixed-Mode Bending*) per tre rapporti di modo misto differenti, selezionati in modo da coprire lo spettro di possibili modalità di delaminazione tra il modo I puro ed il modo II puro. La buona corrispondenza mostrata con i valori sperimentali riscontrati in letteratura ha determinato l'utilizzo di tale set in problemi di natura più complessa, quale il *delamination buckling* di una piastra in HTA/6376C. Essendo le sue proprietà paragonabili a quelle dell'AS4/PEEK, ci si è avvalsi del medesimo modello di frattura per modellarne i meccanismi di delaminazione. La validità di questa scelta è stata confermata dal buon riscontro evidenziato tra il carico di collasso previsto dalle analisi statiche non lineari ed il valore sperimentale disponibile in letteratura, frutto anche di una curata definizione delle imperfezioni geometriche.

Infine, si è condotto uno studio qualitativo sulla reduzione della resistenza a compressione dovuta alla presenza di delaminazoni di dimensioni, forme e profondità diverse all'interno di un pannello in AS4/PEEK. Le conclusioni emerse da queste indagini si sono rivelate in linea con i risultati ottenuti in lavori precedenti svolti da altri autori, evidenziando una diminuzione della resistenza a compressione all'aumentare della dimensione e della profondità del danneggiamento. Al contrario, l'influenza della forma della delaminazione, circolare o quadrata, appare trascurabile.

Parole chiavi: delaminazione, buckling, pannelli in composito, elementi coesivi, resistenza a compressione.

Contents

List of Figures

List of Tables

Nomenclature

Chapter 2

a = crack length;

d = damage variable;

$\mathbf{f}$ = nodal load vector;

m = mode mixity ratio;

s = element width at the delamination front;

$u_i^{-/+}$ = global displacement of the top and bottom surfaces, respectively;

$\mathbf{x}$ = current position vector of a pint on the element middle surface;

$\mathbf{B}$ = tensor relating relative displacements to nodal displacements;

$\mathbf{D}$ = constitutive tensor of the cohesive element;

G = energy release rate;

G_I = mode I energy release rate;

$G_{\mathbf{II}}$ = mode II energy release rate;

$G_{\mathbf{III}}$ = mode III energy release rate;

G_C = critical energy release rate;

$G_{\mathbf{IC}}$ = mode I critical energy release rate;

$G_{\mathbf{IIC}}$ = mode II critical energy release rate;

$G_{\mathbf{IIIC}}$ = mode III critical energy release rate;

$G_{\mathbf{shear}}$ = shear mode energy release rate;

G_T = total energy release rate;

K_p = penalty stiffness;

N = interlaminar normal tensile strength;

N_k = standard Lagrangian shape functions;

$\overline{N_k}$ = element interpolation functions;

S = interlaminar sliding shear strength;

T = interlaminar scissoring shear strength;

$\mathbf{X}$ = initial position vector of a pint on the element middle surface;

β = mode ratio;

δ = separation or relative displacement (single-mode);

δ^0 = separation at damage onset (single-mode);

δ^f = separation at failure of the cohesive element (single-mode);

δ_m = equivalent separation (mixed-mode);

$\delta_m^{\mathbf{max}}$ = maximum equivalent separation (mixed-mode);

δ_m^0 = equivalent separation at damage onset (mixed-mode);

$\delta_{\mathbf{shear}}$ = total tangential separation;

$\overline{\delta_{\mathbf{sr}}}$ = Kroenecker delta;

μ = parameter in the B-K criterion;

τ = tractions;

τ^0 = tractions at damage onset;

Γ = middle surface of the cohesive element;

Δ_i = global separation between the top and bottom element surfaces;

ΔA = virtually closed area;

Θ = coordinate transformation tensor;

Chapters 3 to 7

a_0 = initial crack length;

b = specimen width ;

c = length of the lever;

e = length of the cohesive zone region (DCB, ENF and MMB models);

fc = ratio between mesh density in the cohesive zone region and the adjacent regions;

h = distance from the top surface to the delamination;

$l_{\mathbf{cz}}$ = lenght of the cohesive damaged zone;

$l_{\mathbf{czI}}$ = length of the cohesive damaged zone for fracture under pure mode I;

$l_{\mathbf{czII}}$ = length of the cohesive damaged zone for fracture under pure mode II;

$l_{\mathbf{eI}}$ = estimated suitable element size within the cohesive zone region for delamination under pure mode I;

$l_{\mathbf{eII}}$ = estimated suitable element size within the cohesive zone region for delamination under pure mode II;

n = number of experimentally determined fracture toughnesses at mode ratios different than 0 and 1;

$size$ = element size within the cohesive zone region along the fracture propagation direction;

t = specimen thickness;

u = x component of the displacement vector;

v = y component of the displacement vector;

v_e = vertical displacement at the end loaded edge of the DCB specimen;

$v_{\mathbf{lever}}$ = vertical displacement at the load-point of the MMB specimens;

v_m = vertical displacament at the midpoint of the ENF specimen ;

w = z component of the displacement vector;

A = unsupported area of the panels;

A_d = initial damaged area of the panels;

C = compliance;

$E_{\mathbf{ii}}$ = Young's modulus in the ii direction;

$G_{\mathbf{ij}}$ = ij component of the shear modulus;

L = half length of the specimen;

M = parameter that depends on the cohesive zone model theory used to estimate a suitable element size within the cohesive zone region;

N_e = requested minimum number of elements within the cohesive damaged zone;

P = applied load in the DCB, ENF and MMB tests/simulations;

$P_{\mathbf{growth}}$ = load at the onset of delamination growth;

$P_{\mathbf{GB}}$ = global buckling load;

$P_{\mathbf{LB}}$ = local buckling load;

$P_{\mathbf{MAX}}$ = maximum load;

$\overline{U}$ = prescribed displacement rate along the x-direction;

V = height of the loading point above the pivot point in the MMB test;

$\overline{V}$ = prescribed displacement rate along the y-direction;

$\delta_{\mathbf{DCB}}$ = opening displacement in the DCB test/simulation;

ϵ = error committed by the least-square curve;

θ_z = rotation around z-axis;

λ = eigenvalues (displacements) associated to the global buckling eigenmodes;

μ = viscous regularization factor;

$\nu_{\mathbf{ij}}$ = ij component of the Poisson ratio;

χ = crack length correction factor;

Γ = transverse modulus correction parameter;

Appendix A

$n_{\mathbf{BE}}$ = position of the back echo peak within the vector containing the sample points of a generic acquired signal;

$s_{\mathbf{US}}$ = distance of the discontinuity surface from the US probe;

SR = sampling rate;

$V_{\mathbf{US}}$ = propagation speed of ultrasonic waves within the material;

List of acronyms

4ENF Four-Point End Notched Flexure;

ASTM American Society for Testing and Materials;

BVD Barely Visible Damage;

CBT Classical Beam Theory;

CC Compliance Calibration;

CFRP Carbon Fiber Reinforced Plastic;

CZM Cohesive Zone Model;

DCB Double Cantilever Beam;

EDT Energy Derivative Technique;

ELS End Loaded Split;

ENF End Notched Flexure;

LEFM Linear Elastic Fracture Mechanics;

LVDT Linearly Variable Displacement Transducer;

MAC Modal Assurance Criterion;

MBT Modified Beam Theory;

MMB Mixed-Mode Bending;

NCF Non Crimp Fabric;

NDT Non Destructive Testing;

ONF Over Notched Flexure;

PEEK Polyetheretherketone;

TOF Time-Of-Flight;

UD Unidirectional;

US Ultrasonic;

VCCT Virtual Crack Closure Technique;

Chapter 1

Introduction

This Chapter provides a general overview on complex phenomena that characterize fracture of composite materials, focusing on delaminations and their interaction with the buckling response.

A solid comprehension of these topics is of particular interest, since it will allow developing enhanced numerical design tools that will eventually consent to fully exploit the potential gainings offered by composites in comparison to light metal alloys.

1.1 Damage in composite structures

1.1.1 General overview

In recent years, the use of composite materials, particularly advanced CFRPs (Carbon Fiber Reinforced Plastics), is rapidly increasing in structural components of aircrafts, such as Airbus 380, Boeing 787 (Figure 1.1 [1]) and coming Airbus 350.

The reasons for this are, in the first place, their superior specific mechanical properties under static and fatigue in-plane loadings, namely higher strength-to-weight and stiffness-to-weight ratios as compared with metal alloys traditionally used in the aerospace industry. Furthermore, CFRPs exhibit improved corrosion and environmental resistance, great design flexibility and potential reduction of processing, fabrication and life cycle costs. As a result, extensive usage of composite materials instead of light alluminium allowys may significantly contribute to reduce both developing and operating costs: indeed, aeronautical industry expectations are of a 20% reduction in the short period and, even, of a 50% reduction in the long one [2].

In spite of having these advantages, the poor properties in the thickness direction make composites particularly susceptible to damage under transverse low velocity impacts. This damage can arise because of dropped tools during manufacturing and maintenance operations, due to parts being hit

by runway debris propelled by the tires or by flying though hailstorms and can seriously degrade the buckling stability and compressive strength of the laminate. Embedded manufacturing defects, in-service cyclic loads and environmental conditions may promote further damage initiation and evolution, which can eventually lead to catastrophic loss of load-carrying capacity of the component.

Figure 1.1: Boeing 787: the world's first major airliner to use composite materials for most of its construction.

Since the effect of damage upon mechanical properties of composite laminates is still not fully understood, current composite design tends to be conservative for primary airframe structures under predominantly compressive loads. As a result, most of the weight-saving potential is yet to be fully explored. Consequently, widespread use of composites in primary structural applications will be postponed until further understanding of the fracture response of CRFPs is gained.

At this purpose, experimental tests can be carried out not only to furtherly investigate the delamination phenomenon but also to provide reference data to aid the development and validation of numerical models. Indeed, large costs associated to mechanical tests to real-size components make it unfeasible to rely all the investigation on experimental testing. Furthermore, panel failure is often a sudden event with little or no propagation of damage prior to failure. Studying the mechanisms involved from experimental data alone is therefore difficult.

Hence,the availability of reliable numerical tools to accurately predict damage onset and propagation in composite materials has become more and more important. Once validated against experimental data, in fact, numerical models can be used to simulate the structural response under

any condition expected to encounter during the service life, thus reducing design and certification costs, as well as to implement complex optimization methodologies to achieve optimum designs of damage tolerant high performance composite components. Moreover, a deeper understanding of residual mechanical properties after sub-critical damage occurance by means of numerical assessment may allow engineers to schedule more accurate mantenaince and replacement programs, ensuring structural integrity during in-between inspections periods.

Summarizing, experimental testing together with numerical simulation may enable to take full advantage of the weight-saving potential of CFRPs in coming years and, as a result, a significant reduction in fuel consumption and air contaminant emissions per passenger may be achieved as well.

1.1.2 Failure mechanisms in composite materials

In contrast to metals, where fracture under static loading is known to result from the nucleation or initiation and subsequent growth of a single dominant flaw, the fracture of fiber reinforced composite laminates is quite complex and characterized by the initiation and progression of multiple failure modes. The usual failure mechanisms can be divided into:

- Fiber failure modes: tensile fracture and local buckling and kinking in compression.
- Matrix failure modes: transverse, longitudinal and angle-ply cracking and polymer degradation due to environmental causes such as radiation, temperature or moisture uptake.
- Fiber-matrix debonding.
- Interlaminar interface failure: delamination between adjacent plies.

The kinds of damage mechanisms occurring, their distribution and their possible interactions are dependent on many parameters, such as the properties of the fiber/matrix system, the curing process, the stacking sequence of the laminate or the environmental conditions.

1.2 Introduction to delamination

In this work, attention is focused on delaminations or interlaminar cracks, which are one of the predominant forms of failure in laminated fiber-reinforced composites due to their relatively weak interlaminar strengths.

Particularly, impact-induced delaminations are investigated as they may reduce severely the structural integrity without being detected. Special attention is given to their effect upon the post-buckling response and compressive strength of a composite panel.

1.2.1 Causes of delamination

Delaminations may arise during any moment of the manufacturing process or service life under various circumstances:

- *Geometric discontinuities.*

  The stress gradients that occur near abrupt changes of section, such as ply drop-offs, unions between stiffeners and thin plates, free edges, and bonded and bolted joints and access holes promote delamination initiation and trigger intraply damage mechanisms.

  In a laminate consisting of a number of plies in various orientations, the plies provide mutual restraint against Poisson's deformations and provide interlaminar shearing stresses, as well as normal stresses, in the thickness direction. This interlaminar load transfer occurs at boundaries and specimen edges and can cause delamination [3].

- *Curved sections.*

  In curved segments, tubular sections, cylinders, spheres and pressurized containers the normal and shear stresses at the interface of two adjacent plies can originate the loss of adhesion and the onset of an interlaminar crack [4].

- *Hygrothermal in-service effects.*

  Different thermal expansivities of matrix and reinforcement result in mechanical stresses that can be a source of delamination as environmental temperature changes.

  Likewise, anisotropic dimensional response of the laminas due to absorption of moisture might be a cause of interlaminar cracks. Plasticization of the polymeric matrix and chemical deterioration of the constituent materials due to interaction with penetrating water may inflict further damage such as matrix crazes or cracks [5].

- *Poor manufacturing process.*

  Delamination may originate during the manufacturing stage due to a disuniform resin distribution or to the presence of embedded voids

resulting from poor practices when laying the plies. Residual stresses can also be induced by differential shrinkage of the constituents upon cooling from curing temperature to room temperature. For thermoset matrix composites, the extend of matrix shrinkage is associated to the curing reaction; for thermoplastic matrix composites, it depends on the degree of crystallinity achieved as the molten polymer is cooled [6].

- *Low velocity impacts.*

  Transverse concentrated loads caused by low energy impacts, such as a dropped tool during maintenance or propelled runway debris during take-off or landing, can originate interlaminar debonding between adjacent plies with different fiber orientations.

1.2.2 Delaminations caused by impact

Impact-induced delaminations are initiated due to interaction of matrix cracks and the resin-rich area along ply interface resulting, in general, in a complex damage pattern including multiple delamination, fiber breakage and matrix cracks.

Impact tests show that the majority of damage occur towards the rear surface of the specimen [7]: the area of the delaminations increases through the thickness away from the point of impact and significant matrix cracking develops on the back face. Due to the nature of aircraft structures though, the back face is often in an area that is not easily accessible and this cracking pattern cannot be visually detected.

As for delaminations caused by impact, they are classified as BVD (Barely Visible Damage), since they arise underneath the surface of the laminate and are not easily detectable during maintenance tasks. This explains why impact damage is of such concern in designing composite structures, since undetected subsurface delamination can lead to catastrophic failures without any external signs.

Shape of the various delaminations originated as a consequence of an impact is complex and depends upon the specimen geometry, the material properties and the impact energy. Even though, not all impact-induced damage mechanisms are active in the same way and simplified delamination geometries can be assumed when simulating embedded damage in tests [7] and in finite element analyses. Indeed, delamination area is normally simplified to be square [7], circular [8] or ellyptical [9] in order to offer a compromise between realistic representation of the geometry of the actual delaminations and ease of manufacturing of artificial damage.

Implanting non adhesive inserts of known shape and position into the specimens, the effect of delamination geometry on mechanical properties can be studied in a controlled manner.

Focusing back on numerical procedures, the definition of the interlaminar crack geometry is much simpler with artificial delaminations, and reliable results can be obtained by performing relatively straightforward analyses with single or multiple delaminations through the thickness of the specimen.

In the series of studies presented in this work only the simplest case was considered: impact-induced damage was in fact represented as a rectangular or circular single delamination.

1.2.3 Delamination buckling

Delaminations can cause a significant reduction in the compressive strength of a composite structure. Drastic reduction in bending stiffness is also observed and, when compressive loads are present, interlaminar cracks may promote local buckling of the thinnest sub-laminate. Once buckling occurs, interlaminar debonding might extend and further decrease the load-carrying capacity of the structure.

Fuselage panels and upper wing skins are examples of composite components particularly susceptible to buckling due to in-service compressive and shear loads. To fully exploit the weight saving potential of composite materials in such aerostructures, hence, accurate knowledge of the post-buckling behavior must be achieved as well, to ensure structural integrity in the postbuckling regime. Disregarding the presence of damage, engineers are still reluctant to furtherly explore the possibilities offered by CFRPs because of the complexity of their response in the nonlinear range, and particularly in the post-buckling field, in which non-linearities play a dominant role [10].

Delamination buckling consists in the complex interaction between embedded delaminations and buckling and postbuckling response that yields to the compressive strenght reduction experimentally evidenced in damaged laminates. This loss of strength is caused by the out-of-plane buckling of the groups of plies, or sublaminates, above and below the delamination. When buckling of any of the sublaminates occurs, the remaining plies undergo not only the initial in-plane compression but also the bending stresses derived from unsymmetric loading of the laminate. Stresses in these plies are, consequently, greater than would exist in an undamaged panel, resulting in a reduced failure load.

When a delaminated composite panel is subjected to uniaxial in-plane

compression, different buckling modes (Figure 1.2 [8]) can develop depending upon delamination size and position.

(a) *Local buckling mode.*

(b) *Mixed buckling mode.*

(c) *Global buckling mode.*

Figure 1.2: Buckling modes of a delaminated composite panel.

Local buckling, depicted in Figure 1.2a, may occur when the upper sublaminate is thin and the delaminated area is large. In this case, the stiffness of the upper sublaminate is small relative to that of the lower one and, therefore, the thinner sublaminate buckles. Further loading upon the local buckling load can promote a mode switch to the mixed buckling mode shown in Figure 1.2b, which is a combination of local and global buckling modes that may arise prior to the collapse load. At this load, global instability of the structure happens, namely, the global buckling mode is observed. This mode is characterized by both sublaminates buckling in the same direction and with the same out-of-plane displacement as displayed in Figure 1.2c, and may be the first one to occur when the initial delamination has a small area and is located near the midsurface of the panel. In some cases, the collapse load can be attained without any propagation of the embedded damage.

Chapter 2

Numerical models for delamination

Several numerical techniques have been proposed to assess the delamination problem in composite laminates.

Traditional numerical tools are formulated within the framework of LEFM (Linear Elastic Fracture Mechanics). LEFM is based on Griffith's fracture theory [11], which according to the first law of thermodynamics, postulates that the reduction in strain energy due to propagation of a crack is used to create new crack surfaces. This assumption is valid for brittle materials, in which dissipation of energy derived from plastic deformation during fracture can be neglected because no significant process zone develops ahead of the crack tip. Since nonlinear crack tip processes take place within a plastic zone small relative to the smallest characteristic dimension of the specimen, numerical approaches based on LEFM assume that fracture mechanisms can be confined to the delamination front. Discontinuity growth is predicted when a combination of the components of the energy release rate G is equal or greater than a critical value G_C. Techniques such as the J-integral [12, 13], the EDT (Energy Derivative Technique) [14], the stiffness derivative [15] or the VCCT (Virtual Crack Closure Technique) are used to compute the G_C components using LEFM principles.

A more recent approach consists of models in which nonlinear crack tip processes are represented explicitly rather than being assigned to points at the discontinuity front. The cohesive zone formulation collapses onto a surface of displacement discontinuity the effect of progressive stiffness degradation due to irreversible damage of the resin-rich layer between laminas where delaminations arise. Based on Damage Mechanics, this approach seems to represent better physical mechanisms that develop ahead of the crack tip and allows overcoming some of the important drawbacks of the LEFM-based models.

In this chapter, further attention will be given to the formulation of

two of the most widespread procedures implemented in current FEM codes to simulate delamination: VCCT and cohesive elements.

2.1 The VCCT

The VCCT is a LEFM-based approach to predict crack propagation within brittle materials, such as PEEK (polyetheretherketone) and epoxy fiber-reinforced composites typically used in aircraft structural components. This technique is based on Irwin's assumption [16] that the strain energy released to extend a crack by a small amount Δa from a (Figure 2.1a [17]) to $a + \Delta a$ (Figure 2.1b [17]) is identical to the work required to close the crack to its original length a.

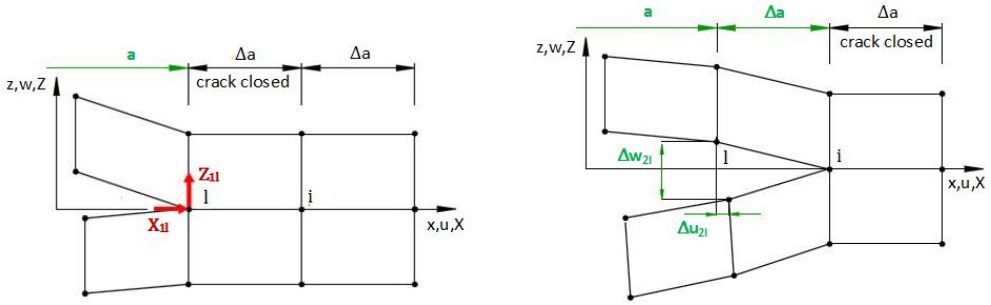

(a) *First step, crack closed.* (b) *Second step, crack extended.*

Figure 2.1: Two step VCCT (2D).

According to Griffith's fracture theory, local crack growth occurs when the total energy release rate, G_T, evaluated at a point along the delamination front reaches a critical value, G_C, called the mixed-mode fracture toughness of the material:

$$G_T \geq G_C \Rightarrow \text{Delamination propagation} \tag{2.1}$$

Available criteria to determine an accurate prediction of G_C will be discussed in Subsection 2.2.5. With regard to G_T, it can be calculated as the sum of the nodal pure mode I (interlaminar tension), mode II (sliding shear) and mode III (scissoring shear) energy release rates:

$$G_T = G_I + G_{\text{II}} + G_{\text{III}} \tag{2.2}$$

These energy release rate components, shown in Figure 2.2 [17], can be computed from the solution obtained from the FEM analysis as the work done by nodal forces to close the crack tip per unit of virtually closed area.

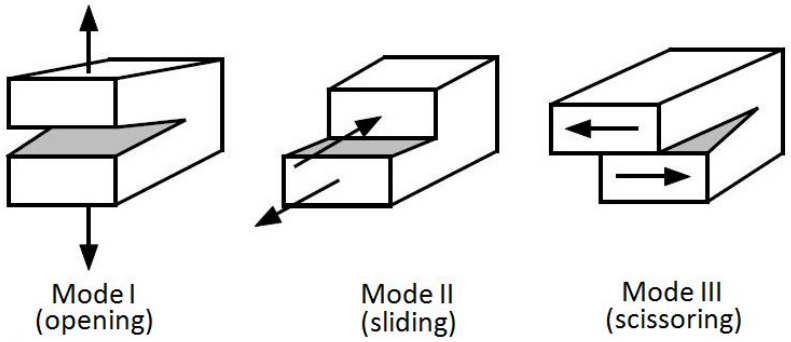

Figure 2.2: Interlaminar fracture modes.

Historically, this was done firstly by physically extending or closing the crack during two different finite element analyses. For the two-dimensional problem depicted in Figure 2.1 [17], the expression of the energy release rates obtained with this technique, referred in literature as the crack closure method or the two-step virtual crack closure technique, are:

$$G_I = \frac{1}{2\Delta a} Z_{1,l} \Delta w_{2,l}; \qquad G_{\mathrm{II}} = \frac{1}{2\Delta a} X_{1,l} \Delta u_{2,l} \tag{2.3}$$

In the former equations, Δa is the virtually closed crack length, equal to the length of the elements at the delamination front. $X_{1,l}$ and $Z_{1,l}$ are the shear and normal forces at node l computed in the first step to keep closed the crack (Figure 2.1a). $\Delta u_{2,l}$ and $\Delta w_{2,l}$ are the corresponding nodal separations obtained in the second step as the crack tip is allowed to extend by Δa until node i (Figure 2.1b).

The VCCT proposed by Rybicki and Kanninen [18] allows for significant alleviation of the computational cost of the analysis compared with the former method. For Δa small enough, that is, for a sufficiently fine mesh where fracture propagation is expected to occur, a delamination extension from $a+\Delta a$ (node l) to $a+2\Delta a$ (node i) in the three-dimensional problem depicted in Figure 2.3 [19]) does not significantly alter the state at the crack tip. Therefore, the displacements behind the extended crack tip at node i are approximately equal to the displacements behind the original crack tip at node l.

Under this assumption, energy release rate components G_I, G_{II} and G_{III} can be calculated in one single step without any virtual extension of the crack, using nodal forces at the current delamination front (row i) and displacements at first row of nodes behind the crack tip (row l):

$$G_I = \frac{1}{2\Delta A} Z_{Li} (w_{Ll} - w_{Ll^*}) \tag{2.4}$$

$$G_{II} = \frac{1}{2\Delta A} X_{Li}(u_{Ll} - u_{Ll^*}) \tag{2.5}$$

$$G_{III} = \frac{1}{2\Delta A} Y_{Li}(v_{Ll} - v_{Ll^*}) \tag{2.6}$$

where $\Delta A = s\Delta a$ is the virtually closed area and s is the width of the elements at the delamination front. In Figure 2.3, columns are identified by capital letters and rows by small letters. Hence, X_{Li}, Y_{Li} e Z_{Li} denote the forces at the delamination front in column L, row i. The corresponding displacements behind the delamination at the top face row l are denoted u_{Ll}, v_{Ll} e w_{Ll} and at the lower face row l^* are denoted u_{Ll^*}, v_{Ll^*} e w_{Ll^*}.

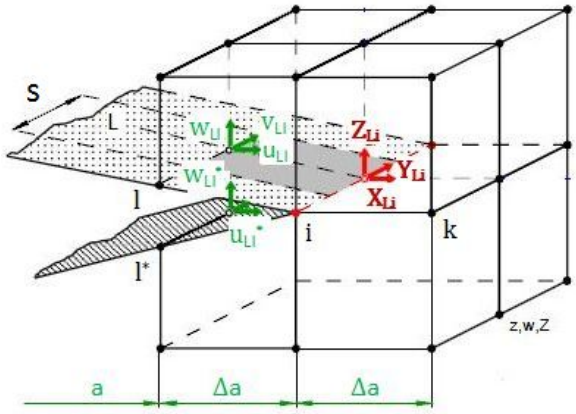

Figure 2.3: VCCT 3D.

Nevertheless, the assumption of self-similar delamination propagation, namely, that delamination front does not change its shape throughout the loading history, demands previous knowledge of the crack location and propagation direction. This requirement precludes VCCT from being used for several classes of very important delamination problems, such as free edge crack nucleation and growth and delamination caused by low-velocity impact, since it cannot predict damage initiation.

2.2 Cohesive elements

The formulation of cohesive elements is based on the CZM (Cohesive Zone Model) proposed by Dugdale and Barenblatt [20, 21] for simulating complex fracture mechanisms at the crack front.

The main advantage of cohesive zone models is the capability to predict both onset and propagation of delamination without previous knowledge of the flaw location and propagation direction. Hence, in contrast to

VCCT, problems such as study upon compressive behavior of composite plates containing multiple embedded artificial delaminations [22] as well as fracture analysis of composite co-bonded joints [23] can be numerically investigated. For this reason, cohesive zone formulation has become a very useful tool in designing damage tolerant composite structures.

2.2.1 CZM for brittle composites

The cohesive zone approach models an extended cohesive zone, or process zone, at interfaces where delaminations may occur, in which tractions τ_i or cohesive forces resist interfacial separations δ_i , often referred as relative displacements in literature.

The cohesive damage zone is the portion of the cohesive layer closer to delamination front in which any irreversible degradation of interface properties has taken place (Figure 2.4[24]). Elements within this zone are characterized by the fulfillment of the specified damage initiation criterion that governs the onset of the progressive damage process. Physically, the cohesive damage zone represents the manner in which the material stiffness degrades locally due to the coalescence of crazes around the crack tip.

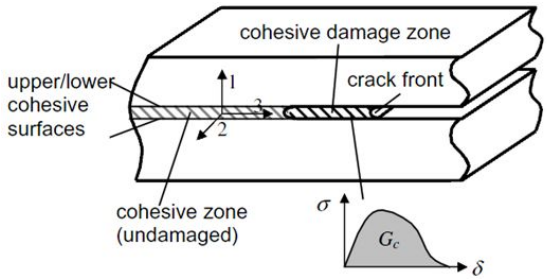

Figure 2.4: Schematic cohesive zone model.

According to Camanho[25], cohesive zone approaches can be related to Griffith's theory of fracture if the size of the cohesive zone is negligible when compared with characteristic dimensions of the specimen. This condition is satisfied by materials that exhibit quasi-brittle fracture behavior, such as PEEK or epoxy composites used in aerospace structures. The linking between both theories can be established setting the area under the traction-separation curve equal to the corresponding fracture toughness, regardless of its shape. For single-mode delamination, this means:

$$\int_0^{\delta_3^f} \tau_3(\delta_3)\, d\delta_3 = G_{\mathrm{IC}}; \int_0^{\delta_2^f} \tau_2(\delta_2)\, d\delta_2 = G_{\mathrm{IIC}}; \int_0^{\delta_1^f} \tau_1(\delta_1)\, d\delta_1 = G_{\mathrm{IIIC}} \qquad (2.7)$$

where G_{IC}, G_{IIC} and G_{IIIC} are respectively mode I, mode II and mode III fracture toughnesses and δ_3^f, δ_2^f and δ_1^f the corresponding final separations relative to the crack propagation under single-mode loading.

Similarly to Equations (2.7), the following expression can be written for the general mixed-mode problem:

$$\int_0^{\delta_m^f} \tau_m(\delta_m)\, d\delta_m = G_C \tag{2.8}$$

where G_C is the mixed-mode fracture toughness, δ_m the equivalent separation (defined in Subsection 2.2.4), τ_m the corresponding equivalent traction and δ_m^f the final equivalent separation associated to complete decohesion.

2.2.2 Geometry of the cohesive element

In a FEM model, a layer of cohesive elements is placed at interlaminar interfaces where debonding failure is expected to develop.

The connectivity of a cohesive element is like that of a continuum element; however, it is useful to think of a cohesive element as being composed of two faces (a bottom and a top face) separated by the cohesive zone thickness. The geometry of the zero-thicknes 8-node cohesive element used in this work is depicted in Figure 2.5 [26].

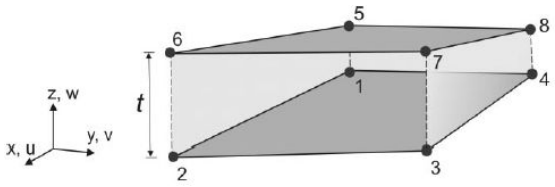

Figure 2.5: Geometry of the 8-node cohesive element.

The so called zero-thickness elements are suitable in situations where intermediate glue material is very thin and for all practical purposes may be considered to be of zero thickness, such as bonded composite laminae investigated in this work. In this case, macroscopic material properties are not relevant directly, and the analyst must resort to concepts derived from fracture mechanics, as discussed in the following sections.

2.2.3 Kinematics and stiffness matrix of the cohesive element

The constitutive equation of zero-thickness cohesive elements is established in terms of tractions τ and separations δ across the interface, both

defined with respect to the local reference system of the element. Computation of the stiffness matrix in global coordinates makes it necessary to express these separations in terms of global nodal displacements. This is perfomed in two steps: firstly, global separations are calculated from global nodal displacements and, secondly, local separations are obtained by performing an appropriate coordinates transformation.

The relation between separations and nodal displacements in global coordinates can be obtained from the kinematics of the cohesive element, shown in Figure 2.6 [23].

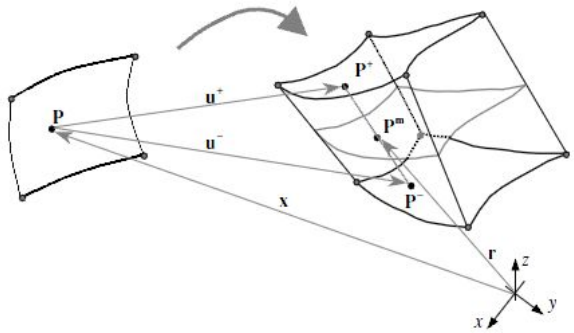

Figure 2.6: Kinematics of the zero-thickness cohesive element.

Let $\overrightarrow{X}$ be the vector corresponding to the initial position of a point P on the middle surface, $\overrightarrow{x}$ the current position vector of a point P^m on the element middle surface and u^+ and u^- the displacements of P^+ and P^- on the top and bottom surfaces, respectively. Then, the element middle surface is defined as:

$$x_i = X_i + \frac{1}{2}(u_i^- + u_i^+) \tag{2.9}$$

which evidences the relation between global separations and displacements on the top and bottom surfaces:

$$\Delta_i = u_i^+ - u_i^- \tag{2.10}$$

These displacements can be interpolated from nodal values:

$$u_i^+ = N_k u_{ki}^+, \quad k \in \text{top nodes} \tag{2.11}$$

$$u_i^- = N_k u_{ki}^-, \quad k \in \text{bottom nodes} \tag{2.12}$$

where u_{ki}^+, u_{ki}^- are the displacements in the i direction of the k top and bottom nodes of the element, respectively, and N_k are standard Lagrangian shape functions. Thus, Equation (2.10) can be rewritten as:

$$\Delta_i = N_k u_{ki}^+ - N_k u_{ki}^- = \overline{N_k} u_{ki} \tag{2.13}$$

The coordinate transformation between global and local coordinates is accomplished using the rotation tensor Θ_{si} defined in [26]:

$$\delta_i = \Theta_{si}\Delta_i = \Theta_{si}\overline{N_k}u_{ki} = B_{sik}u_{ik} \tag{2.14}$$

Let Γ be the mid-surface area in the deformed configuration, the cohesive element stiffness matrix and load vector can be determined from the principle of virtual work:

$$\int_\Gamma d\delta_s \tau_s d\Gamma = f_{ki} du_{ki} \tag{2.15}$$

$d\delta_s$ and du_{ki} are the virtual separations and nodal displacements respectively, whereas f_{ki} is the nodal load vector.

From Equation 2.14 and for a geometrically nonlinear problem:

$$\int_\Gamma \left(\frac{\partial B_{spj}}{\partial u_{ki}} u_{jp} + B_{sik} \right) \tau_s d\Gamma = f_{ki} \tag{2.16}$$

Substituting the expression of the constitutive law (Equation (2.18) in Subsection 2.2.4) into Equation (2.16), the scalar components of the element stiffness matrix can be finally computed:

$$K_{kizv} = \int_\Gamma \overline{\delta_{sr}} D_{sr} B_{rvz} \left(\frac{\partial B_{spj}}{\partial u_{ki}} u_{jp} + B_{sik} \right) d\Gamma \tag{2.17}$$

2.2.4 Constitutive law

The constitutive law that relates the element tractions τ to the element separations δ expressed in local isoparametric coordinates is:

$$\tau_s = D_{sr}\delta_r \tag{2.18}$$

The following hypotheses are taken into account for the definition of the constitutive operator D_{sr} [27]:

1. Linear elastic response prior to damage onset:

$$\tau_s = K_p \delta_s \tag{2.19}$$

   where K_p is the penalty stiffness. The value of K_p must be high enough to avoid interpenetration of the crack faces under compression loading and to prevent artificial compliance from being introduced into the model by the cohesive elements. However, too-high values of the penalty stiffness can lead to numerical problems, such as spurious oscillations of tractions [28]. In many cases, K_p is assumed to be the same for the three loading modes.

2. Failure of the cohesive element is characterized by progressive degradation of the material stiffness, which is driven by a damage process. A scalar overall damage variable d captures the combined damage effects of all active mechanisms and evolves monotonically from 0 to 1 upon further loading subsequent to damage onset. The analytical expression of d depends upon the damage evolution law chosen to describe the irreversible softening at the interface.

3. The cohesive layer does not undergo damage under pure normal compressive stresses or strains.

In order to describe delamination initiation and growth under a general mixed-mode loading condition, it is convenient to introduce the equivalent separation δ_m:

$$\delta_m = \sqrt{\delta_1^2 + \delta_2^2 + \langle \delta_3 \rangle^2} = \sqrt{\delta_{\text{shear}}^2 + \langle \delta_3 \rangle^2} \tag{2.20}$$

where δ_{shear} is the norm of the vector of the tangential separations. The Macauley operator $\langle \cdot \rangle$, defined as $\langle x \rangle = \frac{1}{2}(x + |x|)$, accounts for the fact that compression stiffness is not affected by damage.

The irreversibility of damage is taken into account by defining the constitutive equation in terms of the maximum equivalent separation $\delta_m^{\max}$, which refers to the maximum value of the equivalent separation attained during the loading history:

$$\delta_m^{\max} = \max\left(\delta_m, \delta_m^{\max}\right) \tag{2.21}$$

A single-variable constitutive law for mixed-mode delamination capable of tracking damage evolution at interfaces, capturing the irreversible softening behavior of the cohesive zone ad dealing with contact problems derived from compression loading can be established defining the constitutive operator D_{sr} as follows [26]:

$$D_{sr} = \begin{cases} \overline{\delta_{sr}} K_p, & \delta_m^{max} \leq \delta_m^0 \quad (2.22a) \\ \overline{\delta_{sr}} K_p \left[(1-d)K_p + dK_p \dfrac{\langle -\delta_3 \rangle}{\delta_3} \overline{\delta_{s3}} \right], & \delta_m^0 < \delta_m^{\max} < \delta_m^f \quad (2.22b) \\ \overline{\delta_{s3}}\ \overline{\delta_{3r}} \dfrac{\langle -\delta_3 \rangle}{\delta_3} K_p, & \delta_m^f \leq \delta_m^{\max} \quad (2.22c) \end{cases}$$

where $\overline{\delta_{sr}}$ is the Kronecker delta. Three different material behavior zones delimited by the equivalent separations corresponding to damage onset δ_m^0 and to total decohesion δ_m^f can be identified:

- *Linear elastic response prior to damage initiation* (2.22a).

- *Progressive softening upon further loading after damage onset* (2.22b).
- *Interpenetration control subsequent to ultimate failure of the element* (2.22c).

It can be noticed that the constitutive equation is coupled to the specified damage evolution law through the values of the critical separations δ_m^0 and δ_m^f, which can be computed defining appropriate damage onset and damage propagation criteria respectively, and through the overall damage variable d, which depends upon the shape of the softening law as well as on δ_m^0 and δ_m^f themselves. A suitable damage law defined in terms of equivalent separations δ_m and corresponding equivalent tractions τ_m is discussed in Subsection 2.2.5.

2.2.5 Damage evolution law

The damage evolution law to couple with the constitutive equation to describe the fracture behavior of the cohesive layer is defined by:

- A damage onset criterion.
- A softening law.
- A damage propagation criterion.

Damage onset criterion

Damage onset refers to the commencement of the stiffness degradation of the cohesive element. The softening process begins when the stresses and/or strains satisfy a predefined damage initiation criterion. Corresponding values of equivalent separation and equivalent traction are δ_m^0 and τ_m^0 respectively.

Under mixed-mode loading, initiation of the softening behavior may occur before any of the traction components attain their respective single-mode allowables, namely, the interlaminar tensile strength N and the interlaminar shear strengths S and T. Hence, the damage onset criterion must account for the interaction between normal and shear loadings. In this work, the quadratic stress criterion proposed by Cui et al. [29] was used, since it has been demonstrated to provide satisfactory predictions for composite laminates [26]:

$$\left(\frac{\langle \tau_3 \rangle}{N}\right)^2 + \left(\frac{\tau_2}{S}\right)^2 + \left(\frac{\tau_1}{T}\right)^2 = 1 \tag{2.23}$$

Among the several manners of measuring the mode ratio under mixed-mode loading conditions, the mode mixity ratio β has been used in the following discussion. For an opening separation δ_3 greater than zero, β is defined as:

$$\beta = \frac{\delta_{\text{shear}}}{\delta_3} \tag{2.24}$$

Using the quadratic stress criterion, the mixed-mode equivalent separation corresponding to the initiation of damage is given by [26]:

$$\delta_m^0 = \begin{cases} \delta_3^0 \delta_1^0 \sqrt{\dfrac{1+\beta^2}{(\delta_1^0)^2 + (\beta\delta_3^0)^2}}, & \delta_3 > 0 \qquad (2.25a) \\ \delta_{\text{shear}}^0, & \delta_3 \leq 0 \qquad (2.25b) \end{cases}$$

Using the same penalty stiffness for modes I, II and III and assuming isotropic shear behavior, that is , $S = T$, the equivalent separations δ_3^0, δ_1^0 and δ_{shear}^0 corresponding to the onset of softening under single-mode loading are equal to:

$$\delta_3^0 = \frac{N}{K_p}; \qquad \delta_1^0 = \delta_2^0 = \delta_{\text{shear}}^0 = \frac{S}{K_p} \tag{2.26}$$

Finally, equivalent traction τ_m^0 corresponding to damage initiation can be easily calculated as:

$$\tau_m^0 = K_p \delta_m^0 \tag{2.27}$$

Softening law

Among the several softening models commonly used (bilinear, exponential, perfectly plastic), the bilinear law employed in [26] to simulate the different interlaminar fracture toughness tests for the investigated material was adopted herein. Figure 2.7 [24] shows such a law.

Line AB represents the linear softening envelope of the bilinear constitutive equation. Unloading subsequent to damage onset is assumed to occur linearly towards the origin of the traction-separation plane. Reloading subsequent to unloading also occurs along the same linear path until the softening envelope is reached. Further reloading follows this envelope as indicated by the arrow until δ_m^f is attained.

Assuming a linear softening law, the overall damage variable d reduces to the expression proposed by Camanho [26]:

$$d = \frac{\delta_m^f (\delta_m^{\max} - \delta_m^0)}{\delta_m^{\max} (\delta_m^f - \delta_m^0)}, \qquad d \in [0, 1] \tag{2.28}$$

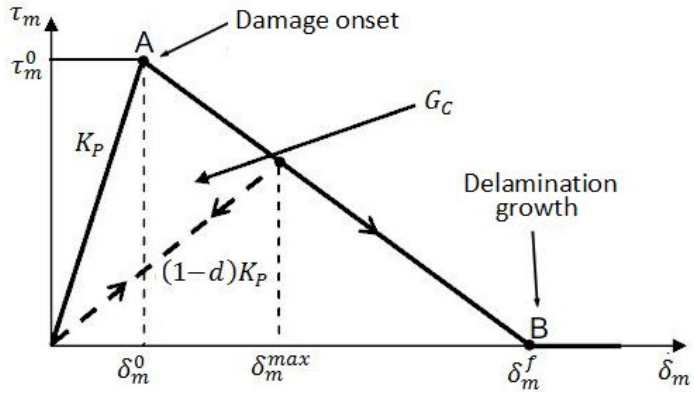

Figure 2.7: Linear Damage Evolution.

Damage propagation criterion

The definition of an appropriate damage propagation criterion allows for determining the equivalent separation δ_m^f corresponding to the reduction to zero of tractions that hold together the faces of the cohesive element.

For the bilinear law, Equation (2.8) in Subsection 2.2.1 reduces to:

$$\frac{1}{2}K_p\delta_m^0\delta_m^f = G_C \tag{2.29}$$

According to the principles of LEFM, mixed-mode delamination growth is predicted when $G_T \geq G_C$. Several laws have been implemented in FEM codes to consider for mode mixity when computing the fracture toughness of a material, such as the power law criterion [30], the B-K criterion [31] and the Reeder criterion [32]. Camanho et al. [26] demonstrated that for PEEK and epoxy composites examined in this work (AS4/PEEK and HTA/6376C respectively), predictions provided by the B-K criterion agree well with experimental results [33]. Indeed, the B-K law is suitable to predict mixed-mode fracture toughness for materials which exhibit the same critical fracture energies for both shear modes, that is, $G_{\mathrm{IIC}} = G_{\mathrm{IIIC}}$.

Assuming that the delamination mechanisms are the same for modes II and III, the concept of energy release rate for shear loading $G_{\mathrm{shear}} = G_{\mathrm{II}} + G_{\mathrm{III}}$ proposed by Li et al. [34, 35] is introduced into the B-K criterion. This consideration enables to overcome the fact that no adequate mixed-mode delamination growth criteria that incorporate mode III are available, as reliable mixed-mode tests methods with mode III loading have not been developed yet.

$$G_{IC} + (G_{IIC} - G_{IC})\left(\frac{G_{\mathrm{shear}}}{G_T}\right)^{\eta} = G_C, \qquad \text{with} \quad G_T = G_I + G_{\mathrm{shear}} \tag{2.30}$$

The parameter η is found by least-square fitting of experimental data obtained from MMB test performed at different mode ratios. G_I and G_{shear} are respectively the normal and shear components of the energy absorbed during fracture evolution until total decohesion is achieved.

For the linear softening law, the B-K criterion explicited in terms of the mode mixity ratio β is given by:

$$G_{IC} + (G_{IIC} - G_{IC})\left(\frac{\beta^2}{1+\beta^2}\right)^{\eta} = G_C \tag{2.31}$$

Using (2.29) into (2.31) and solving for δ_m^f, the mixed-mode equivalent displacement corresponding to total decohesion is obtained as [26]:

$$\delta_m^f = \begin{cases} \dfrac{2}{K_P \delta_0^m}\left[G_{IC} + (G_{IIC} - G_{IC})\left(\dfrac{\beta^2}{1+\beta^2}\right)^{\eta}\right], & \delta_3 > 0 \quad (2.32a) \\ \sqrt{(\delta_1^f)^2 + (\delta_2^f)^2}, & \delta_3 \leq 0 \quad (2.32b) \end{cases}$$

2.2.6 Mixed-mode damage model 3D representation

The mixed-mode bilinear damage evolution law presented in this chapter can be illustrated in the three-dimensional map shown in Figure 2.8 [27].

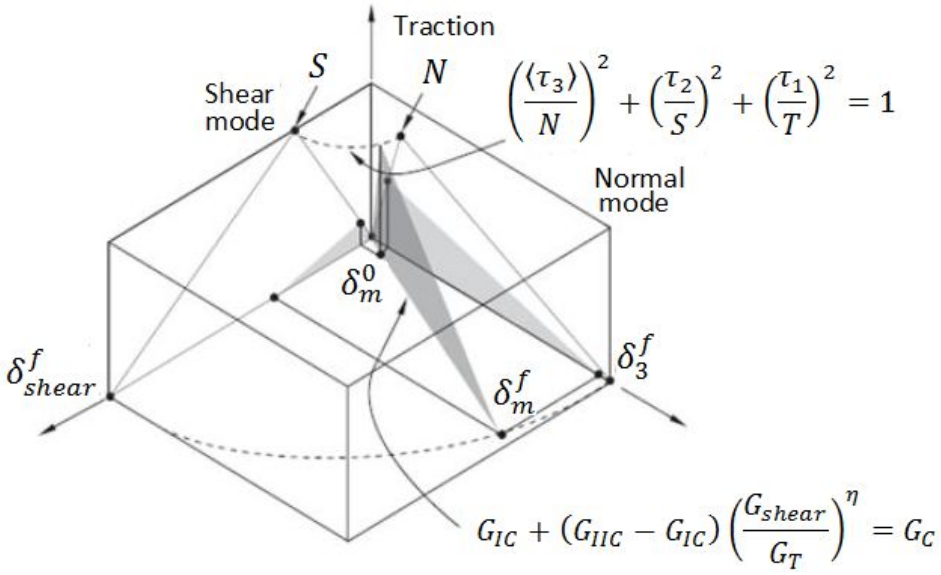

Figure 2.8: Mixed-mode response in cohesive elements.

The triangles $0 - N - \delta_3^f$ and $0 - S - \delta_{\text{shear}}^f$ represent the bilinear response in pure Mode I and pure shear mode respectively, while the shaded triangles in the two vertical coordinate planes represent the components of the mixed-mode energy release rate, G_I and G_{shear}, corresponding to total decohesion when is δ_m^f attained. All intermediate vertical planes containing the vertical axis represent the response under mixed-mode conditions with different mode mixity ratios β, clearly illustrating the dependence of damage onset and evolution upon the loading condition.

2.2.7 Validity of the model

The proposed damage model provides good predictions in case of delamination under constant-mode conditions.

Nevertheless, under variable mode conditions the definition of the damage threshold parameter as the maximum equivalent separation may lead to the violation of the Clausius-Duhem inequality. Thermodynamically consistent positive energy dissipation rate during damage evolution is not ensured by the presented model due to the eventual restoration of the cohesive state when the mode changes [36].

This can be illustrated in Figure 2.9 [36], where the bilinear constitutive law obtained for two different mode ratios $m = G_{\text{shear}}/G_T$ are represented.

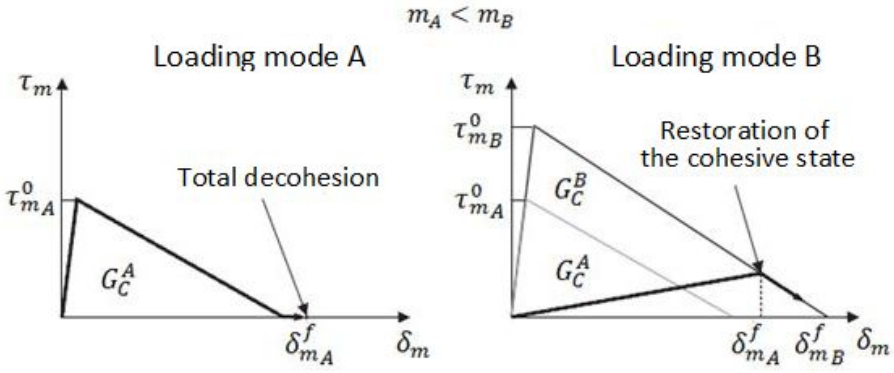

Figure 2.9: Restoration of the cohesive state for delamination propagation under variable mode-ratio.

If the mode-ratio changes from A to B during delamination growth, there is a thermodynamically inconsistent restoration of the cohesive state for $m_A < m_B$.

Chapter 3

Introduction to the DCB, ENF and MMF tests

This chapter reports a summarized description of the experimental procedures regarding the DCB (Double Cantilever Beam) and the ENF (End Noched Flexure) tests, simulated in Chapter 4, as well as the MMB test (Mixed-Mode Bending), simulated in Chapter 5.

Moreover, some of the available analytical methods to obtain preliminary estimations of the corresponding load-displacement curves are discussed. Assessment of their accuracy was performed through comparison with experimental data obtained by Reeder [37].

3.1 Standard test method for mode I interlaminar fracture toughness

3.1.1 Experimental test

Issued under the fixed designation D5528 within the ASTM (American Society for Testing and Materials) Standards [38], the DCB test is the standard experimental method for determining the opening Mode I interlaminar fracture toughness, G_{IC}, of continuous fiber-reinforced polymer matrix composites. An R curve (resistance curve) depicting G_{IC} as a function of delamination length is generated to characterize the initiation and propagation of a delamination in the specimen. The DCB test method is limited to use with composites consisting of UD (unidirectional) carbon fiber and glass fiber tape laminates with brittle and tough single-phase polymer matrices.

The DCB specimen shown in Figure 3.1 [38] consists of a rectangular, uniform thickness, UD composite laminate containing an even number of plies. Specimen length, $2L$, shall be at least 125mm and coupon width, b, from 20 to 25mm, inclusive. The laminate thickness, $2h$, shall be be-

tween 3 and 5mm. A non adhesive insert is inserted at the midplane ot the specimen during layup to form an initiation site for the delamination. The film thickness shall be no greater than 13μm. For thermoplastic matrix composites, such as the AS4/PEEK investigated in this chapter, a thin polyamid film is recommended. The initial delamination length, a_0, measured from the load line to the end of the insert, shall normally be 50 mm.

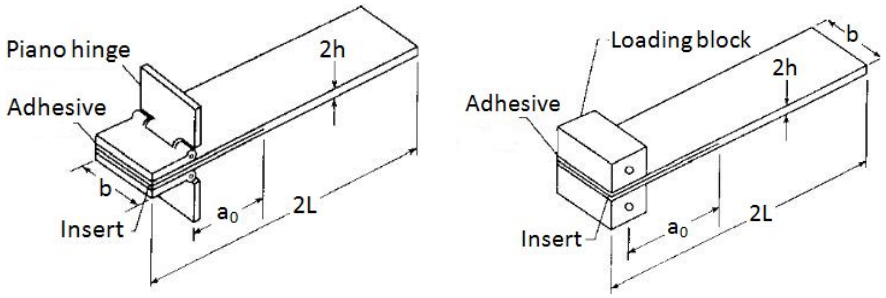

(a) *with piano hinges.* (b) *with loading blocks.*

Figure 3.1: DCB specimen.

Opening forces are applied to the DCB specimen by means of hinges (Figure 3.1a) or loading blocks (Figure 3.1b) bonded at one end of the specimen. The test machine shall be operated in a displacement control mode with a constant displacement rate in the range from 0.5 mm/min to 5.0 mm/min. Applied load versus opening displacement δ_{DCB} has to be recorded during the test. The opening displacement may be estimated as the crosshead separation, provided the deformation of the testing machine is less than 2% of the opening displacement of the test specimen; otherwise, it shall be obtained from a properly calibrated external gage or transducer attached to the specimen.

Three different data reduction methods for calculating mode I interlaminar fracture toughness values from load-displacement curves can be used: the MBT (Modified Beam Theory) method, the CC (Compliance Calibration) method or the MCC (Modified Compliance Calibration) method. Among them, the MBT is recommended, since it yields the most conservative values of G_{IC}. Further details upon the mode I interlaminar fracture toughness standard test can be found in [38].

3.1.2 Analytical solution of the DCB test

The analytical solution for the DCB test can be obtained via closed-form equations based on beam theory and linear elastic fracture mechanics [39].

Linear behavior prior to material softening can be determined using CBT (Classical Beam Theory) equations, considering each arm as a perfectly clamped beam at the delamination front:

$$\delta_{\mathrm{DCB}} = \frac{2a_0^3}{3\Big(E_{11}\frac{bh^3}{12}\Big)}P \tag{3.1}$$

where a_0 is the initial delamination length, E_{11} the longitudinal Young's modulus, b the specimen width and h the arm thickness, namely the half-thickness of the specimen. Opening displacement δ_{DCB} is equal to two times the vertical displacement of the loaded-edge of the laminate. This method, however, leads to an overestimation of the stiffness of the undamaged laminate because the beam is not perfectly built-in, that is, rotation may occur at the delamination front.

MBT model [40] can be used to obtain more reliable predictions of the initial stiffness. This calculation method treats the DCB specimen as if it contained a slightly longer initial delamination. In doing so, the estimated opening displacement is corrected for local shear deformation that occurs around the crack tip, not accounted for in CBT. An extra length, given by the product of the crack length correction factor χ and the arm thickness is, therefore, added to the measured initial crack length a_0:

$$\delta_{\mathrm{DCB}} = \frac{2(a_0+\chi h)^3}{3\Big(E_{11}\frac{bh^3}{12}\Big)}P \tag{3.2}$$

with

$$\chi = \sqrt{\frac{E_{11}}{11G_{13}}\left[3-2\Big(\frac{\Gamma}{1+\Gamma}\Big)^2\right]} \tag{3.3}$$

where Γ is the transverse modulus correction parameter which accounts for anisotropy:

$$\Gamma = 1.18\frac{\sqrt{E_{11}E_{22}}}{G_{13}} \tag{3.4}$$

in which, E_{22} and G_{13} are the transverse Young's modulus and the shear modulus respectively.

Clearly, for $\chi = 0$ Equation (3.2) becomes Equation (3.1).

The nonlinear response after the commencement of the delamination propagation can be obtained through the basic form of the strain energy release rate equation given by [41]:

$$G = \frac{P^2}{2b}\frac{dC}{da} = \frac{P}{2b}\frac{d\delta}{da}|_{P=cost} \tag{3.5}$$

where $C = \delta_{\mathrm{DCB}}/P$ is the compliance and a is the delamination length. For the MBT, Equation (3.2) can be substituted into Equation (3.5) to obtain G_I:

$$G_I = \frac{P^2(a+\chi h)^2}{b\left(E_{11}\frac{bh^3}{12}\right)} \tag{3.6}$$

Analytical solution for the nonlinear part can be determined substituting the expression of a obtained from Equation (3.6) (under the assumption that during fracture propagation G_I stays constant and equal to the experimental value of G_{IC} reported in Table 4.5) into Equation (3.2) to compute compliance as delamination grows. The nonlinear curve for the CBT can be obtained by simply setting χ to 0.

Computed analytical curves were plotted against experimental data [37] in Figure 3.2. Maximum calculated loads percentage errors with respect to experimental values are shown in Table 3.1.

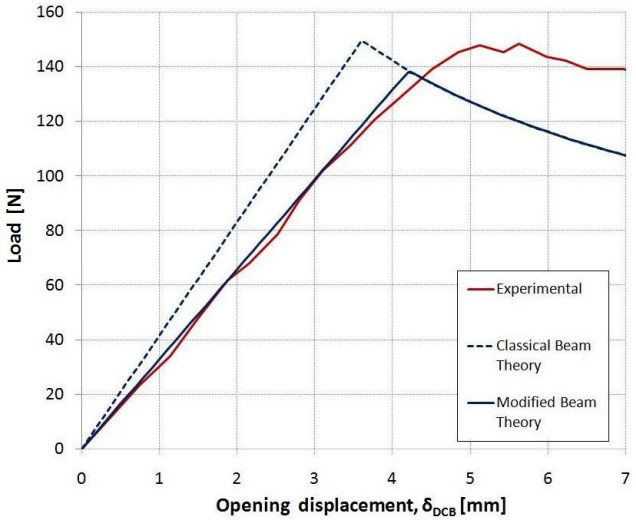

Figure 3.2: Analytical DCB curves.

Curve	P_{max} (N)	error (%)
Experimental [37]	147.3	0
CBT	149.5	1.49
MBT	138.1	-6.25

Table 3.1: Analytical DCB maximum loads (Figure 3.2).

CBT overestimates the stiffness of the undamaged DCB specimen by approximately 20%, although it obtains a closer prediction of the peak value than MBT. In any case, results show that, whenever experimental data is not available, reliable preliminary estimations of the response of the DCB specimen can be provided by the analytical models discussed in this Section.

3.2 Test methods for mode II interlaminar fracture toughness

3.2.1 Experimental tests

Unlike mode I and mixed-mode cases, a general consensus among researchers upon the standard for mode II interlaminar fracture toughness testing of fiber-reinforced composites has not been reached yet. The reasons for this are the tendency of delamination to grow in an unstable manner under mode II loading and, mainly, an uncomplete understanding of how friction forces between crack surfaces may affect the experimental evaluation of fracture toughness. Consequently, specific guidelines for performing the mode II test are still not available.

Despite this, different test procedures have been proposed. Figure 3.3 [42] shows the setup of four of the most commonly used test methods:

- *ENF (End Notched Flexure)* or *3ENF (Three-Point End Notched Flexure)* [43]. The ENF test is often unstable and, thus, it yields only the initiation value of mode II interlaminar fracture toughness. Unstable delamination growth consists of a run-arrest extension of the crack in which the delamination front jumps ahead abruptly as G exceeds energy required to create new crack surfaces G_{IIC}. This precludes propagation toughness values from being determined and may lead to nonconservative predictions for materials which exhibit lower propagation toughness values than the initiation one. The use of longer initial delamination increases the tendency for stable delamination growth during the test.

  A stabilized ENF test has been proposed in [44] to prevent instability from arising by controlling the real-time loading based on the measurement of crack silding displacement of the specimen. Nevertheless, this test procedure is much more complex than other tests methods.

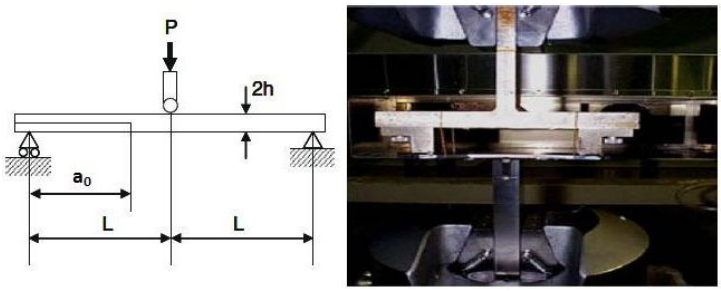

(a) *ENF (End Notched Flexure.)*

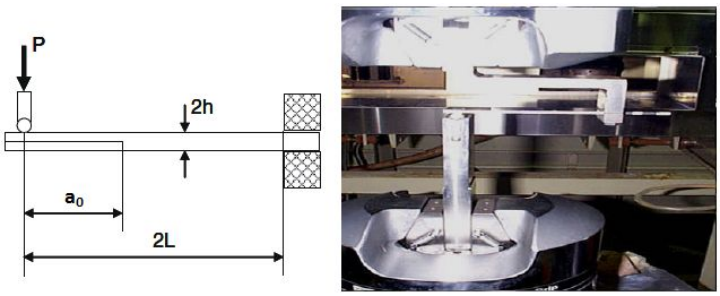

(b) *ELS (End Loaded Split).*

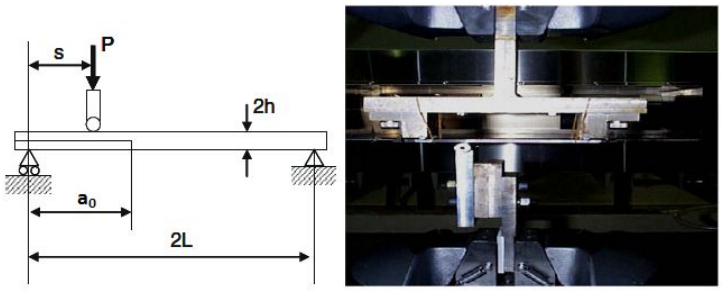

(c) *ONF (Over Notched Flexure).*

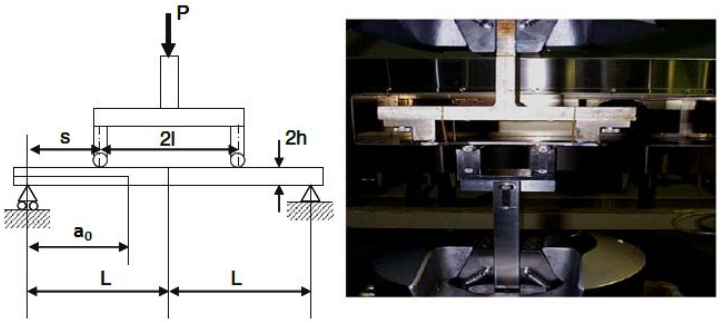

(d) *4ENF (Four-Point End Notched Flexure).*

Figure 3.3: Mode II interlaminar fracture toughness test methods.

- *ELS (End Loaded Split)* [45]. This test yields to stable delamination propagation but requires a relatively complex sliding fixture.
- *ONF (Over Notched Flexure)* [46] and *4ENF (Four-Point Bend End Notched Flexure)* [47]. Both methods yield to stable delamination growth and their test fixtures are simple. However, in both ONF and 4ENF tests it is difficult to remove friction effect between crack faces under the loading point placed over the crack. This frictional force can significantly slow down crack propagation and, as a result, data reduction methods based on the assumption of frictionless contact used in the calculation of G_{IIC} (conventional CC (Compliance Calibration) method) may yield to an overestimation of the delamination resistance. Therefore, results derived from 4ENF and ONF tests are typically higher than values computed from an ENF test. For this reason, further investigation is required to develop more accurate data reduction techniques which consider for the influence of friction upon 4ENF and ONF tests.

3.2.2 Analytical solution of the ENF test

The analytical solution for the ENF test can be determined through closed-form equations based on beam theory and linear elastic fracture mechanics [39].

The MBT method, even though not commonly used as a data reduction method for the ENF test, provides the analytical framework to compute the displacement of the specimen midpoint, v_m. Similarly to the DCB case, equations of the CBT method are corrected to account for shear deformations and rotations that occur around the delamination front by considering an additional crack length of $0.42\chi h$:

$$v_m = \left[\frac{3(a_0 + 0.42\chi h)^3 + 2L^3}{96\left(\frac{E_{11}bh^3}{12}\right)}\right]P \tag{3.7}$$

where L is the half length of the ENF specimen (Figure 3.3a) and χ is defined by Equations (3.3) and (3.4) in Subsection 3.1.2.

Substituting Equation (3.7) into Equation (3.1) in Subsection 3.1.2:

$$G_{\mathrm{II}} = \frac{3(a_0 + 0.42\chi h)^2 P^2}{64b\left(\frac{E_{11}bh^3}{12}\right)} \tag{3.8}$$

Nonlinear response subsequent to the onset of crack propagation can be generated substituting the expression of a obtained from Equation (3.8)

(under the assumption that during fracture propagation G_{II} stays constant and equal to the experimental value of G_{IIC} reported in Table 4.5) into Equation (3.7) to compute compliance as delamination grows.

CBT prediction for the load-displacement curve is obtained through the same procedure by simply setting χ to zero in Equations (3.7) and (3.8).

Computed analytical curves were plotted against experimental data [37] in Figure 3.4. Calculated peak loads and correspondent percentage errors with respect to experimental values are shown in Table 3.2.

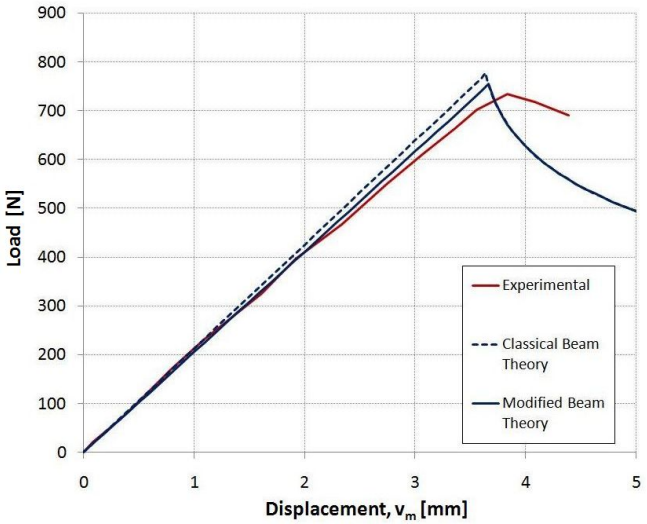

Figure 3.4: Analytical ENF curves.

Curve	P_{max} (N)	error (%)
Experimental [37]	734	0
CBT	777.1	5.87
MBT	755.4	2.92

Table 3.2: Analytical ENF maximum loads (Figure 3.4).

It is worth highlighting that, unlike the DCB estimation procedures, MBT exhibits better correlation to experimental data than CBT both in terms of stiffness prior to crack propagation and maximum predicted load. Nevertheless, stiffness degradation before the onset of fracture propagation displayed by the experimental curve is not captured by neither of the analytical models. Despite this, results show that, whenever experimental

data is not available, reliable preliminary estimations of the response of the ENF specimen can be provided by the analytical models discussed in this Section.

3.3 Standard test method for mixed-mode interlaminar fracture toughness

3.3.1 Experimental test

Issued under the fixed designation D6671/D6671M within the ASTM Standards [48], the MMB (Mixed-Mode Bending) test is the standard experimental method for determining the interlaminar fracture toughness, G_C, of continuous fiber-reinforced polymer matrix composites at various Mode I to Mode II loading ratios. Similarly to pure mode I and mode I tests, this method is limited to use with composites consisting of UD carbon fiber tape laminates with brittle and tough single-phase polymer matrices. However, the MMB test allows for obtaining the mixed-mode fracture toughness only as delamination propagation initiates from the insert. Hence, unlike the DCB test, in which propagation toughness values can be computed, no R curves can be derived for the mixed-mode case. Experimental fixture is shown in Figure 3.5 [48].

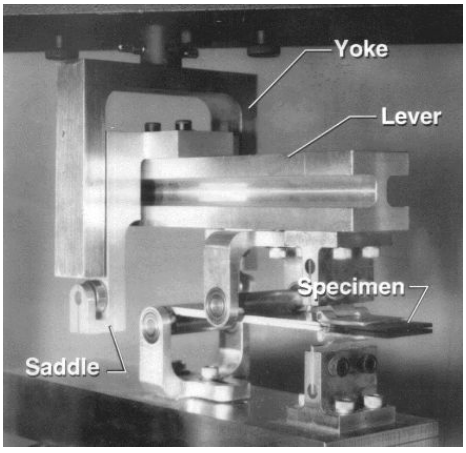

Figure 3.5: MMB fixture.

Loading forces are applied to the MMB specimen via tabs, which may be made from piano hinges or end blocks, that are applied near the ends of the delaminated section of the specimen and through rollers that bear against the specimen in the nondelaminated region to allow sliding with

minimal friction. The base of the MMB apparatus attaches to the bottom specimen tab and also bears on the specimen near the far end with a roller to hold the specimen stationary while loaded by the lever.

The MMB lever attaches to the top tab and bears down on the specimen halfway between the base roller and the tabs. The lever roller acts as a fulcrum so by pushing down on the lever arm opposite the tab, a downward load is applied to the specimen center creating mode II, while an upward force is appled to the split end of the laminate creating Mode I. Figure 3.6 [49] evidences that the MMB test is actually a combination of the standard DCB test for mode I toughness and the ENF test for mode II toughness.

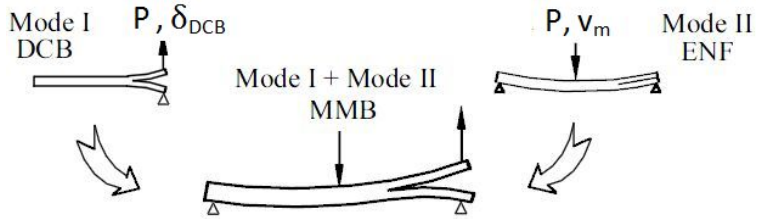

Figure 3.6: Mode I-mode II loading in the MMB test.

The proportion of Mode I and Mode II loading in a MMB test is controlled by setting the length of the lever arm, c, and remains essentially constant during delamination growth. Mixed-mode ratios of G_{II}/G_T between 20 and 100% can be obtained.

Geometry of the MMB apparatus and specimen is depicted in Figure 3.7 [49].

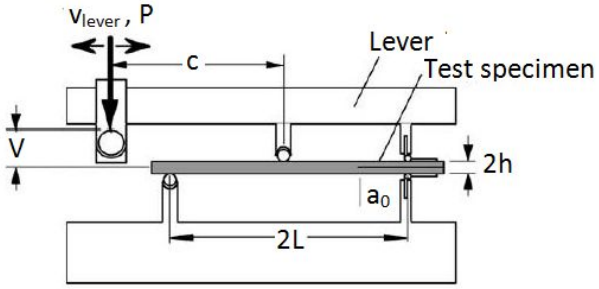

Figure 3.7: MMB apparatus and specimen geometry.

The half-span length of the MMB apparatus L shall be 50 mm. The overall length of the specimen is not critical but is normally around 137 mm, whereas the width of the specimen shall be between 20 and 25 mm. The laminate thickness shall be normally between 3 and 5 mm, with a

variation in thickness for any given specimen not greater than 0.1mm. The insert length a_0 is approximately 50 mm which corresponds to an initial delamination length of approximately 25 mm plus the extra length required to apply the tabs, with a maximum film thickness of 13 μm. To reduce geometrical nonlinear effects as a result of lever rotation, the lever shall be loaded such that the height V of the loading point above the pivot point is about $0.3L$.

Permanent record during the test of load versus opening displacement at the point of load application must be performed. The load point displacement may be taken from the crosshead separation of the load frame or from an external gage attached to the MMB apparatus such as an LVDT (Linearly Variable Displacement Transducer). The test is carried out in displacement control, with a constant displacement rate that ranges from 0.5 to 5.0 mm/min.

Mixed-Mode fracture toughness G_C is then derived from experimental data by means of closed-form equations based on modified beam theory, which consider shear and bending deformations occurring near the crack tip. A compliance calibration technique is not used because delamination growth is not always stable and because the specimen cannot simply be adjusted in the loading fixture to obtain data from different delamination lengths.

Occasionally, when testing low toughness material, the weight of the lever may cause significant loading of the MMB specimen. Therefore, the measured G_C may be affected. Correction for lever weight is then required.

Further details upon the mixed mode I-mode II interlaminar fracture toughness standard test can be found in [48].

3.3.2 Analytical solution of the MMB test

The analytical solution for the MMB test can be obtained through closed-form equations based on beam theory and LEFM [39]. Because the MMB test combines the DCB and ENF tests, equations for displacement and strain energy release rate for these tests will be used in the calculations for the MMB test.

It was shown in [49] that equivalent DCB and ENF loadings can be calculated from the applied load to the MMB test, P:

$$P_{\mathrm{DCB}} = \frac{3c - L}{4L} P \tag{3.9}$$

$$P_{\mathrm{ENF}} = \frac{c + L}{L} P \tag{3.10}$$

The former equations can be derived from the superposition analysis depicted in Figure 3.8 [37].

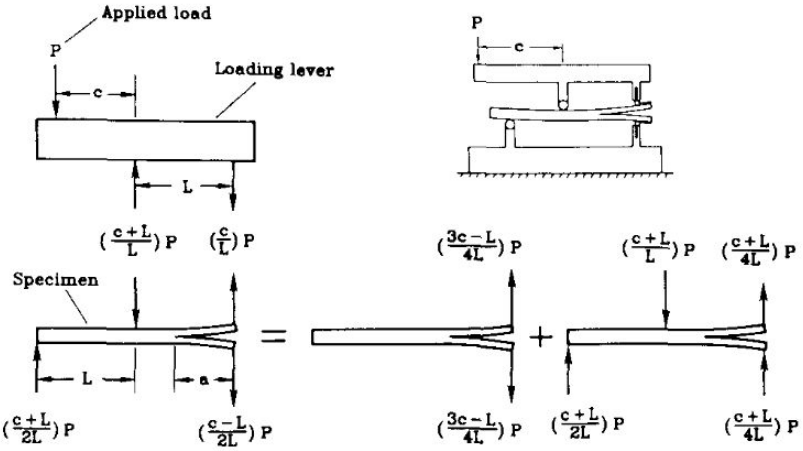

Figure 3.8: Superposition analysis of the mode I and mode II loading in the MMB specimen.

The load-point displacement v_{lever} is obtained from the pure mode displacement components δ_{DCB} and v_m as [39]:

$$v_{\text{lever}} = \frac{3c - L}{4L}\delta_{\text{DCB}} + \frac{c + L}{L}v_m \tag{3.11}$$

Substituting Equation (3.11) into Equations (3.1) and (3.7) respectively, the linear elastic solution through MBT is determined:

$$v_{\text{lever}} = \frac{4(3c - L)^2(a_0 + \chi h)^3 + (c + L)^2\Big[3(a_0 + 0.42\chi h)^3 + 2L^3\Big]}{96L^2\Big(E_{11}\frac{bh^3}{12}\Big)}P \tag{3.12}$$

in which all symbols have their usual meaning.

The expression of G is obtained substituting Equation (3.12) into Equation (3.5) in Subsection 3.1.2:

$$G = \frac{4(3c - L)^2(a + \chi h)^2 + 3(c + L)^2(a + 0.42\chi h^2)}{64L^2\Big(\frac{E_{11}bh^3}{12}\Big)}P^2 \tag{3.13}$$

Nonlinear response can be computed substituting the expression of a obtained from Equation (3.13) (under the assumption that during fracture growth mixed-mode energy release rate G stays constant and equal to experimental values of G_C reported in Table 4.5 for each mode ratio) into Equation (3.12) to determine compliance as crack extends.

CBT prediction for the MMB test is obtained through the same procedure by simply setting χ to zero in Equations (3.12) and (3.13).

Computed analytical curves at different G_{II}/G_T values were plotted against corresponding experimental data [37]. Results for mode ratios equal to 0.20, 0.50 and 0.80 are shown in Figures 3.9, 3.10 and 3.11 respectively, while maximum load values are reported in Table 3.3.

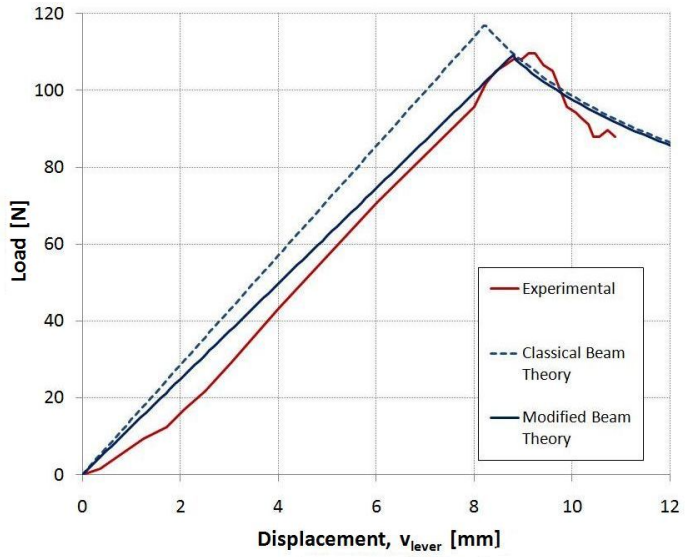

Figure 3.9: Analytical MMB curves for $G_{\mathrm{II}}/G_T = 0.20$.

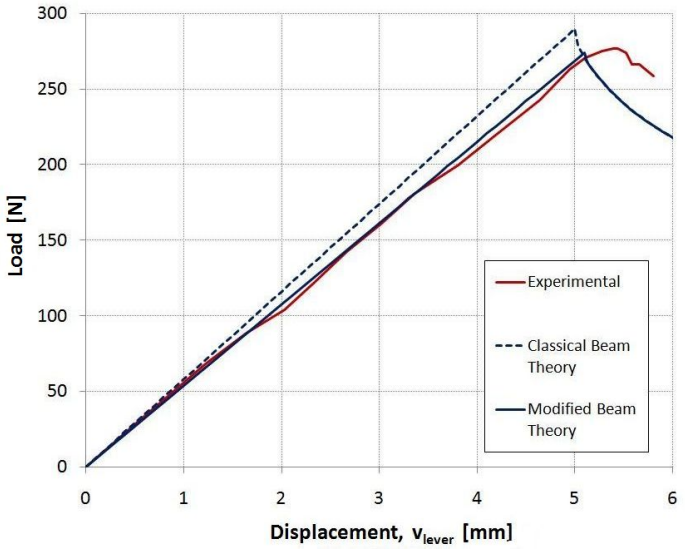

Figure 3.10: Analytical MMB curves for $G_{\mathrm{II}}/G_T = 0.50$.

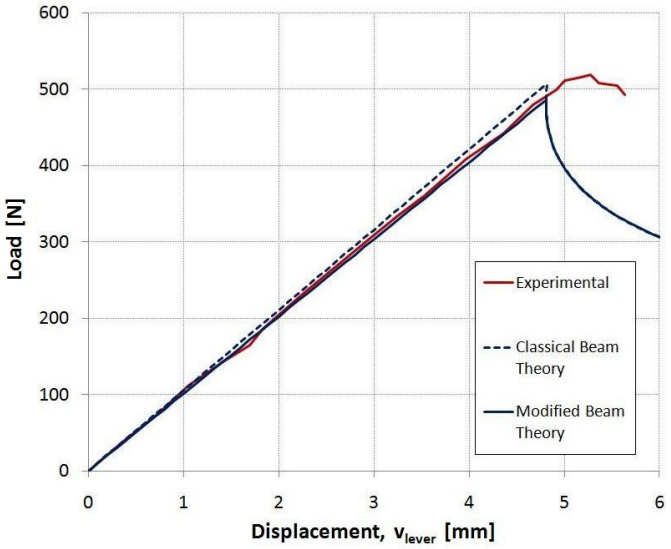

Figure 3.11: Analytical MMB curves for $G_{\mathrm{II}}/G_T = 0.80$.

Curves	$\frac{G_{\mathrm{II}}}{G_T} = 0.20$		$\frac{G_{\mathrm{II}}}{G_T} = 0.50$		$\frac{G_{\mathrm{II}}}{G_T} = 0.80$	
	P_{max} (N)	error (%)	P_{max} (N)	error (%)	P_{max} (N)	error (%)
Experimental [37]	108.1	0	275.4	0	518.7	0
CBT	109.2	1.02	290	5.30	506	-2.45
MBT	99.9	-7.59	274.2	-0.44	485.1	-6.48

Table 3.3: Analytical MMB maximum loads (Figures 3.9, 3.10 and 3.11).

Accuracy of the predicted response by the analytical curves depends upon the mode ratios. Nevertheless, the percentage error of the calculated maximum loads is less than 8% for all the loading conditions, which demonstrates that, whenever experimental data is not available, reliable preliminary estimations of the load-displacement curve can be provided by the analytical models discussed in this Section.

It can be observed, as well, that for both analytical models agreement with experimental data in the nonlinear zone gets worse as mixed mode increases: analytical curves display much more consistent load drops at high mode II regimes. These curves show, in fact, an increasing tendency towards unstable crack propagation at high mode ratios (instability being characterized by a displacement decrease upon further loading after the peak load). Only the careful selection of geometrical parameters of the three investigated MMB specimens precludes this from actually occuring.

Chapter 4

DCB and ENF models: parametric studies

A numerical investigation upon single-mode delamination in a unidirectional AS4/PEEK laminate is reported in this Chapter. A set of FEM models were implemented in Abaqus/Standard to predict delamination growth and damage evolution under pure mode I and pure mode II loading conditions. This aim was pursued by simulating the DCB and the ENF tests, whose results are presented in Sections 4.2 and 4.3 respectively.

Sensitivity analyses of the response to several model and mesh parameters were conducted for both tests. The purpose of these parametrical studies was to achieve a unique set of parameters that yielded a good compromise between computational cost and accuracy with respect to experimental data for both loading conditions simultaneously. Validation of the calibrated models was carried out plotting the predicted load-displacement curves against corresponding experimental response obtained by Reeder [37]. Additionally, numerical results computed by Camanho in [26] are reported.

4.1 On the DCB and ENF models

This Section provides information about geometry, material properties and mesh pattern of the DCB and ENF models implemented in this Chapter and the MMB specimens simulated in Chapter 5. Model and discretization parameters investigated in the sensitivity studies are discussed as well.

4.1.1 Specimens geometry

Geometry of the simulated specimens is shown in Figure 4.1. Length $2L$, width b and thickness $2h$ of the specimens are common to all the simulated tests, including the MMB, and are reported in Table 4.1. It can be noticed that length of the simulated specimens is shorter than that prescribed by

the ASTM Standards [38] and [48]. In fact, only the span length from the load line to the opposite support, in the DCB and MMB tests, and between the two supports, in the ENF test, were modeled. Initial crack length values a_0, shown in Table 4.2, were extracted from [26] and ensure a stable fracture propagation during the whole simulation time.

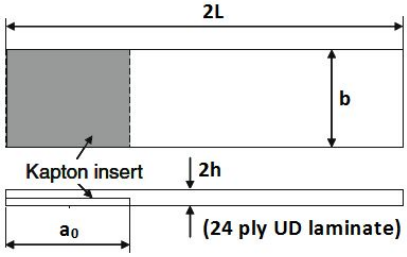

Figure 4.1: Sketch of the geometry of the DCB, ENF and MMB specimens.

$2L$ (mm)	b (mm)	$2h$ (mm)
102	25.4	3.12

Table 4.1: DCB, ENF and MMB specimen dimensions.

	(DCB)	(MMB)			(ENF)
G_{II}/G_T	0	0.20	0.50	0.80	1.0
a_0 (mm)	32.9	33.7	34.1	31.4	39.3

Table 4.2: Initial crack lenghts a_0 for the DCB, ENF and MMB models.

4.1.2 Modelization issues and mesh pattern

The 24-ply unidirectional AS4/PEEK specimens were modeled with two layers of S4R, namely, 4-node, quadrilateral shell elements with reduced integration and a large-strain formulation. Hourglass occurance was checked comparing results with those obtained using fully integrated S4 elements. Difference was negligible in all DCB, ENF and MMB analyses and, even, sligthly more accurate predictions were computed with the S4R. Since the number of integration points per element decreases from four to one, running time was significantly reduced as well (see Section 5.3).

The reference surfaces of the sub-laminates were moved from the mid-surface of the sub-laminates to the contact surface between the two sub-laminates using the shell property option OFFSET, as suggested in [27] for a more precise geometrical modelization in contact problems.

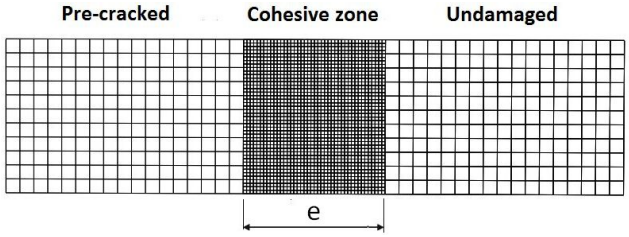

Figure 4.2: Sketch of the mesh pattern of the models.

Three levels of mesh refinement were considered within the specimen as depicted in Figure 4.2:

- *Pre-cracked region*, where the Kapton insert of length a_0 (Table 4.2) is located. Contact algorithm to avoid interpenetration between the upper and lower arms was only implemented for ENF and MMF tests. The DCB specimen does not require this procedure as arms are pulled appart and no contact interference is expected.

- *Cohesive zone region*, where delamination propagation may occur. A layer of cohesive elements was placed between upper and lower shell elements to simulate damage evolution within the interlaminar interface. For each test, length e was chosen such that the delamination front would not propagate beyond this region at the end of the analysis (see Table 4.3).

- *Undamaged region*, where delamination propagation shall not occur. The upper and lower layers of shell elements were connected together by means of beam type multi-point constraints, simulating a perfect bond.

	(DCB)	(MMB)			(ENF)
G_{II}/G_T	0	0.20	0.50	0.80	1.0
e (mm)	18.35	34.6	33.8	39.2	23.4

Table 4.3: Length of the cohesive zone region, e, for the DCB, ENF and MMB models.

Tie constraints were defined as well to allow for rapid transitions in mesh density along the lines between the cohesive zone and the adjacent regions.

4.1.3 Material properties

Laminates consist of plies from PEEK matrix, a thermoplastic resin, reinforced with continuous high stress, high strain carbon AS4 fiber. Mechanical and interface properties of the AS4/PEEK are shown in Tables 4.4 and 4.5 [37]. A value of $\eta = 2.284$ was used for the B-K criterion as suggested in [26].

E_{11} (GPa)	$E_{22} = E_{33}$ (GPa)	$G_{12} = G_{23}$ (GPa)	G_{23} (GPa)	$\nu_{12} = \nu_{13}$	ν_{23}	N (MPa)	$S = T$ (MPa)
122.7	10.1	5.5	3.7	0.25	0.45	80	100

Table 4.4: Material properties (AS4/PEEK).

G_{II}/G_T	0	0.20	0.50	0.80	1.0
$G_C(kJ/m^2)$	0.969 (G_{IC})	1.103	1.131	1.376	1.719 (G_{IIC})

Table 4.5: Interlaminar fracture toughness (AS4/PEEK).

4.1.4 Selected parameters for the sensitivity analysis

Sensitivity studies discussed in Sections 4.2.2 and 4.3.2 were conducted to examine the influence of various parameters upon the load-displacement curves of the DCB and ENF models.

Investigated parameters can be divided into two categories:

- *Cohesive zone model parameters.* These parameters are required to define the traction-separation law of the cohesive elements:
  - *Penalty stiffness (K_p).* Possible values of K_p to prevent both the introduction of artificial compliance to the model and numerical instability depend upon material properties. However, conditions to be fulfilled when selecting K_p to ensure an appropriate response of cohesive elements are not very restrictive. Hence, this choice stays quite arbitrary and shall be based on empirical methods, experience and data found in literature.

- *Viscous regularization factor (μ).* Material models exhibiting softening behavior and stiffness degradation often lead to severe convergence difficulties of the Newton-Raphson method, even if a line-search algorithm is activated. Numerical convergence depends upon the mesh refinement, the elastic properties of the system and the parameters associated to the cohesive model.

  A common technique that aids in overcoming these convergence difficulties is the viscous regularization method, which causes the tangent stiffness matrix of the softening material to be positive for sufficiently small time increments through the introduction of an additional viscous term in the constitutive law of the cohesive element [50]. A high value will speed up convergence and, hence, reduce the computing time; however, it may lead to erratic results. In any case, it is convenient to check that viscous energy be small compared to overall strain energy to ensure that the cohesive response is not significally altered by the dissipation term.

- *Discretization parameters.* These parameters define the discretization pattern and mesh density of the FEM model.

  - *Size of the elements within the cohesive zone (size).* Solutions achieved by using cohesive elements when simulating delamination mechanisms depend strongly upon the mesh refinement within the cohesive zone region. Indeed, element size in this area constraints the way in which the delamination front may extend. Furthermore, in order to yield realistic predictions of the delamination evolution, discretization of the cohesive zone region has to be sufficiently fine to ensure an accurate representation of the interlaminar stress fields ahead of the crack tip. For these reasons, investigation on the dependency of the simulated response upon mesh density is necessary to properly select the characteristic size of the cohesive elements.

  - *Fine-coarse ratio (fc).* This parameter is defined as the ratio between the number of elements along the width of the specimen in the cohesive zone region and the number of elements along the width in adjacent regions (the pre-cracked and the undamaged regions). It enables to evaluate the effect of employing a coarser mesh outside the cohesive zone region. Different mesh patterns corresponding to the DCB specimen obtained varying the fc value are shown in Figure 4.8.

4.2 Numerical analysis of the DCB test

This Section reports the implemented methodology to determine a suitable set of parameters for the DCB model.

4.2.1 Boundary conditions and prescribed displacements

Configuration and boundary conditions of the DCB specimen are depicted in Figure 4.3. Vertical displacement v_e at loaded edge was applied linearly until a maximum value of 3.5mm. Opening displacement δ_{DCB} is equal to $2v_e$. All displacement and rotation components were constrained at nodes on the opposite edge of the specimen.

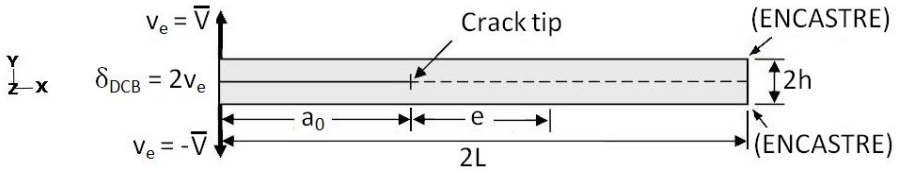

Figure 4.3: Boundary conditions and prescribed displacements in the DCB model.

4.2.2 Parametric studies

Sensitivity studies were carried out to investigate the influence of parameters presented in Section 4.1.4 upon the load-displacement curve obtained by the DCB model.

Reference paper concerning numerical simulation of this test [26], though, does not provide precise details about the investigated parameters, except from the penalty stiffness value. Without more guidelines, the search for an appropriate set required a considerable amount of analyses. For this reason, results obtained by these intermediate models are not reported in this work. The same applies to the ENF case in Section 4.3.

Curves presented as follows were generated, on the contrary, varying one parameter at a time with respect to the set of parameters that fits better experimental data among those investigated. Parameter values of this set are summarized in Table 4.6. Corresponding load-displacement curve is plotted in blue solid line in following figures.

Penalty stiffness, K_p (N/mm^3)	10^6
Viscous regularization factor, μ	10^{-4}
Fine-coarse ratio, fc	4
Element size in the cohesive zone, $size$ (mm)	0.5

Table 4.6: Selected set of parameters for the DCB model.

Sensitivity analysis to penalty stiffness

Figure 4.4 shows that similar results can be obtained using different combinations of penalty stiffness and viscous regularization factor. Since $K_p = 10^6$ was shown to provide good results for AS4/PEEK in [26], this value was mantained for the penalty stiffness. Correlation with experimental data was then improved through the adjustment of the viscous regularization factor.

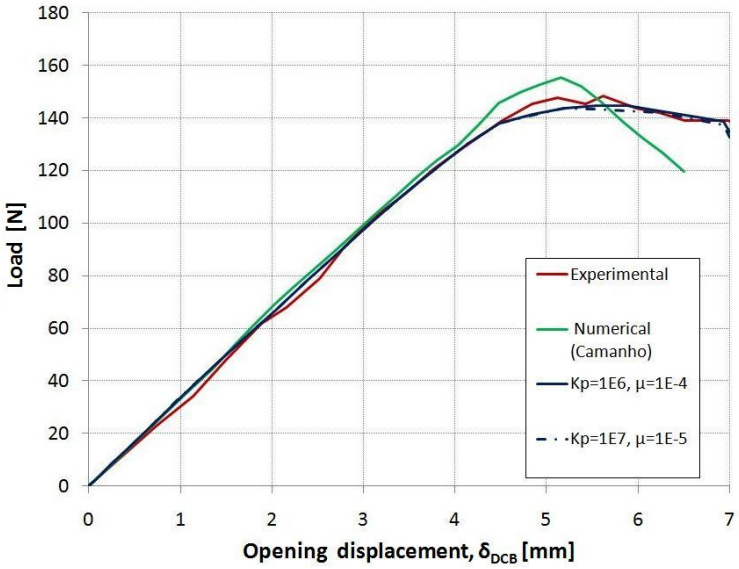

Figure 4.4: Sensitivity to the penalty stiffness the DCB model.

Sensitivity analysis to viscous regularization factor

Figure 4.5 shows how the amount of artificial viscous dissipation affects the response during delamination growth under pure mode I loading. Three different viscous regularization factors were considered. For $\mu = 10^{-3}$, the load-displacement curve does not show any softening behavior within the simulated opening displacement range. On the contrary, for $\mu = 10^{-5}$ the

peak load value is slightly underpredicted, while load drop is overestimated. Finally, setting μ to 10^{-4} generates an intermediate response that correlates properly to experimental data. Estimated maximum load values are reported in Table 4.7.

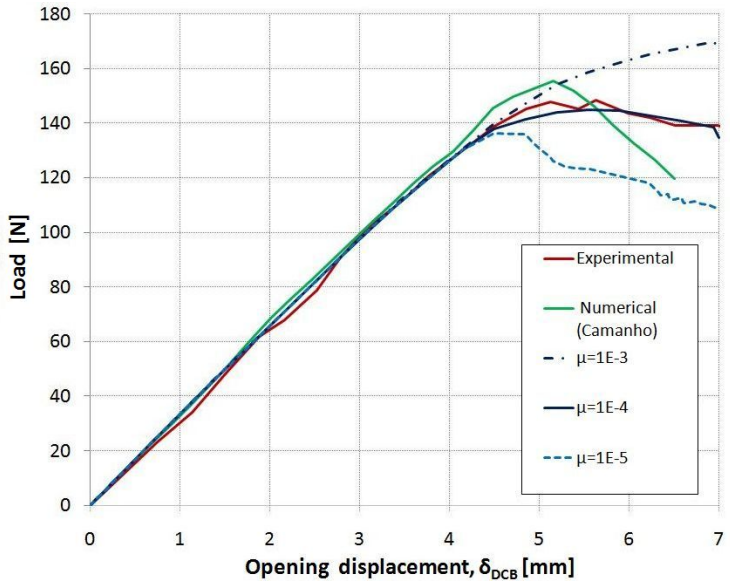

Figure 4.5: Sensitivity to viscous regularization factor of the DCB model.

	P_{max} (N)	error (%)
Experimental [37]	147.3	0
Numerical (Camanho) [26]	155.3	5.43
$\mu = 1E-3$	No softening response	
$\mu = 1E-4$	144.8	-1.70
$\mu = 1E-5$	136.2	-7.47

Table 4.7: Maximum loads in Figure 4.5.

Sensitivity analysis to element size within the cohesive zone region

Element length in the cohesive zone layer must be carefully chosen to capture correctly the continuum stress field ahead of the delamination front. Turon [51] suggests that a minimum of three elements in the cohesive

damaged zone are required to provide good resolution for the stress distribution responsible for delamination evolution. The cohesive damaged zone is the portion of the cohesive zone located just ahead of the crack tip where initiation of the irreversible softening process is observed. Its length l_{cz} is the distance from the delamination front to the point when the maximum cohesive traction is attained. Figure 4.6 displays this distance for pure mode I delamination.

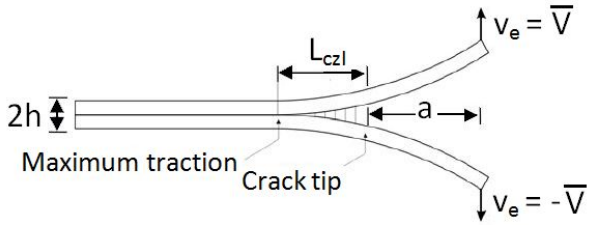

Figure 4.6: Length l_{czI} of the cohesive damaged zone for pure mode I.

Estimations of the length l_{czI} of the cohesive damaged zone for single mode I, valid for an infinite body under remote loading, were computed substituting values in Tables 4.4 and 4.5 into Equation (4.1):

$$l_{\mathrm{czI}} = ME_{22}\frac{G_{\mathrm{IC}}}{N^2} \tag{4.1}$$

where M is a parameter that depends on the cohesive zone theory used to derive the expression for the cohesive zone length.

The most commonly used models in literature are Rice's model [52], with $M = 0.88$, and Hillerborg's model [53], with $M = 1$. Choosing one theory rather than the other is not actually a critical issue: predicted l_{czI} was only used to derive an estimation of a potentially suitable element size l_{eI} within the cohesive zone region. Therefore, computed size value through Equation 4.2 has to be interpreted as a mere reference value from which to start sensitivity studies:

$$l_{\mathrm{eI}} = \frac{l_{\mathrm{czI}}}{N_e} \tag{4.2}$$

in which $N_e = 3$ is the requested minimum number of elements within the cohesive damaged zone according to [51].

This being said, the Hillerborg's model was employed as it provides the least conservative estimation of l_{czI} and, therefore, leads to a suggested coarser mesh than the Rice's model. Convenience of this choice was assessed *a posteriori*. Estimated length of the cohesive damaged zone

through Equation (4.1) is $l_{czI} = 1.5mm$, which using Equation (4.2) yields to a recommended element size of $l_{eI} = 0.5mm$.

Mesh-dependency of the response is shown in Figure 4.7. Table 4.8 reports the obtained maximum load values. Numbers between brackets denote the aproximate number of elements within the cohesive damaged zone associated to each mesh size.

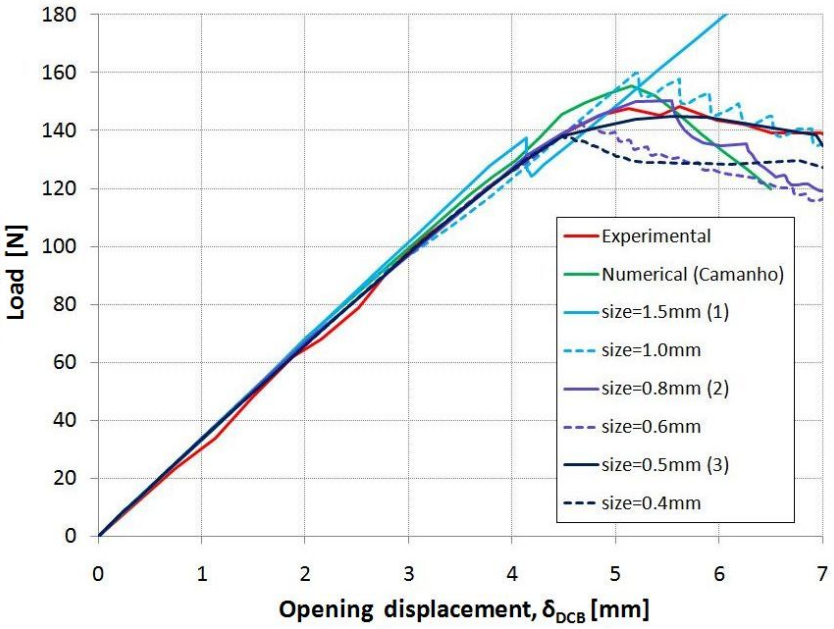

Figure 4.7: Sensitivity to mesh density in the cohesive zone of the DCB model.

	P_{max} (N)	error (%)
Experimental [37]	147.3	0
Numerical (Camanho) [26]	155.3	5.43
size = 1.5mm (3)	No softening response	
size = 1.0mm	159.9	8.70
size = 0.8mm (2)	150.2	2.11
size = 0.6mm	142.7	-2.99
size = 0.5mm (3)	144.8	-1.70
size = 0.4mm	138.1	-6.11

Table 4.8: Maximum loads in Figure 4.7.

As expected, there is a great sensitivity to the element size of the response during delamination growth. On the contrary, initial stiffness is not influenced by this parameter.

It can be noticed that a mesh with only one element along the cohesive damaged zone ($size = 1.5$mm) is clearly too coarse to correctly represent the stress field at the crack tip, generating a curve which does not display any softening response. Reducing element size to 1.0mm enables to capture the initiation of the stiffness degradation process.

A realistic prediction of the maximum load can already be obtained with this mesh density, in spite of the spurious oscillations displayed during fracture propagation, the amplitude of which tends to become less significative as mesh size furtherly decreases ($size = 0.6$mm).

For the recommended size value, 0.5mm, correlation with experimental data is very good. Consequently, further refinement of the mesh is neither required nor convenient: too small ratios between in-plane dimensions and thickness of the shell elements may lead, in fact, to an unproper model response that may require their substitution with solid elements.

Last configuration analysed ($size = 0.4$mm) shows the complexity and unpredictability of the dependance of the results upon the mesh density: a completely different response in the nonlinear regime and a sudden increase in the percentage error with respect to reference data is obtained.

To conclude, it was demonstrated that for the AS4/PEEK, Hillerborg's model and Turon's recommentadations provide a useful guidance to properly select the size of cohesive elements ahead of the crack tip. Nonetheless, careful sensitivity studies have to be conducted to establish an optimal mesh density, since predicted response shows a great dependence upon discretization level. For element sizes of about 1mm or less, though, sufficiently realistic results can be computed, since predicted responses display an error of less than the 10% with respect to experimental data. Best agreement with experimental response was obtained with a mesh size of 0.5mm.

Sensitivity analysis to mesh density outside the cohesive zone

Three mesh refinement levels in the pre-cracked and undamaged regions were investigated: $fc = 4$, $fc = 2$ and $fc = 1$, mesh patterns of which are shown in Figure 4.8a, 4.8b and 4.8c respectively (with $size$=0.5mm). Mesh size outside the cohesive zone region seems to have no effect upon the DCB specimen response as curves overlap (Figure 4.9). To minimize the CPU time, fc was set to 4.

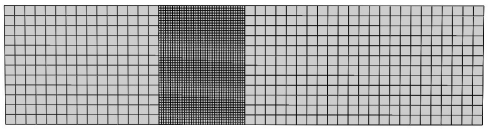

(a) fc=4.

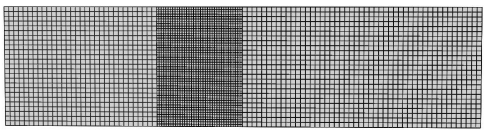

(b) fc=2.

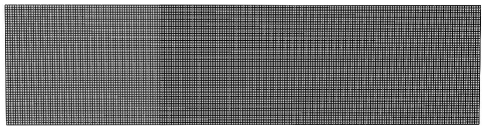

(c) fc=1.

Figure 4.8: Mesh pattern of the DCB specimen for different fc values.

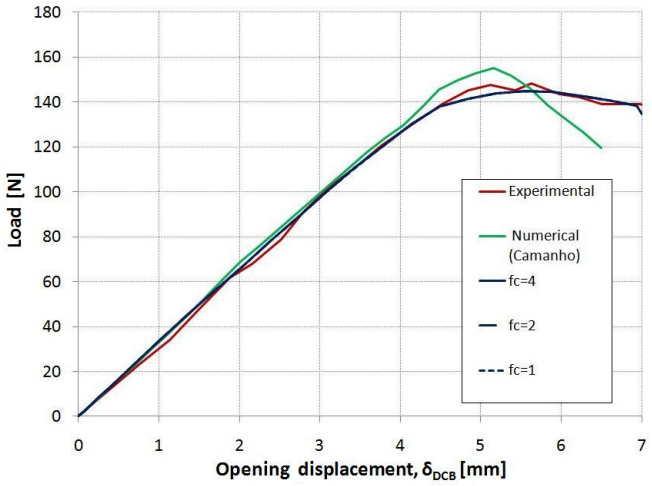

Figure 4.9: Sensitivity to mesh density outside the cohesive zone of the DCB model.

4.2.3 Results of the DCB model

Response predicted by the 6516-element DCB model calibrated according to parameter values reported in Table 4.6 are in very good agreement with experimental data as reported in Figure 4.10: peak load is underpredicted by only 1.7% and accurate results during delamination propagation are provided.

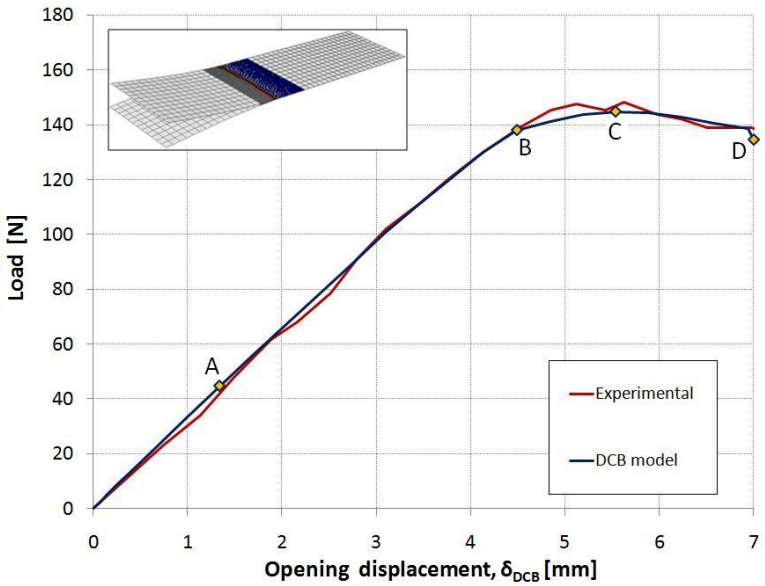

Figure 4.10: Load vs. displacement of the calibrated DCB model.

In addition to the load-displacement curve, the numerical model enables to track the progressive damage process during the applied opening displacement history. For each displacement increment, damage maps of the specimen can be obtained by evaluating the overall damage variable d (SDEG in Abaqus/Standard) at each of the cohesive elements placed ahead of the delamination front. A d value of 0.00 indicates that the element has not undergone any damage; a d value of 1.00, on the contrary, indicates that the stiffness of the element has completely degraded and that upper and lower shell elements are not connected together by cohesive forces anymore. Through these damage maps, four remarkable points were identified on the predicted load-displacement curve, as indicated in Figure 4.10:

- *Point A: Damage initiation* (Figure 4.11a). Onset of the softening process along the first row of cohesive elements around the initial delamination front.
- *Point B: Onset of delamination growth* (Figure 4.11b). Commencement of the stiffness degradation.
- *Point C: Peak load* (Figure 4.11c). Required opening load starts to decrease due to severe interface degradation.
- *Point D: Final opening displacement*(Figure 4.11d). Predicted final delaminated and damaged areas can be visualized.

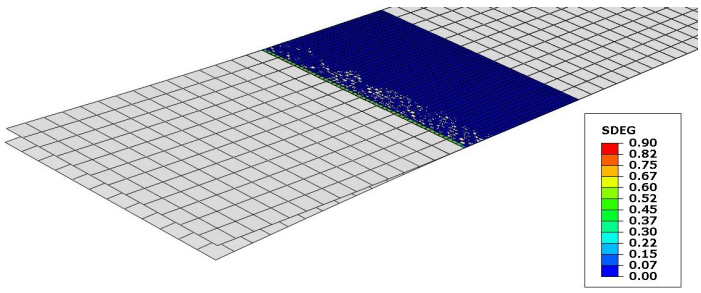

(a) *Damage initiation.*(A): $\delta_{\mathrm{DCB}} = 1.34\mathrm{mm}$, $P = 44.7\mathrm{N}$.

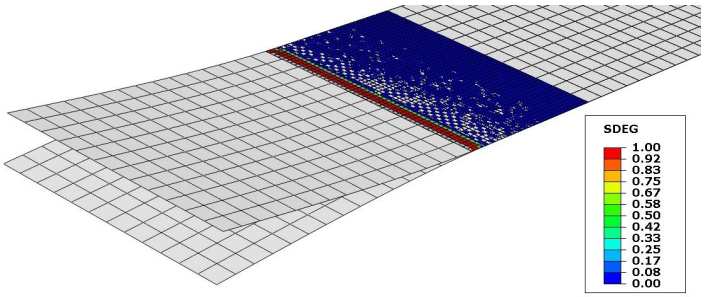

(b) *Onset of delamination growth.*(B): $\delta_{\mathrm{DCB}} = 4.49\mathrm{mm}$, $P = 138.1\mathrm{N}$.

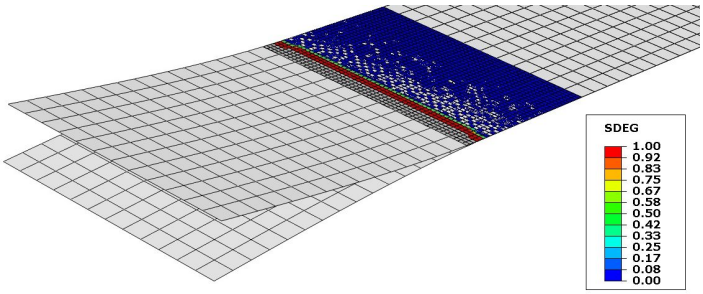

(c) *Peak load configuration.*(C): $\delta_{\mathrm{DCB}} = 5.54\mathrm{mm}$, $P = 144.8\mathrm{N}$.

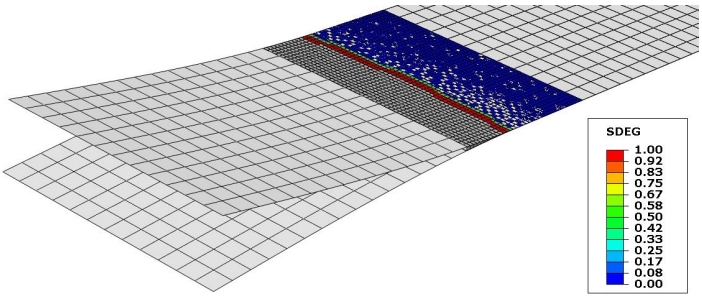

(d) *Final configuration.*(D): $\delta_{\mathrm{DCB}} = 7\mathrm{mm}$, $P = 134.6\mathrm{N}$.

Figure 4.11: Damage and delamination evolution (DCB simulation).

4.3 Numerical analysis of the ENF model

This Section reports the implemented methodology to determine a suitable set of parameters for the ENF model.

4.3.1 Boundary conditions and prescribed displacements

Configuration and boundary conditions of the ENF specimen are shown in Figure 4.12. Vertical displacement v_m at the middle point of the specimen was applied linearly in small incremenents until a maximum value of 4.5mm. Bottom nodes at the pre-damaged end of the specimen were constrained along the y- and z- directions. At the opposite end, all displacement components were constrained.

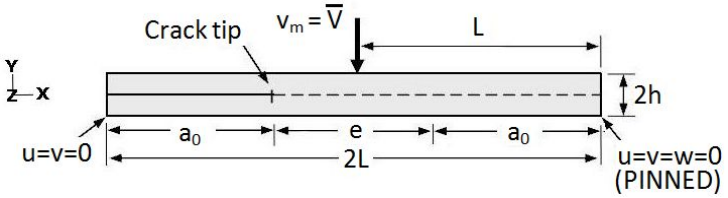

Figure 4.12: Boundary conditions and prescribed displacements in the ENF model.

4.3.2 Parametric studies

Sensitivity studies were performed to investigate the influence of parameters presented in Section 4.1.4 upon the load-displacement curve obtained by the ENF model. Results presented herein were generated varying one parameter at a time with respect to the parameter set that fits better experimental data among those investigated. Parameter values of this set are summarized in Table 4.9. Corresponding load-displacement curve is plotted in blue solid line in figures reported as follows.

Penalty stiffness, K_p (N/mm^3)	10^6
Viscous regularization factor, μ	10^{-4}
Fine-coarse ratio, fc	4
Element size in the cohesive zone, $size$ (mm)	0.6

Table 4.9: Selected set of parameters for the ENF model.

It can be noticed that, except the size of the elements within the cohesive zone region, the other parameters were set like in the DCB model.

Sensitivity analysis to penalty stiffness

It was demonstrated in Section 4.2.2 that, given a penalty stiffness value, adjustment of the numerical curve can be relied on the proper calibration of the viscous regularizaton factor.

Therefore, K_p value used in the DCB analyses was employed in ENF models as well.

Sensitivity analysis to viscous regularization factor

Like in the DCB model, three different viscous regularization factors were investigated.

For $\mu = 10^{-3}$, the specimen does not exhibit any softening response for the simulated midpoint displacement range. On the contrary, the introduction of too little amount of artificial viscous energy ($\mu = 10^{-5}$) induces an overestimation of the load drop in the delamination propagation zone of the curve, even though the maximum load is accurately predicted. Finally, the selected value, 10^{-4}, generates an intermediate response that fits well to experimental results.

Estimated peak load values are reported in Table 4.10.

	P_{max} (N)	error (%)
Experimental [37]	734	0
Numerical (Camanho) [26]	697.6	-4.96
$\mu = 1E-3$	No softening response	
$\mu = 1E-4$	719.9	-1.92
$\mu = 1E-5$	718.57	-2.1

Table 4.10: Maximum loads in Figure 4.13.

Figure 4.13 shows how the amount of artificial viscous dissipation affects the response during delamination propagation under pure mode II loading.

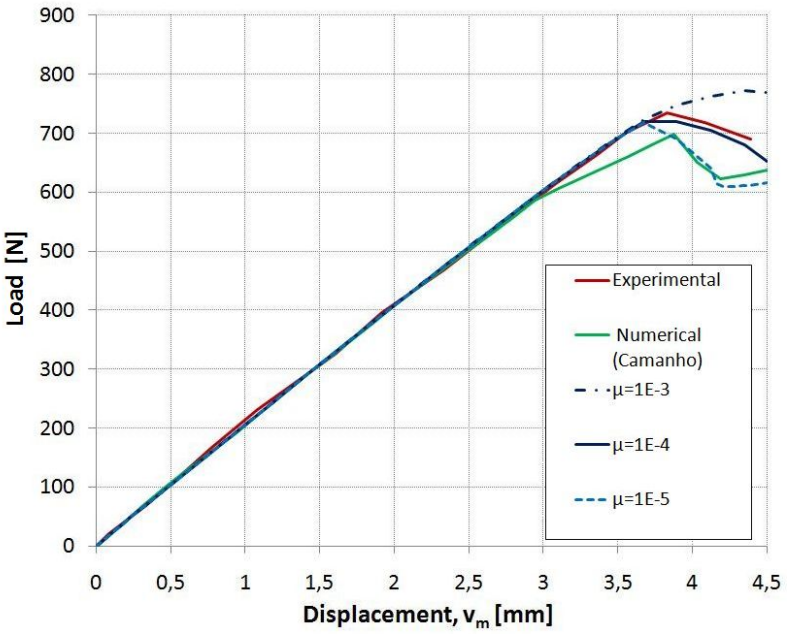

Figure 4.13: Sensitivity to viscous regularization factor of the ENF model.

Sensitivity analysis to element size within the cohesive zone region

Similarly to the DCB model, estimations of the length l_{czII} of the cohesive damaged zone for pure mode II delamination were computed substituting values in Tables 4.4 and 4.5 into Equation (4.3), valid for an infinite body under remote loading:

$$l_{\mathrm{czII}} = ME_{22}\frac{G_{\mathrm{IIC}}}{S^2} \tag{4.3}$$

in which $M = 1$ for the Hillerborg's model used herein. Length l_{eII} of the cohesive and shell elements is given by:

$$l_{\mathrm{eII}} = \frac{l_{\mathrm{czII}}}{N_e} \tag{4.4}$$

where $N_e = 3$, as recommended in [51]. Length of the cohesive damaged zone calculated with Equation (4.3) is equal to $l_{czII} = 1.7$ mm, which using Equation (4.4) yields to a suggested element size of $l_{\mathrm{eII}} = 0.6$ mm, sligthly greater than for the DCB test.

Mesh-dependency of the response is shown in Figure 4.14. Table 4.11 reports the obtained maximum load values. Numbers between brackets denote the aproximate number of elements within the cohesive damaged zone associated to each mesh size.

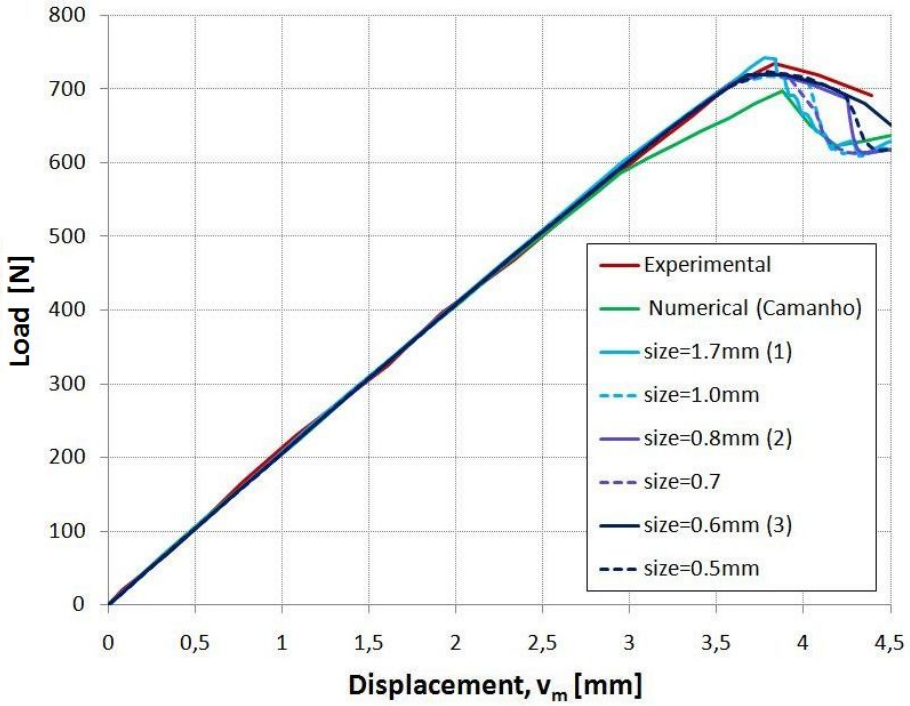

Figure 4.14: Sensitivity to mesh density in the cohesive zone of the ENF model.

	P_{max} (N)	error (%)
Experimental [37]	734	0
Numerical (Camanho) [26]	697.6	-4.96
size = 1.7mm (1)	742.7	1.19
size = 1.0mm	717.9	-2.19
size = 0.8mm (2)	721.8	-1.66
size = 0.7mm	720.3	-1.87
size = 0.6mm (3)	719.9	-1.92
size = 0.5mm	724.1	-1.35

Table 4.11: Maximum loads in Figure 4.14.

Computed results indicate that mesh density within the cohesive zone region is less critical for the ENF test than for the DCB test. Predicted load-displacement curves are, in fact, consistent with experimental data even for the coarsest mesh considered ($size$=1.7mm). Furthermore, percentage error of estimated maximum loads stays lower than 2.5%. Hence,

it can be concluded that the simulation of progressive delamination of an AS4/PEEK structure subjected to Mode II does not require a particularly high mesh refinement. Moreover, response during delamination propagation is not as influenced by discretization level as the DCB model.

A high density mesh was selected though, with an element length of 0.6mm. This value yields a good agreement with experimental curve until the end of the simulation without a significant increase of the analysis time compared to other coarser meshes investigated.

Sensitivity analysis to mesh density outside the cohesive zone

Influence of mesh density outside the cohesive zone region on the predicted response is almost negligible. Figure 4.15 shows that even for $fc = 4$, computed response is in good agreement with experimental results.

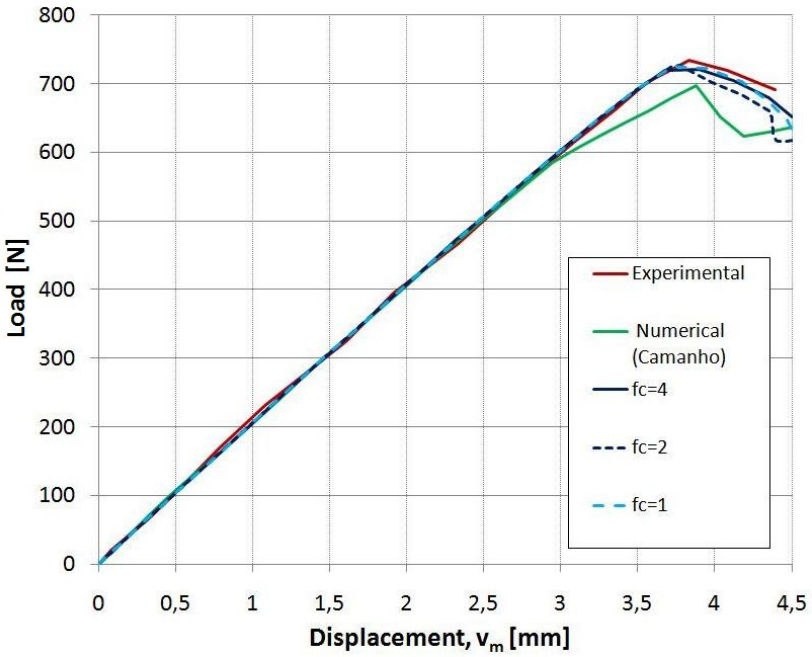

Figure 4.15: Sensitivity to fine-coarse ratio of the ENF model.

Nevertheless, the increment of the CPU time due to the use of high density meshes in the pre-cracked and undamaged zones is much more consistent than what observed for the DCB model. The reason for this may be the non negligible computational cost associated to the contact algorithm implemented on the internal faces of the sub-laminates in the pre-cracked region, not required by the DCB specimen.

4.3.3 Results of the ENF model

Load-displacement curve predicted by the 8568-element ENF model calibrated according to parameter values reported in Table 4.9 are in good agreement with experimental results: maximum load is underpredicted by only 1.92% and response during fracture growth is accurately computed, as displayed in Figure 4.16.

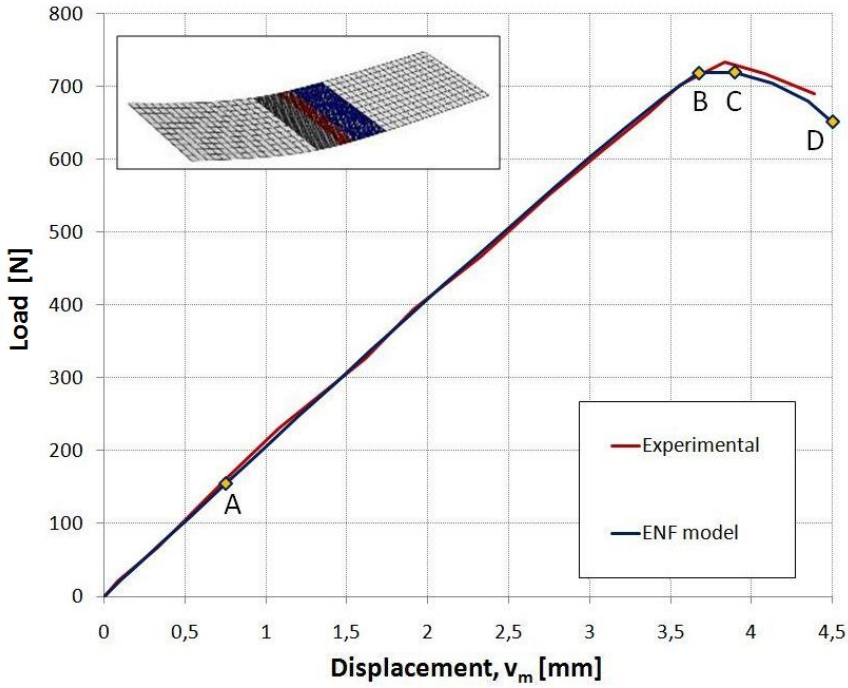

Figure 4.16: Load vs. displacement of the calibrated ENF model.

Similarly to the DCB simulation, damage maps of the specimen can be plotted through the evaluation of the overall damage variable d (SDEG in Abaqus/Standard) at each of the cohesive elements placed ahead of the crack tip. A d value of 0.00 indicates that the element is not affected by damage; a d value of 1.00, on the contrary, denotes that the interlaminar interface is completely damaged and, therefore, adjacent laminas are not tied together by cohesive forces anymore.

By means of the obtained damage maps, four remarkable points were identified on the predicted response curve:

- *Point A: Damage initiation* (Figure 4.17a). Commencement of the softening process along the first row of cohesive elements at the initial delamination front.

- *Point B: Onset of delamination growth/ Point C:Peak load* (Figure 4.17b). Unlike the DCB model, initiation of delamination propagation and the maximum load occur almost consecutively.
- *Point D: Final displacement*(Figure 4.17c). Predicted final delaminated and damaged areas can be visualized.

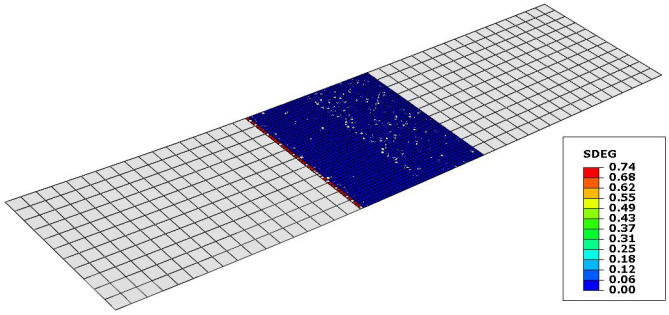

(a) *Damage initiation.*(A): $v_m = 0.75$mm, $P = 154.7$N.

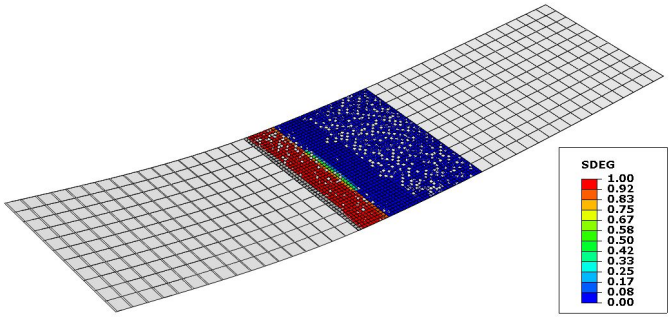

(b) *Onset of delamination growth*(B): $v_m = 3.67$mm, $P = 719.0$N / *Peak load*(C): $v_m = 3.90$mm, $P = 719.9$N

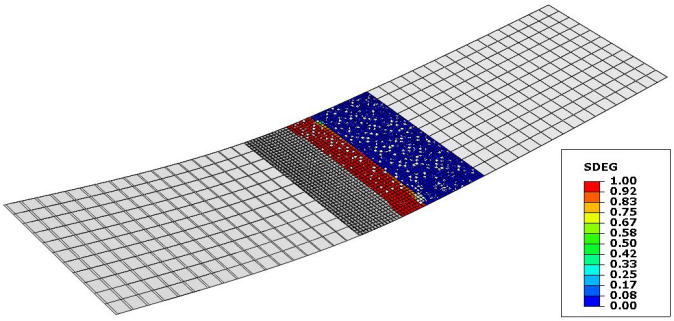

(c) *Final configuration.*(D): $v_m = 4.5$mm, $P = 651.5$N.

Figure 4.17: Damage and delamination evolution during the ENF simulation.

4.4 Determination of a set of parameters for fracture analysis under general loading conditions

Sensitivity studies carried out in Sections 4.2.2 and 4.3.2 yielded two different suitable sets of cohesive-zone-related parameters to simulate delamination under pure mode I and pure mode II loading conditions respectively. As it can be noticed in Tables 4.6 and 4.9, these sets only differ between them in the mesh size employed within the cohesive zone region. Three element sizes were examined as possible values to include in the set of parameters to be used under general loading conditions:

- $size$=0.5mm, corresponding to the value obtained from the DCB analyses.
- $size$=0.6mm, corresponding to the value obtained from the ENF analyses.
- $size$=1.0mm, corresponding to the coarsest mesh, among those investigated, that provided sufficiently realistic predictions for both tests simultaneously.

Load-displacement response of the DCB and ENF models obtained with these mesh sizes as well as percentage errors of the predicted maximum loads with respect to experimental values are reported in Figure 4.18 and Table 4.12 respectively.

Crossed analyses were firstly conducted to compare the DCB-based and the ENF-based element sizes and demonstrated that while the predicted ENF response with the DCB-based mesh density ($size$=0.5mm) continued to agree well with experimental data, the predicted DCB response wth the ENF-based mesh density ($size$=0.6mm) failed to reproduce the nonlinear behavior after the onset of delamination growth.

However, such a fine mesh may cause the simulation time to dramatically when analysing more complex loading conditions and problems, such as the MMB test (see Section 5.3 or the buckling response of damaged composite panels reported in the following Chapters. For this reason, comparison with results computed with a coarser mesh ($size$=1.0mm) was also established.

Its corresponding DCB solution, displayed in Figure 4.7, shows some spurious oscillations, which, however, do not significantly alter the nonlinear response during damage propagation. With regard to the ENF model,

a slightly anticipated load drop can be noticed in the load-displacement curve. Nevertheless, the effects of damage on the stiffness and strength of the ENF specimen can be reliably assessed, as this drop manifests itself after the initiation of fracture propagation and after the maximum load is attained.

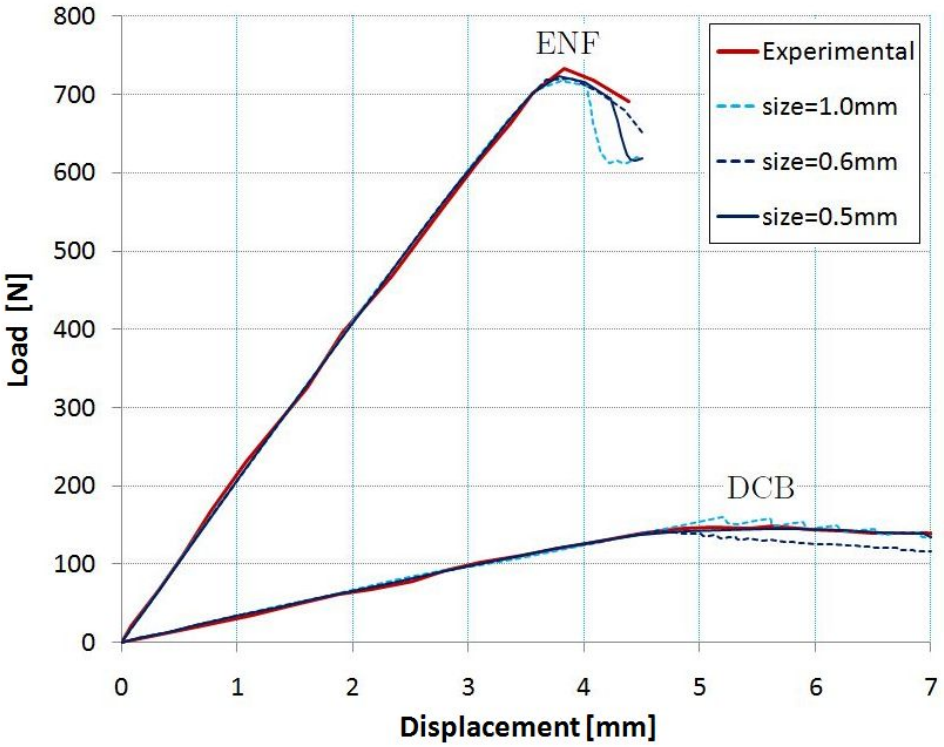

Figure 4.18: Comparison of DCB and ENF results for different mesh sizes.

	DCB error (%)	ENF error (%)
size=1mm (coarsest mesh)	8.70	-2.19
size=0.6mm (ENF set)	-6.11	-1.92
size=0.5mm (DCB set)	-1.70	-1.35

Table 4.12: Percentage error with respect to experimental maximum load.

Providing a similar accuracy to that obtained with the other two finer meshes, an element size of $1mm$ yielded, however, a significant reduction in computing times (see Section 5.3). With this choice, in fact, the number of elements of the DCB and ENF models reduces from 6516 to 1560 and

from 8568 to 2646 respectively. For this reason, the element size within the cohesive zone region was finallyset to 1.0mm.

To conclude, the determined set of parameters for the simulation of delamination under general mixed-mode loading conditions within an AS4/PEEK laminate is shown in Table 4.13. Validation of this set was performed through MMB tests reported in Chapter 5.

Penalty stiffness, K_p (N/mm^3)	10^6
Viscous regularization factor, μ	10^{-4}
Fine-coarse ratio, fc	4
Element size in the cohesive zone, $size$ (mm)	1.0

Table 4.13: Determind set of parameters for simulating delamination mechanisms in an AS4/PEEK laminate.

Chapter 5

MMB analyses: validation of the set of parameters

In this Chapter, the set of parameters reported in Table 4.13 obtained from parametric studies upon DCB and ENF specimens was used to simulate fracture mechanisms under mixed-mode loading conditions within a unidirectional AS4/PEEK laminate. At this aim, the MMB test was reproduced at three different mode ratios G_{II}/G_T (0.20, 0.50 and 0.80). Validation of the FEM models was carried out by plotting the predicted load-displacement curves against corresponding experimental response obtained by Reeder [37]. In addition, numerical results computed by Camanho in [26] and Balzani in [54] are reported.

The objective of Chapters 4 and 5 was, hence, to implement and validate a methodology to establish cohesive-model-related requirements through parametric studies on simple DCB and ENF models, that enbled to obtain accurate predictions of fracture evolution under general mixed-mode loading conditions as well.

5.1 Numerical analyses of the MMB tests

The MMB test was simulated at three different mode ratios G_{II}/G_T (0.20, 0.50 and 0.80) using the set of parameters proposed in Table 4.13.

5.1.1 Specimens geometry, mesh pattern and material properties

Figure 4.1 and Tables 4.1 and 4.2 provide geometrical data about the modeled specimens. Details upon the mesh pattern can be found in Figure 4.2 and Table 4.3. Material and interface properties are shown in Tables 4.4 and 4.5.

5.1.2 Boundary conditions

Configuration and boundary conditions of the MMB specimens are shown in Figure 4.12. Similarly to the ENF specimen, bottom nodes at the pre-damaged end of the specimen were constrained along the y- and z- directions. At the opposite end, all displacement components were constrained.

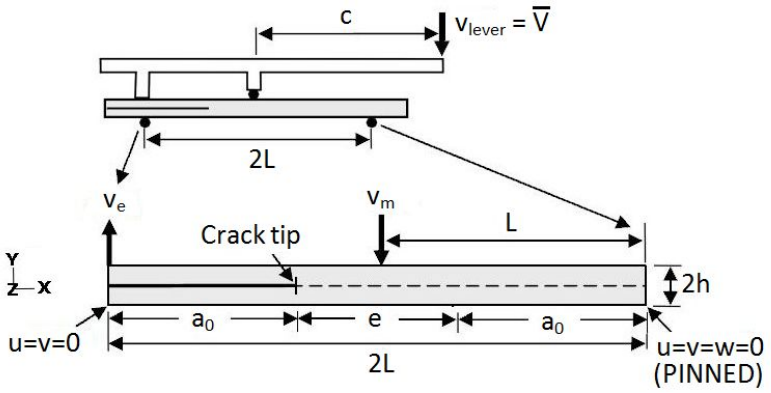

Figure 5.1: Boundary conditions and prescribed displacements in the MMB model.

5.1.3 Determination of the load-point displacement

Information available from the MMB test in [37] relates the load to applied at the end of the lever opposite to the pre-cracked region to the displacement of the load-point. Since the lever was not simulated in the numerical models, it was necessary to calculate the load-point applied displacement v_{lever} and corresponding load P using the information available from the FEM models.

The load-point displacement v_{lever} can be related to the pre-cracked end displacement v_e and the middle-point displacement v_m of the specimen assuming rigid body motion of the loading arm using the following expression [54]:

$$v_{\text{lever}} - \frac{c+L}{L} v_m + \frac{c}{L} v_e = 0 \tag{5.1}$$

This linear combination of nodal degrees of freedom was used to define a linear multi-point constraint in the Abaqus/Standard input file.

Load P required to apply the linear displacement law v_{lever} at the end of the lever was determined from the vertical reactions at the supports (Figure 5.2 [37]), assuming that the weight of the lever is negligible.

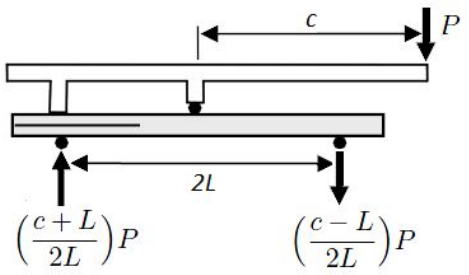

Figure 5.2: Vertical reaction forces at end supports in the MMB specimen.

Averaging values derived from both reaction forces, load P was obtained.

5.1.4 Determination of the length c of the lever arm

The length of the lever arm used in [37] was determined accounting for the weight of the lever. Since the lever was not simulated in the FEM models, the lengths corresponding to the different mode ratios are greater and need to be computed.

It was demonstrated in [37] that:

$$\frac{G_I}{G_{\text{II}}} = \frac{4}{3}\left(\frac{3c-L}{c+L}\right)^2, \qquad \text{for } c \geq \frac{L}{3} \tag{5.2}$$

Combining Equation (5.2) with the definition of the mode ratio $m = G_{\text{II}}/G_T$, the length of the lever c as a function of m and the specimen length $2L$ was obtained:

$$c = \frac{L\left(\frac{L}{2}\sqrt{3\left(\frac{1-m}{m}\right)}+1\right)}{3-\frac{1}{2}\sqrt{3\left(\frac{1-m}{m}\right)}} \tag{5.3}$$

Lengths of the lever arm for each mode ratio used in the FEM model an in the experiments are presented in Table 5.1:

G_{II}/G_T	0.20	0.50	0.80
Numerical c (mm)	109.89	44.60	28.47
Experimental c (mm)	97.4	42.2	27.6

Table 5.1: Lengths of the lever arm for each mode ratio.

5.1.5 Results of the MMB models

Results obtained by the MMB simulations at mode ratios G_{II}/G_T of 0.20, 0.50 and 0.80 are shown in Figures 5.3, 5.4 and 5.5 respectively. Predicted maximum loads are reported in Table 5.2 for the three loading conditions.

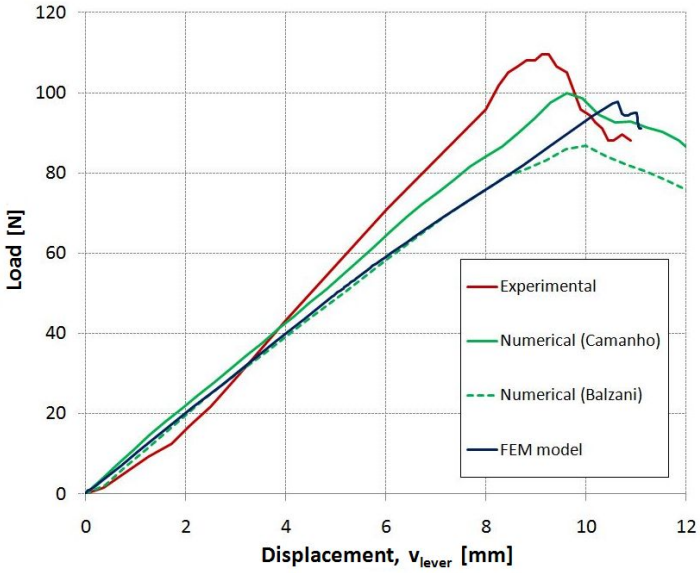

Figure 5.3: Load vs. displacement of the MMB model for G_{II}/G_T= 0.20.

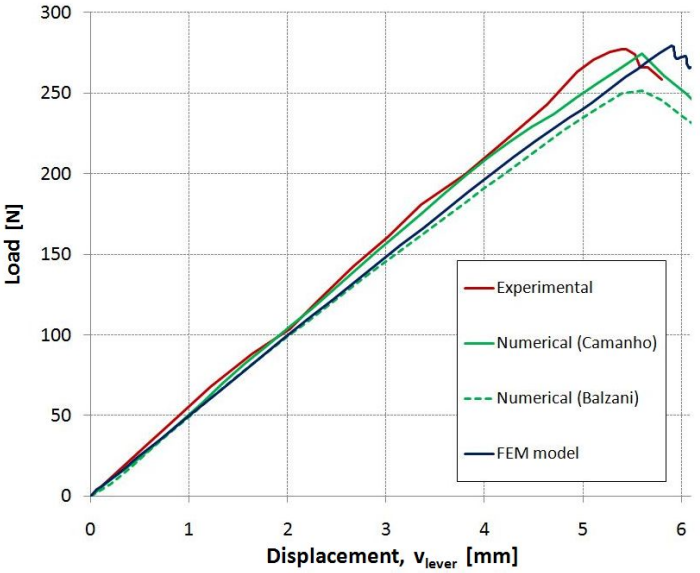

Figure 5.4: Load vs. displacement of the MMB model for G_{II}/G_T= 0.50.

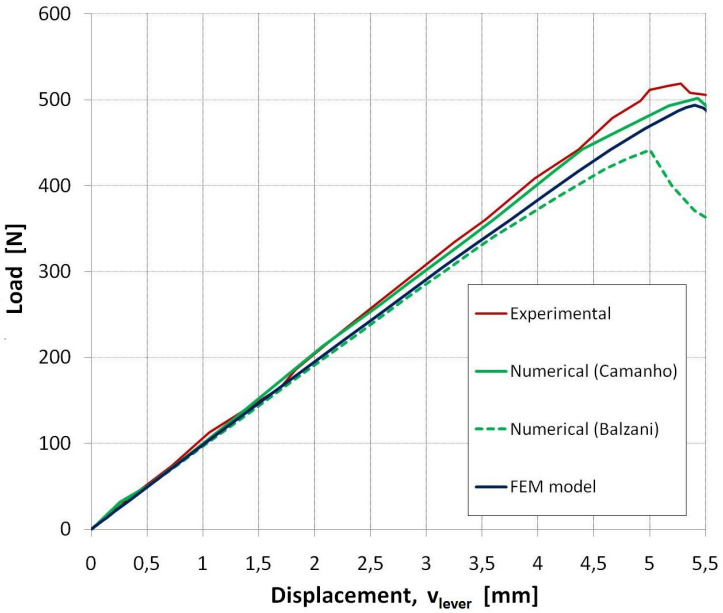

Figure 5.5: Load vs. displacement of the MMB model for G_{II}/G_T= 0.80.

G_{II}/G_T	Curve	P_{max} (N)	error (%)
0.20	Experimental [37]	108.0	0
	FEM model	98.7	-8.61
	Numerical (Camanho)[26]	99.9	-7.59
	Numerical (Balzani)[54]	86.8	-19.70
0.50	Experimental [37]	275.4	0
	FEM model	279.2	1.38
	Numerical (Camanho)[26]	274.5	-0.33
	Numerical (Balzani)[54]	251.4	-19.70
0.80	Experimental [37]	518.7	0
	FEM model	493.5	-5.10
	Numerical (Camanho)[26]	502	-3.22
	Numerical (Balzani)[54]	441.4	-14.90

Table 5.2: Maximum loads in Figure 5.3,Figure 5.4 and Figure 5.5.

Generally speaking, predicted responses using the proposed set of parameters fit well to experimental data and estimations of the maximum loads are sufficiently reliable. Computed solution is, in fact, much more accurate than that obtained by Balzani [54]. Nevertheless, unlike the DCB and ENF tests, numerical models implemented by Camanho [26] show better agreement to experimental curves in all three MMB simulations. No clear explanation can be found to justify this, as detailed information about mesh pattern and cohesive-model parameters used in that analyses is not provided in [26].

The most significant difference between numerical predictions and experimental data corresponds to G_{II}/G_T=0.20. The same behavior can be evidenced in the two numerical works extracted from literature. The reason for this is the fact that the largest difference between the fracture toughness experimentally measured in [37] and the one predicted using the B-K criterion occurs at this mode ratio.

5.2 Concluding remarks

A set of parameters for the numerical analysis of delamination mechanisms in an AS4/PEEK laminate was determined in Chapter 4 from sensitivity studies conducted on DCB and ENF models.

In this Chapter, this set of parameters showed to provide reliable predictions within reasonable CPU times for the MMB test as well (see Section 5.3). Obtained results are summarized in Figure 5.6 and Table 5.3. It can be observed that error stays within a reasonable ±9% with respect to test values. It is worth highlighting, that all implemented models may probably tend to underestimate the size of damaged area at the end of the simulation. The reason for this is that onset of delamination growth is predicted to occur at slightly higher displacement levels than those experimentally measured.

In conclusion, the implemented methodology to set cohesive-model-related parameters was validated under general mixed-mode loading conditions. This fact suggested that the same set of parameters may be valid in more complex fracture problems, such as buckling of composite panels involving delamination propagation investigated in Chapters 6 and 7.

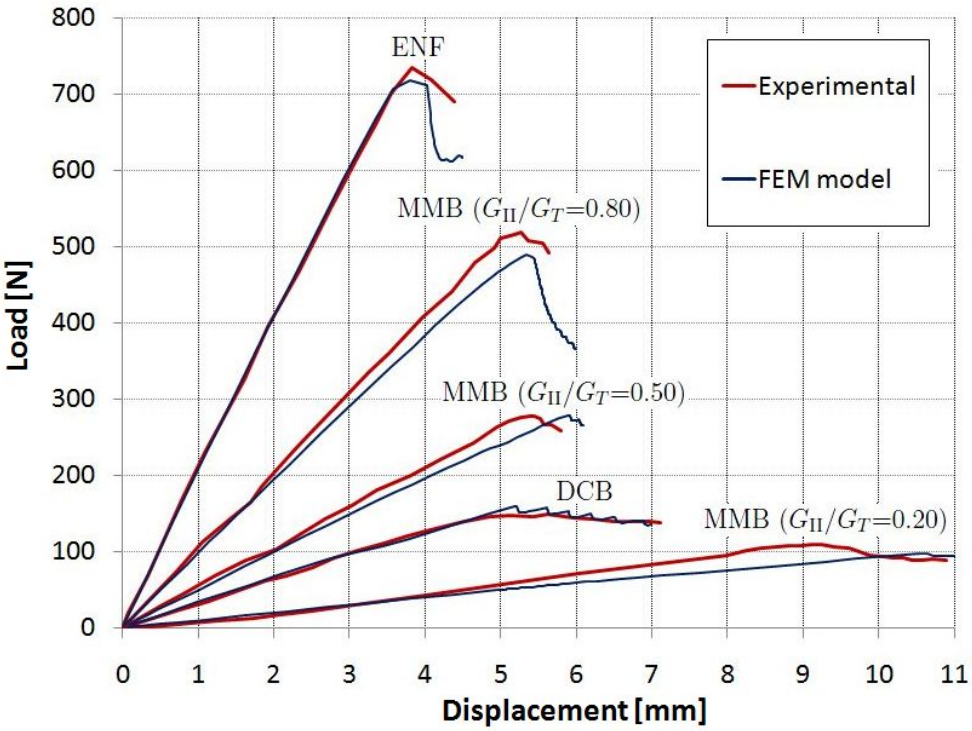

Figure 5.6: Predicted and experimental responses at different mode ratios.

Test	G_{II}/G_T	P_{max} (N)		error
		Experimental [37]	FEM model	(%)
DCB	0.0	147.1	159.9	8.70
MMB	0.20	108.0	98.7	-8.61
	0.50	275.4	279.2	1.38
	0.80	518.7	493.5	-6.52
ENF	1.0	734.0	717.9	-2.19

Table 5.3: Maximum loads in Figure 5.6.

5.3 Computational costs

This Section reports CPU times corresponding to different implementations of the DCB, ENF and MMB finite-element models with the purpose of examining the influence of several model parameters on the required

analysis time and evidencing the conveniency of the determined set of parameters in terms of computational cost.

Table 5.4 provides a summary of the technical specifications of the PC used in the simulations:

PC	OS
Intel(R) Core(TM) i3 M330 @ 2.13GHz. (RAM = 4GB)	Windows 7 Home Premium 64 bit

Table 5.4: Specifications of the PC used in the simulations.

In the following discussions, cohesive-model-related parameters are set as indicated in Table 4.13, unless told otherwise. Maximum loads obtained by the models are reported together with the CPU times to establish a comparison both in terms of accuracy and computational cost. Colored columns in Tables refer to the selected configuration.

5.3.1 Integration scheme

A comparison of CPU times using the fully integrated S4 element and the reduced-integration S4R element is displayed in Figure 5.7. Numbers between brackets denote the time reduction due to the usage of the reduced integration scheme. Predicted maximum loads are reported in Table 5.5.

Test	G_{II}/G_T	P_{max} (N)		
		Experimental [37]	S4R	S4
DCB	0.0	147.1	159.9 (8.70%)	157.6 (6.98%)
MMB	0.20	108.0	98.7 (-8.61%)	97.8 (-9.44%)
	0.50	275.4	279.2 (1.38%)	279.2 (1.38%)
	0.80	518.7	493.5 (-6.52%)	490.2 (-5.49%)
ENF	1.0	734.0	717.9 (-2.19%)	719.0 (-2.05%)

Table 5.5: Maximum loads (S4R vs.S4)

Results show that while analyses employing the S4 element are much more time consuming, accuracy is similar in both cases. Thus, the S4R element was used.

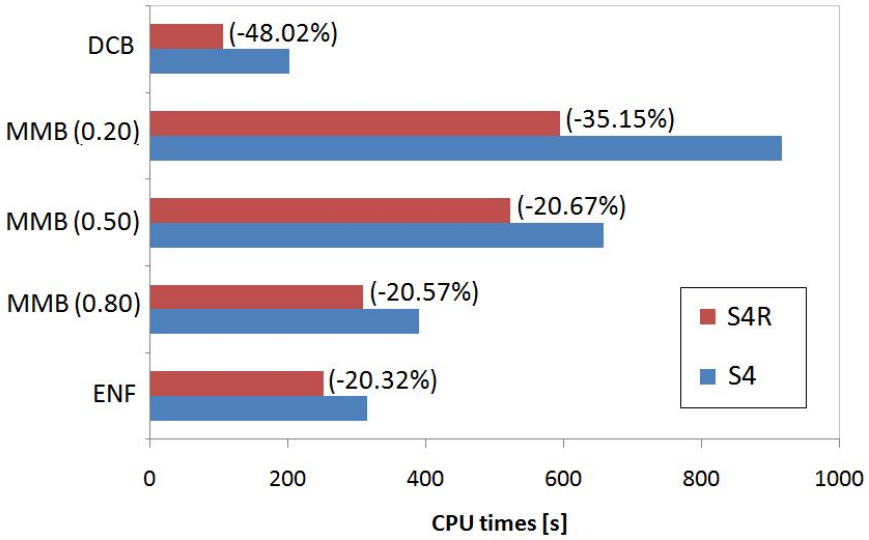

Figure 5.7: Comparison of CPU times (S4R vs S4)

5.3.2 Element size within the cohesive zone region

Two mesh sizes within the cohesive zone region were examined: 1mm (adopted in the selected set of parameters) and 0.5mm (which provided best predictions in the DCB simulation). Computed maximum loads and CPU times are reported in Table 5.6 and Figure 5.8 respectively.

Test	G_{II}/G_T	P_{max} (N)		
		Experimental [37]	$size = 1mm$	$size = 0.5mm$
DCB	0.0	147.1	159.9 (8.70%)	144.8 (-1.70%)
MMB	0.20	108.0	98.7 (-8.61%)	98.3 (-8.98%)
	0.50	275.4	279.2 (1.38%)	281.1 (2.07%)
	0.80	518.7	493.5 (-6.52%)	499.6 (-3.68%)
ENF	1.0	734.0	717.9 (-2.19%)	724.1 (-1.35%)

Table 5.6: Maximum loads (mesh size, cohesive zone region)

Generally speaking, numerical predictions with a smaller element size show a better agreement with respect to experimental data. However, this enhanced accuracy is obtained through a drammatic increase in the computational cost of the model, specially at high mode II regimes for which contact between the faces of the pre-cracked region plays a dominant role. Therefore, the coarser mesh was adopted.

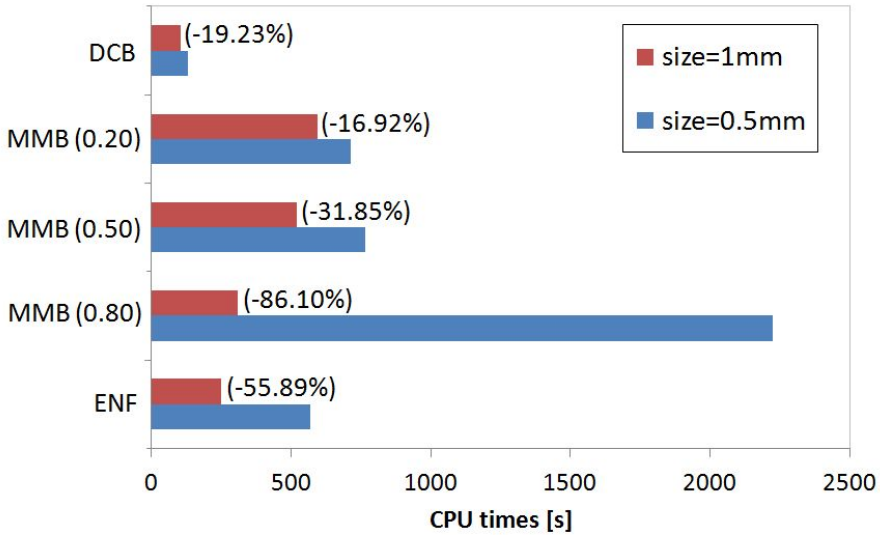

Figure 5.8: Comparison of CPU times (mesh size, cohesive zone region)

5.3.3 Discretization pattern

DCB, ENF and MMB models were implemented with a uniform mesh (without any kind of constraint among nodes on the same sublaminate) to assess the gainings in terms of computational cost derived from defining a coarser mesh outside the cohesive zone region ($fc = 4$). Predicted maximum loads and CPU times are reported in Table 5.6 and Figure 5.8 respectively.

Test	G_{II}/G_T	P_{max} (N)		
		Experimental [37]	$fc = 4$	Uniform
DCB	0.0	147.1	159.9 (8.70%)	157.9 (7.20%)
MMB	0.20	108.0	98.7 (-8.61%)	96.1 (-11.02%)
	0.50	275.4	279.2 (1.38%)	282.2 (2.47%)
	0.80	518.7	493.5 (-6.52%)	493.1 (-4.94%)
ENF	1.0	734.0	717.9 (-2.19%)	728.5 (-0.75%)

Table 5.7: Maximum loads (discretization pattern)

Results computed with a uniform fine discretization pattern were slightly more accurate than with a mesh consisting of different refinement levels. However, analyses with the uniform mesh were so much more time consuming that it was more convenient to adopt the other approach.

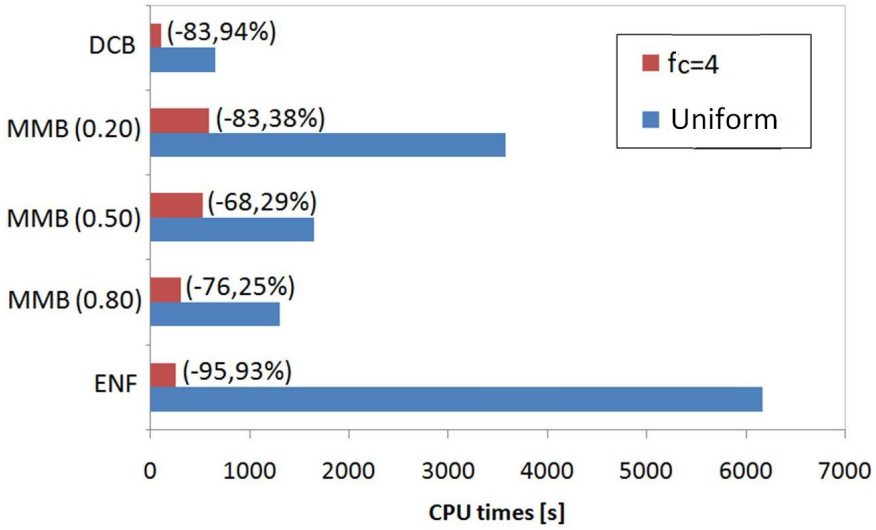

Figure 5.9: Comparison of CPU times (discretization pattern)

5.3.4 Concluding remarks

This investigation evidenced the importance of considering the computational cost, together with the accuracy, as a quality index when implementing FEM models.

CPU times of each of the models examined in this Section are summarized in Table 5.8. MODEL corresponds to the adopted configuration: S4R elements, $size = 1mm$ and $fc = 4$.

Test	G_{II}/G_T	CPU times (s)			
		MODEL	S4	$size = 0.5mm$	Uniform
DCB	0.0	105	202	130	654
MMB	0.20	594	916	715	3575
	0.50	522	658	766	1646
	0.80	309	389	2223	1301
ENF	1.0	734.0	315	569	6164

Table 5.8: Maximum loads (discretization pattern)

Chapter 6

Delamination buckling: model validation

Compressive behavior of an HTA/6376C laminated plate containing an artificial circular delamination was investigated by means of FEM simulations. Comparison was established with experimental work carried out by Nilsson ed al. in [55] on the same damaged HTA/6376C specimen in order to validate results.

The same set of parameters determined for the AS4/PEEK in Chapter 4 was adopted to ensure a proper representation of delamination evolution throughout the analysis. Similar mechanical and interfacial properties of both materials suggested that mesh discretization pattern, penalty stiffness and viscous regularization factor inherited from the AS4/PEEK studies may work properly for the HTA/6376C as well. In addition, sensitivity studies were performed to gain understanding on the effect of parameters usually involved in buckling problems solved through a nonlinear static approach.

Conclusions reached from these analyses were very useful to implement models presented in Chapter 7, in whichthe effect of delamination size, depth and shape upon the compressive response and failure of an AS4/PEEK panel was examined. Experimental data regarding compression tests on delaminated plates was not found in literature for this material and tests on the actual specimens were not performed in this work. Thus, numerical investigation reported in this Chapter was a necessary intermediate stage to gain comprehension on the modelling of delamination buckling mechanisms as well as to validate the usage of the set of parameters found in Chapter 4 in such complex problems.

6.1 Description of the FEM models

Geometry, material properties, boundary conditions and mesh pattern of the investigated specimen are discussed in this Section.

6.1.1 Geometry of the damaged specimen

Dimensions of the HTA/6376C panel are given in Figure 6.1 [55].

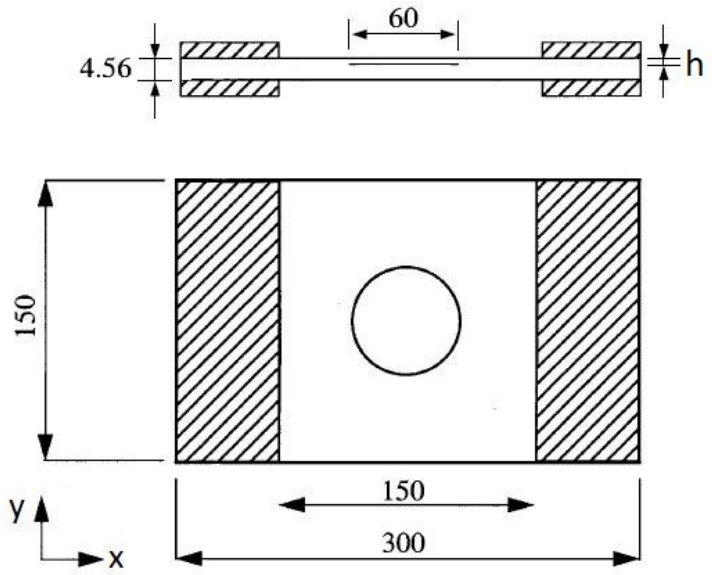

Figure 6.1: Geometry of the damaged HTA/6376C plate specimen (lengths in mm).

Carbon fiber/epoxy laminated plates tested in [55] consist of a cross-ply layup $[(90^o/0^o)_{17}/90^o]$, with 0^o-direction parallel to the loading direction (x_1 direction). Each of the 35 UD plies has a nominal ply thickness of 0.13mm. Steel tabs were bonded to the plate, giving a free length of $150mm$. A 25μ thickness Teflon insert was implanted to simulate an initial circular 60mm diameter delamination, which was placed at a different depth in each coupon. Through-the-thickness location of the insert corresponding to the specimen chosen to validate the FEM models is reported in Table 6.1. In the stacking sequence, // denotes the presence of a delamination.

Stacking sequence	h (mm)
$[90^o/(0^o/90^o)_3//(0^o/90^o)_{14}]$	0.91

Table 6.1: Location of the circular delamination within the HTA/6376C plate specimen.

6.1.2 Material properties

Laminates were manufactured from HTA/6376C prepregs consisting of cured epoxy matrix reinforced with continuous UD high strength carbon fibers. Properties of these prepregs are shown in Table 6.2 [56, 57].

E_{11} (GPa)	$E_{22} = E_{33}$ (GPa)	$G_{12} = G_{23}$ (GPa)	G_{23} (GPa)	$\nu_{12} = \nu_{13}$	ν_{23}	N (MPa)	$S = T$ (MPa)
131	11.7	5.2	3.9	0.3	0.5	30	30

Table 6.2: Material properties (HTA/6376C).

Average values of interlaminar fracture toughnesses experimentally measured by Juntti [56] at different mode ratios are given in Table 6.3.

G_{II}/G_T	0	0.37	0.50	0.63	1.0
$G_C(kJ/m^2)$	0.260 (G_{IC})	0.325	0.440	0.650	1.025 (G_{IIC})

Table 6.3: Interlaminar fracture toughness (HTA/6376C).

Fracture evolution was simulated using the same set of parameters determined for the AS4/PEEK. Being mechanical and interfacial properties of both materials of the same order of magnitude (properties of the AS4/PEEK are reported in Table 4.4), the found set was expected to yield accurate results for the HTA/6376C as well. In spite of the small differences, lower fracture toughnesses and interlaminar tensile and shear strengths indicated a more fragile fracture behavior of HTA/6376C plates.

The parameter η for the B-K criterion to predict delamination propagation was determined through the procedure explained in [26] from experimental data shown in Table 6.3. Considering the pair $((G_{\mathrm{II}}/G_T), (G_T)_j)$ as the experimental values and n as the number of data points obtained at mode ratios different than 0 or 1.0, the problem can be posed as a least-square fitting. Let ϵ be the error committed by the least-square curve:

$$\epsilon = \sum_{\mathrm{j}=1}^{n} \left[(G_T)_j - G_{\mathrm{IC}} - (G_{\mathrm{IIC}} - G_{\mathrm{IC}}) \left(\frac{G_{\mathrm{IIC}}}{G_T} \right)_j^{\eta} \right]^2 \tag{6.1}$$

The minimization of ϵ, namely, $d\epsilon/d\eta = 0$, yields to:

$$\sum_{\mathrm{j}=1}^{n} \left[(G_T)_j - G_{\mathrm{IC}} - (G_{\mathrm{IIC}} - G_{\mathrm{IC}}) \left(\frac{G_{\mathrm{IIC}}}{G_T} \right)_j^{\eta} \right] \left(\frac{G_{\mathrm{II}}}{G_T} \right)_j^{\eta} \ln \left(\frac{G_{\mathrm{II}}}{G_T} \right)_j = 0 \tag{6.2}$$

A value of $\eta = 1.884$ is obtained from the solution of Equation (6.2) for the experimental data in Table 6.3. The prediction of the mixed-mode fracture toughness of the HTA/6376C using the B-K criterion with the determined η value over the entire range of mode ratio is depicted in Figure 6.2. Largest difference between the B-K criterion and the experimental results occurs for $G_{\mathrm{II}}/G_T = 0.37$, as shown in Table 6.4.

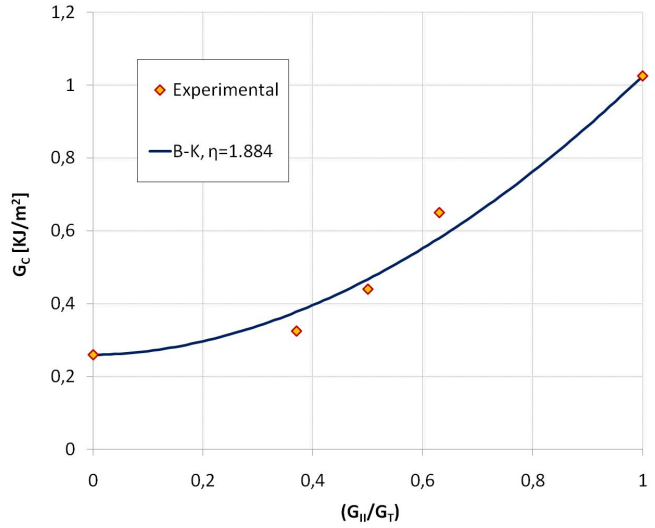

Figure 6.2: Predicted mixed-mode fracture toughness for the HTA/6376C using the B-K criterion.

G_{II}/G_T	Experimental G_C (KJ/m^2)	Predicted G_C (KJ/m^2)	Error (%)
0.37	0.325	0.377	-16.00
0.50	0.467	0.467	-6.14
0.63	0.650	0.580	10.77

Table 6.4: Experimental and predicted fracture toghnesses for the HTA/6376C.

6.1.3 Mesh pattern

The HTA/6376C delaminated specimen was modeled with two layers of reduced-integrated S4R shell elements, each layer simulating one of the two sublaminates.

Similarly to the DCB, ENF and MMB models, three levels of mesh refinement were considered throughout the specimen as shown in Figure 6.3:

- *Delaminated region*, where the circular 60mm diameter Teflon insert is located. Contact was implemented to prevent interpenetration between the upper and lower sublaminates throughout the simulation.
- *Cohesive zone region*, where delamination growth may occur. A layer of cohesive elements was placed between upper and lower shell elements to simulate damage evolution within the delamination plane. An external diameter of 100mm showed to be enough to track the extension of interlaminar debonding even at high postbuckling regimes.
- *Undamaged region*, where delamination propagation shall not occur. The upper and lower layers of S4R elements were connected together through beam type multi-point constraints, simulating a perfect bond during the whole analysis.

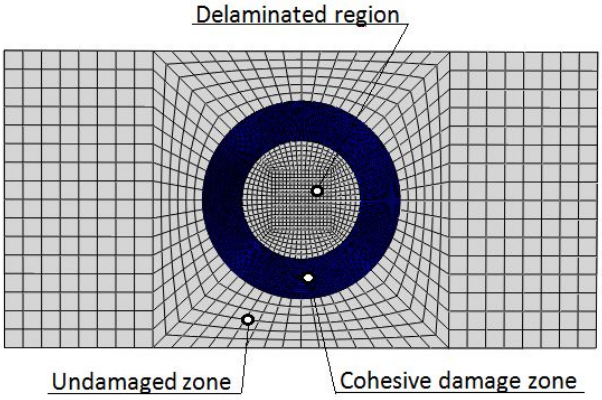

Figure 6.3: Mesh pattern of the HTA/6376C damaged specimen.

Finally, tie constraints were applied onto nodes located along interfaces between the cohesive zone region, where a fine mesh is required to correctly capture the stress field ahead of the crack tip, and the adjacent parts of the model, which do not require such a high level of refinement.

6.1.4 Boundary conditions

The clamping of the specimen to the test machine through the steel tabs was simulated constraining the out-of-plane displacement of nodes located

on the clamped areas, as well as the in-plane component perpendicular to loading direction. Since no anti-buckling guides were used in [55] to avoid the premature buckling of the central part of the plate, unloaded edges were not constrained. To prevent rigid translation along the loading direction, an addition nodal constraint was added to the real boundary conditions. This constraint does not introduce any overconstraint into the problem since in-plane compressive loads are equilibrated. Reaction force at this node is consequently zero. Axial displacement along $x1$-direction was prescribed on both specimen edges to perform the simulation in a displacement control mode. Boundary conditions and applied displacements are shown in Figure 6.4.

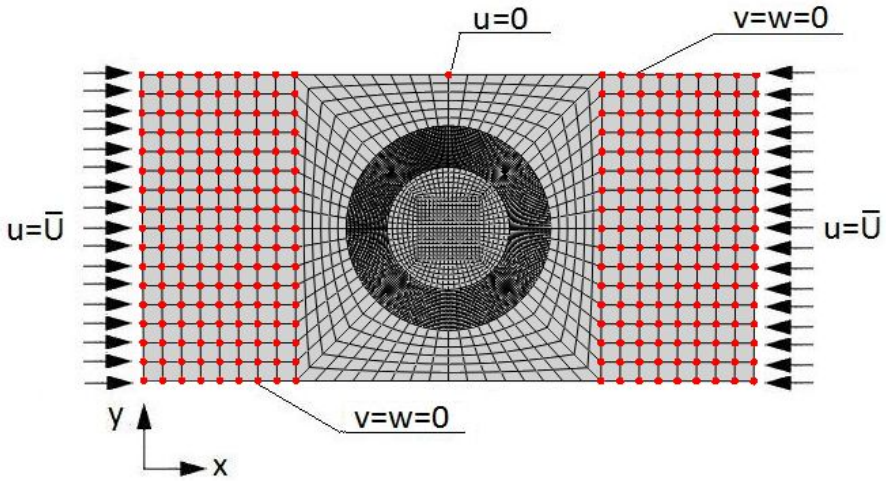

Figure 6.4: Boundary conditions and prescribed displacements in the HTA/6376C models.

6.2 Parametric studies

Several sensitivity studies were carried out to investigate the influence of various parameters upon the correlation between in-plane load and central out-of-plane displacement of both sublaminates:

- *Imperfections* introduced to the nominal geometry of the panel.
- *Viscous regularization factor.*
- *Mesh density* in the delaminated and undamaged regions. Element size within the cohesive zone region was set to $1mm$, as determined for the AS4/PEEK.

Starting values of the parametric studies reported as follows were those inherited from simulations performed in Chapters 4 and 5 upon AS4/PEEK specimens and are shown in Table 6.5:

Mesh parameters	
Imperfections (amplitude and shape)	No imperfection
Fine-coarse ratio, fc	4
Element size in the cohesive zone, $size$ (mm)	1.0
Cohesive zone model parameters	
Penalty stiffness, K_p (N/mm^3)	10^6
Viscous regularization factor, μ	10^{-4}

Table 6.5: Starting values of the parametric studies on the HTA/6376C models.

Sensitivity analysis to imperfections

Imperfections were introduced by initial out-of-plane deflections that perturbate the nominal geometry of the damaged HTA/6387C plate in order to trigger the local buckling of the thinnes sublaminate. Models without initial imperfections, in fact, did not show any opening of the delamination, and unlike experimental results, collapse occured due to global buckling.

Geometrical imperfections were defined as a linear superposition of buckling eigenmodes. This approach involves two analysis runs with the same model definition:

- *Linear eigenvalue buckling analysis* on the panel with the nominal geometry to establish probable collapse modes and to verify that the mesh discretizes those modes accurately.
- *Postbuckling analysis* of the structure containing the geometrical imperfection. The perturbed mesh is created by scaling and adding the lowest buckling modes to the perfect geometry.

In structures with many closely spaced eigenmodes, buckling modes may interact after buckling occurs. Hence, imperfections based on a single buckling mode may yield nonconservative results and a combination of first modes must be used. On the contrary, if a weak interaction is expected due to a large mode separation, the lowest eigenmode may give the most

critical imperfection. This is the case of the investigated panel; thus, only the first global buckling mode (Figure 6.5a) was initially considered to define the geometrical imperfection.

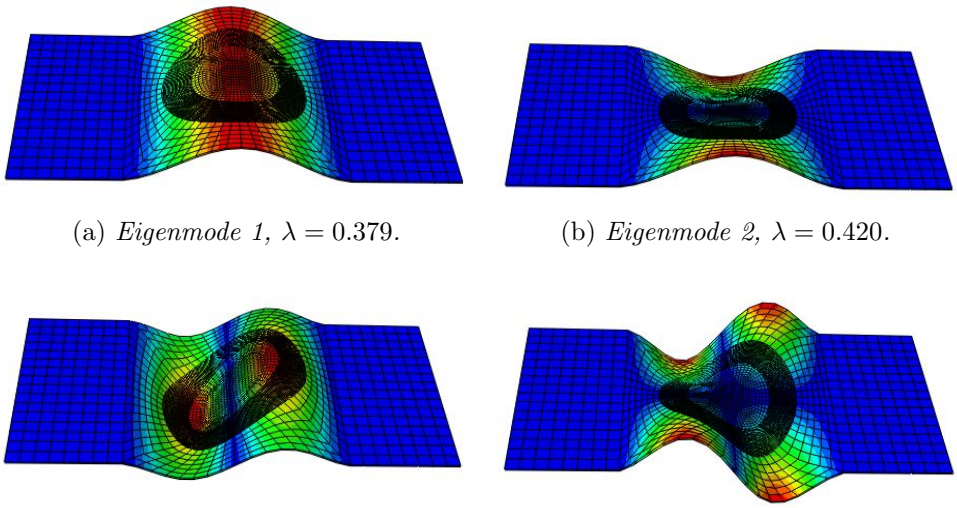

(a) *Eigenmode 1,* $\lambda = 0.379$. (b) *Eigenmode 2,* $\lambda = 0.420$.

(c) *Eigenmode 3,* $\lambda = 0.682$. (d) *Eigenmode 4,* $\lambda = 0.790$.

Figure 6.5: First buckling eigenmodes of the HTA/6376C plate.

The amplitude of the perturbation was controlled through the scale factor associated to each eigenmodes, which defines the maximum out-of-plane nodal displacement imposed to the initial configuration. Results for three different amplitudes, each one corresponding to aa different percentage of the plate thickness, are shown in Figure 6.6 and Table 6.6.

P_{LB} refers to the local buckling load, defined as the load at which initiation of the opening of delamination was observed. This opening can be measured as the difference between the transverse deflections of the two sublaminates. The global buckling load, P_{GB}, which coincides with the maximum compressive load, also referred as or failure load, P_{max}, denotes the load at which postbuckling stiffness is equal to zero, that is, at which transverse displacement increases at constant load. P_{growth} indicates the load at the onset of delamination propagation.

Predicted local buckling load is underestimated in all cases, but a larger imperfection tends to trigger the buckling of the delaminated member at lower displacement/load levels. Disregarding the size of the perturbation, delamination growth occurs just prior to global buckling, which arises at sliglthly higher loads than experimental values. Best agreement with reference data is achieved imposing an out-of-plane displacement corresponding to the 0.1% of the plate thickness, that is, 0.045mm.

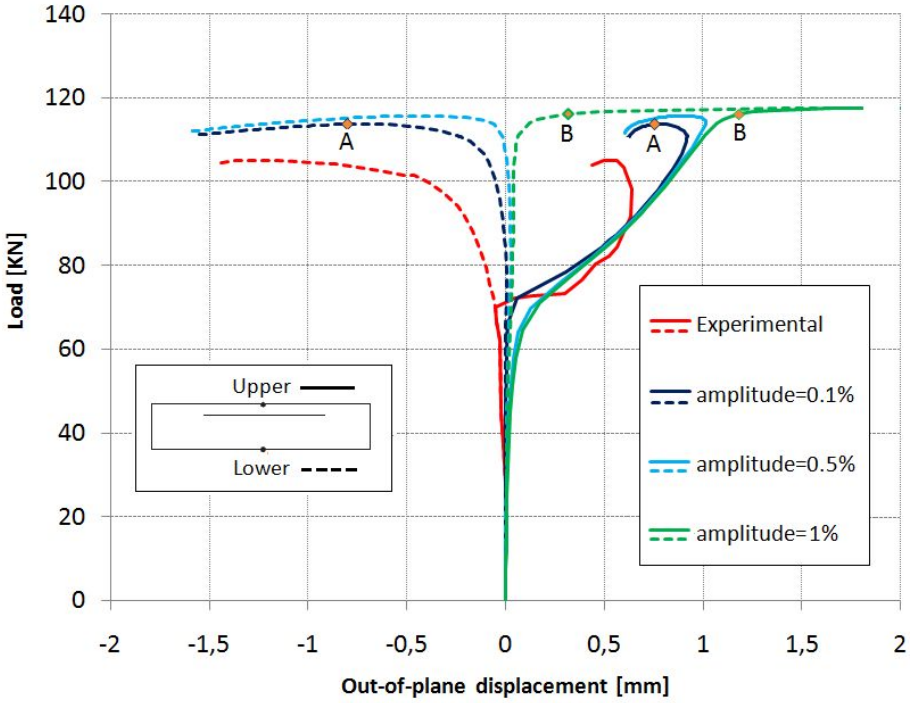

Figure 6.6: Sensitivitiy to imperfection amplitude (HTA/4376C model).

	P_{LB} (KN)	P_{growth} (KN)	$P_{GB} = P_{max}$ (KN)
Experimental [55]	72	104	105
amplitude = 0.1%	66.08 (-8.22%)	113.64 (9.27%)	113.80 (8.38%)
amplitude = 0.5%	58.01 (-19.43%)	115.45 (11.01%)	115.63 (10.12%)
amplitude = 1%	57.89 (-19.60%)	117.29 (12.78%)	117.50 (11.90%)

Table 6.6: Results in Figure 6.6.

It is interesting to notice how imperfections may affect the postbuckling behavior of the panel. The specimen deformation after the global buckling load is displayed in Figures 6.7a and 6.7b for amplitudes equal to 0.1% and 1% respectively (Points A and B in Figure 6.6).

These deformed shapes, which are shown with a deformation scale factor of 20, illustrate the variation of the collapse mode in a qualitative manner. In both cases, the delaminated member buckles and then initially deflects from the thicker lower sublaminate. For the panel with an imperfection amplitude of 0.1%, as the thinnest member reaches the maximum

out-of-plane displacement both sublaminates deflect downwards with an increasing opening of the delamination. For the panel with an imperfection amplitude of 1%, on the contrary, the thickest member deflects upwards as well, and delamination tends to close.

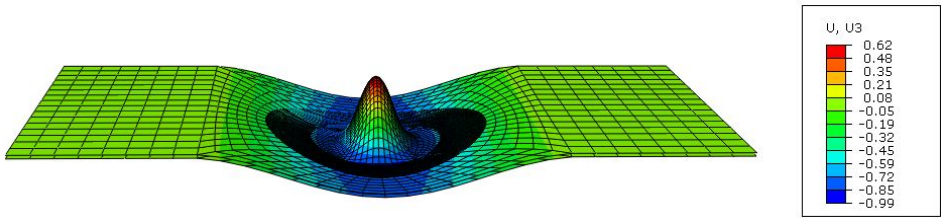

(a) *Collapse mode for amplitude=0.1%.*

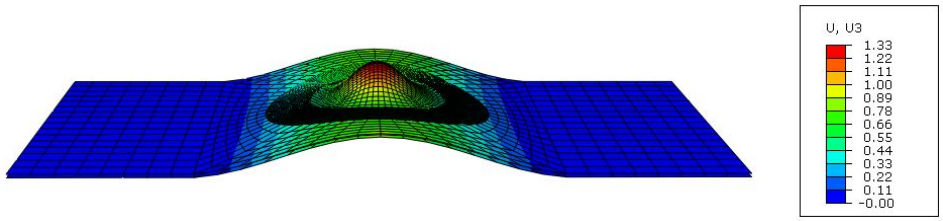

(b) *Collapse mode for amplitude=1%.*

Figure 6.7: Deformed shapes at collapse for two imperfection amplitudes.

With the intent to check that the imperfection defined previously was the most critical one, an additional analysis was carried out considering a combination of the first four global buckling eigenmodes (see Figure 6.7). Contribution of all modes was assumed to be the same, with an amplitude of 0.1% the total panel thickness. Results reported in Table 6.7 demonstrate that response is not significantly affected by a more complex definition of the imperfection and shows that first eigenmode triggers properly both local and global buckling.

	P_{LB} (KN)	$P_{GB} = P_{max}$ (KN)	P_{growth} (KN)
Experimental [55]	72	105	104
1 eigenmode	66.08 (-8.22%)	113.80 (8.38%)	113.64 (9.27%)
4 eigenmodes	65.41 (-9.15%)	113.65 (8.16%)	113.55 (9.18%)

Table 6.7: Results with an imperfection defined by the first four eigenmodes.

Sensitivity analysis to mesh density in the delaminated and undamaged regions

Validity of the mesh pattern determined from fracture simulations upon AS4/PEEK models was checked varying the fine-coarse parameter, fc, which defines the transitions of mesh density between the cohesive zone region and the adjacent parts of the model.

Element size where fracture propagation may occur, contrarily, was mantained equal to 1mm, which was the value that showed to capture correctly the complex stress fields that develop ahead of the delamination front in the AS4/PEEK specimens. Specific studies should be conducted for the HTA/6376C to ensure that a coarser mesh in that zone simulates properly delamination evolution: results of problems involving fracture phenomenon exhibit, in fact, a strong dependency upon mesh refinement level as shown in Chapter 4.

Differences among solutions obtained with different mesh densities outside the cohesive zone region may be motivated by the reduction of the model stiffness as the mesh is refined. Increasing the number of degrees of freedom, though, is only recommended when changes in the solution are not negligible. Further model refinement upon a certain level does not alter significantly results and only contributes to drammatically increase computational cost. To investigate this issue, a convergence check was performed using a finer model than that resulting from parameters in Table 6.5. Mesh pattern of the models are displayed in Figure 6.8, while results are reported in Table 6.8.

	P_{LB} (KN)	$P_{GB} = P_{max}$ (KN)	P_{growth} (KN)
Experimental [55]	72	105	104
$fc = 4$	66.08 (-8.22%)	113.80 (8.38%)	113.64 (9.27%)
$fc = 2$	65.61 (-8.89%)	112.971 (7.59%)	112.86 (8.52%)

Table 6.8: Results computed with different mesh densities outside the cohesive zone region.

A slightly lower global buckling load is obtained by the finer model due to a larger model compliance. Nevertheless, since differences are not significant, the coarser mesh was preferred.

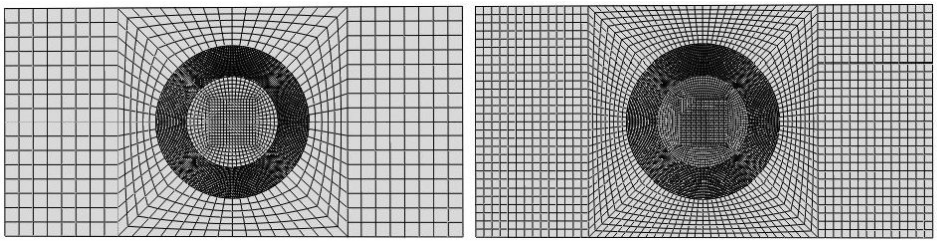

(a) $fc = 4$ (20480 elements). (b) $fc = 2$(27776 elements).

Figure 6.8: Mesh pattern of the HTA/6376C models for different fc values.

Sensitivity analysis to viscous regularization factor

Since damage arises after local buckling but prior to global buckling, interaction between damage mechanisms and postbuckling response may be significant. If the amount of viscous energy introduced to prevent convergence problems derived from the softening behavior of cohesive elements is not set properly, the plate response may be altered in the nonlinear range as damage extends (see Sections 4.2.2 and 4.3.2). To assess the convenience of using the value set for AS4/PEEK (in Table 6.5), two additional levels of viscosity were investigated. Results are shown in Table 6.9.

	P_{LB} (KN)	$P_{GB} = P_{max}$ (KN)	P_{growth} (KN)
Experimental [55]	72	105	104
$\mu = 10^{-6}$	66.08 (-8.22%)	113.36 (7.96%)	113.33 (8.97%)
$\mu = 10^{-4}$	66.08 (-8.22%)	113.80 (8.38%)	113.64 (9.27%)
$\mu = 10^{-2}$	66.08(-8.22%)	114.31 (8,89%)	114.31 (9.91%)

Table 6.9: Results computed with different regularization factors.

As expected, the viscous term has no influence upon the local buckling because there is no energy dissipation prior to damage initiation. As for global buckling and onset of the delamination growth, predictions are very similar for the three models. Nevertheless, delamination propagation may be sensitive to this parameter and, hence, structural response after maximum load may be affected. To select among the three investigated values, a precise correlation between increment of the delamination size and applied compressive load should be available; unfortunately this information is not provided in [55]. Thus, it was decided to mantain the dissipation value used with AS4/PEEK.

6.3 Results of the HTA/6376C model

Predictions computed by the FEM model implemented in accordance with conclusions of parameter studies performed in Section 6.2 are reported in Table 6.10.

	P_{LB} (KN)	$P_{GB} = P_{max}$ (KN)	P_{growth} (KN)
Experimental [55]	72	105	104
FEM model	66.08 (-8.22%)	113.80 (8.38%)	113.64 (9.27%)

Table 6.10: Comparison between FEM predictions and experimental results.

Local buckling load is slightly underestimated, probably due to the introduction of a geometrical imperfection to trigger loss of contact between upper and lower members and enable a correct delamination opening.

Global buckling load, on the contrary, is slightly overpredicted, even when a further mesh refinement was performed to check the convergence of the numerical solution. A possible reason for this may be the discepancy between boundary conditions imposed to the FEM model and the real ones. The perfect clamping provided by steel tabs introduced to the numerical model is, in fact, difficult to achieve experimentally. Indeed, Nilsson et al. [55] observed some flexibility of the clamped ends derived from the nonperfect clamping. This may explain the lower experimental value, as buckling loads are very strongly influenced by boundary conditions.

Similarly to experimental observations, onset of delamination growth occurs at a load slightly below the global buckling, which suggests that failure of the delaminated plate may be caused by fracture propagation.

Damage maps of the HTA/6376C plate were plot at three different analysis steps: damage initiation in Figure 6.9a, onset of delamination growth in Figure 6.9b and load drop of 1% after collapse in Figure 6.9c. An overall damage variable value (d in numerical procedures reported in Chapter 2 and $SDEG$ in Abaqus/Standard) of 0.00 denotes that the cohesive element does not undergo any damage, whereas a value of 1.00 indicates that the interlaminar interface is completely damaged and that, locally, upper and lower sublaminates are not connected together by cohesive forces anymore. Gray elements illustrate the increment of delaminated area.

In accordance with experimental C-scans performed in [55], delamination growth occurs in the perpendicular direction to the load and exhibits a symmetrical pattern.

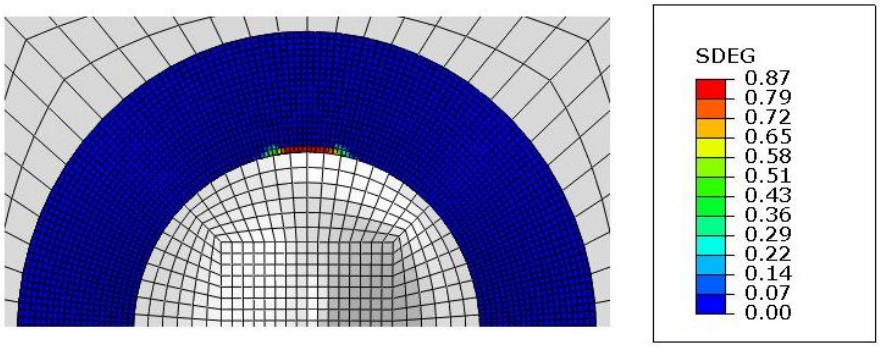

(a) *Damage initiation.* Compressive load = 78.31KN.

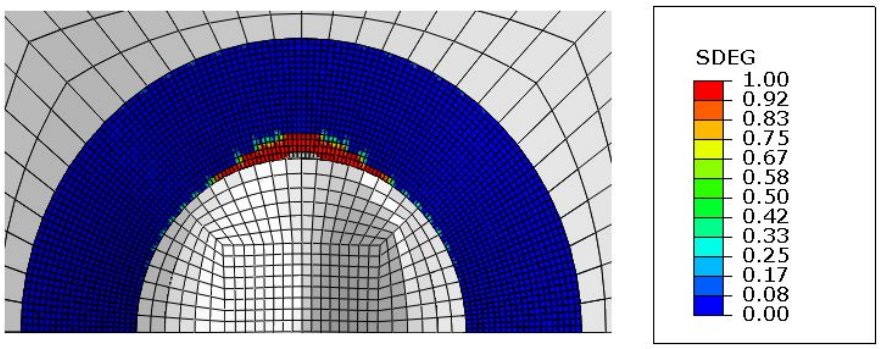

(b) *Onset of delamination growth.* Compressive load = 113.80KN

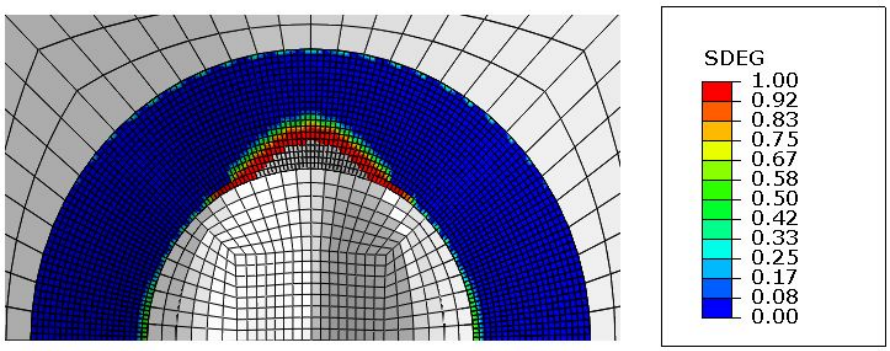

(c) *Delamination growth after global buckling.* Compressive load = 112.66KN

Figure 6.9: Damage maps at different load levels.

Points corresponding to these configurations are indicated in the central out-of-plane deflection and shortening versus uniaxial compressive load curves shown in Figures 6.11 and 6.12.

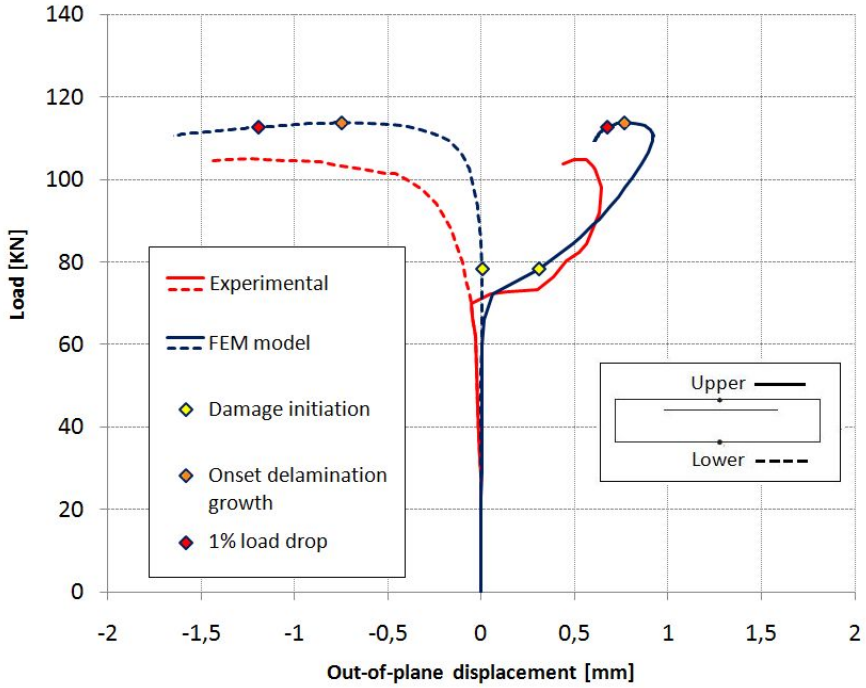

Figure 6.10: Load vs. central out-of-plane displacement of the HTA/6376C FEM model.

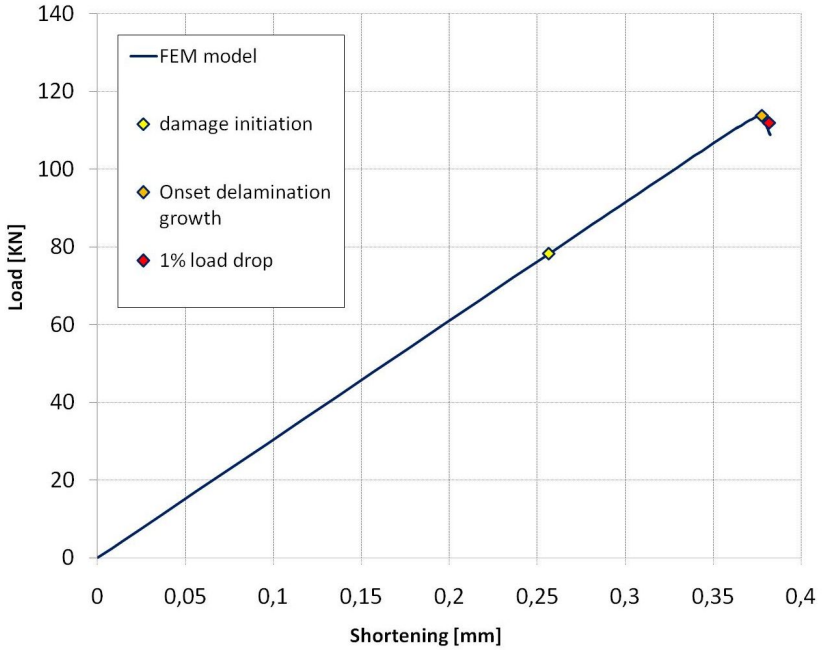

Figure 6.11: Load vs. shortening of the HTA/6376C FEM model.

Defomed shapes corresponding to these points are displayed in Figure 6.12 with a deformation scale factor of 20.

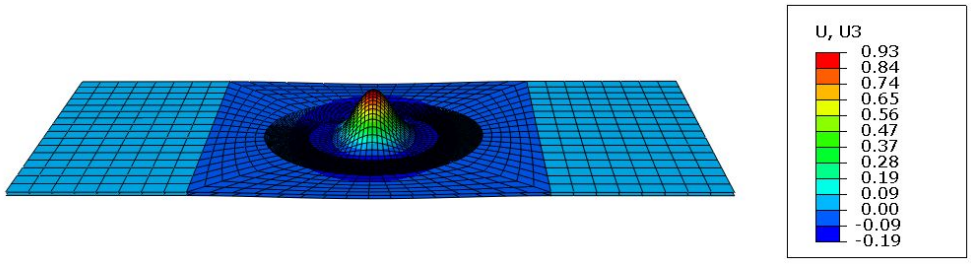

(a) *Damage initiation.* Compressive load = 78.31KN.

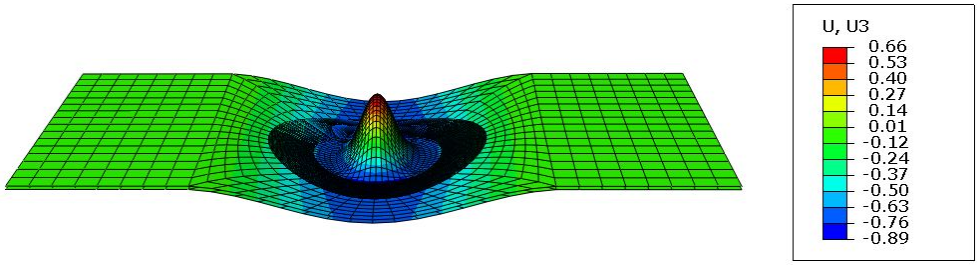

(b) *Onset of delamination growth.* Compressive load = 113.80KN

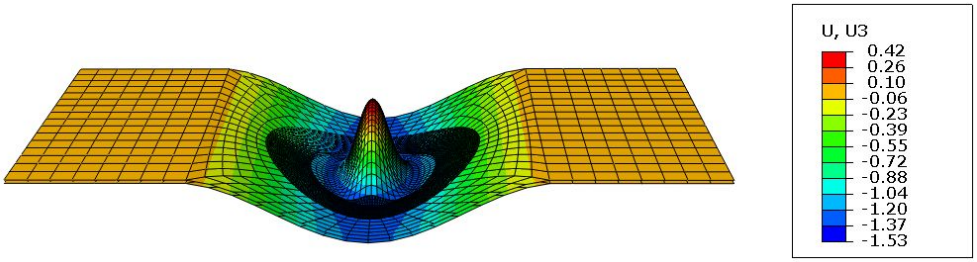

(c) *Delamination growth after global buckling.* Compressive load = 112.66KN

Figure 6.12: Deformed shapes at different load levels.

It can be noticed that for the size and through-the-thickness position of the initial Teflon insert within the investigated specimen, further loading upon local buckling load induces a mixed mode buckling mode, which is the mode evidenced at collapse load as well.

6.4 Concluding remarks

Delamination buckling in an HTA/6376C plate containing an artificial circular delamination was simulated in this Chapter.

Parametric studies aided in understanding the effect of various model parameters upon the predicted structural response in the postbuckling field and confirmed the validity of the parameter set inherited from fracture simulations on AS4/PEEK specimens conducted in Chapters 4 and 5. Therefore, usage of these values with damaged AS4/PEEK plates investigated in Chapter 7 is expected to provide reliable results as well.

Proper delamination opening to capture local buckling demanded the introduction of a geometrical imperfection to the nominal geometry of the specimen. Results showed a strong dependency upon the amplitude of initial out-of-plane displacements imposed to define the imperfection. Particularly, as amplitude increases local buckling is predicted to occur at lower loads and collapse mode may change with respect to experimental one. On the contrary, the number of buckling eingenmodes considered to construct the imperfection showed to be irrelevant. Indeed, as first buckling eigenmodes are not closely spaced, interaction among them is not significant after local buckling. Therefore, an imperfection based on the first eigenmode showed to trigger the proper collapse mechanisms.

A convergence check demonstrated that mesh pattern determined from simulations on AS4/PEEK was suitable and that further mesh refinement did not significantly improve the accuracy of results. Through this, it was concluded that mesh requirements in delamination buckling models are primarily established by the resolution required to correctly capture the delamination mechanisms under general loading conditions, which can be determined through the methodology implemented in Chapter 4.

For this reason, discrepancy with test data was not believed to be caused by the larger stiffness normally exhibited by FEM models with respect to real structures, but rather by the difference between boundary conditions used in the numerical model and the real clamping conditions achieved during experiments carried out in [55], in which, according to the authors, flexibility of the clamped ends probably reduced the global buckling load of the plate.

In conclusion, studies presented in this Chapter evidenced the importance of a careful set of imperfection size to determine reliable the compressive residual strength of a damaged panel. Separation between first buckling eigenmodes may provide guidance on selecting the combination of eigenmodes to construct the most critical imperfection. However, the collapse load may be overestimated if boundary conditions introduced to FEM models do not reproduce perfectly boundary conditions achieved in experimental tests.

Chapter 7

Compressive response for different delamination sizes, depths and shapes

This Chapter presents the results of a numerical investigation into the effect of delamination size, through-the-thickness position and shape upon the compressive response and residual compressive strength of a rectangular AS4/PEEK laminated panel.

Fracture analysis was based on parametric studies conducted in Chapters 4 and 5 to set various model parameters for finite-element simulations involving delamination propagation within unidirectional AS4/PEEK laminates, whose conclusions are discussed in Subsection 5.2. Simulation of buckling behavior, on the other hand, was assisted by experience gained through analyses of delamination buckling on HTA/6376C specimens presented in Chapter 6, in which experimental data was available.

Computed results are only intended for use to achieve qualitative conclusions regarding damage effects on residual compressive properties. Experimental compression tests are, in fact, absolutely necessary to enhance the setting of certain parameters, which otherwise is merely arbitrary and, thus, may yield to unrealistic ultimate strengths. Introducing the same arbitrarities into all the models, though, discrepancies among the responses of the different configurations investigated may be employed to illustrate the delamination effect in a qualitative manner. Experimental validation is left as future work.

7.1 Experimental procedure

Numerical models accounted for experimental conditions of compression tests to be carried out for results validation. A brief description of the test procedure is provided as follows.

Scheduled experimental test is based on the Standard Test Method for Compressive Residual Strength Properties of Damaged Polymer Matrix Composite Plates, issued under the designation D 7137/D 7137M by the ASTM [58].

This test method consists of a uniaxial compression test performed in a displacement control mode to a damaged continuous-fiber reinforced polymer matrix composite plate with multidirectional fiber orientations, which is both symmetric and balanced with respect to the test direction.

The damage state is imparted prior to the application of compressive force through out-of-plane loading caused by quasi-static indentation in accordance with Test Method D 6264/D 6264M [59]) or drop-weight impact in accordance with Test Method D 6264/D 6264M [60]), in which case the test method is commonly referred to as Compression After Impact, or CAI, method.

The damaged flat rectangular plate, whose geometry and staking sequence are described in Subsection 7.2.1, is installed in a multi-piece support stabilizing fixture developed by the Boeing Company, described in Subsection 7.2.2, which inhibits global buckling when the specimen is end-loaded and that has been aligned to minimize axial loading eccentricities that may induce specimen bending. In any case, longitudinal strain measurement at four locations, with two gages attached on opposite faces of the coupon, is recommended to ensure application of pure compressive loading and to detect bending of buckling, or both, if any.

Applied force versus crosshead displacement (stroke) and versus strain (recommended although not required) are recorded while loading until a force maximum value is reached and force has dropped off about 30% from it to prevent support fixture damage, unless the specimen is to be failed, in which case the stroke is increased until specimen rupture.

The purpose of this test procedure is to assess- the damage tolerance capability of the tested laminate, namely, to compute the ultimate compressive residual strength and compressive stiffness of the tested specimen. The response of a damaged coupon, though, is dependent upon many factors, such as laminate thickness, ply thickness, stacking sequence, environment, damage type, damage geometry, damage location and loading/support conditions. Consequently, the results are specific to the geometry and physical conditions tested and are not generally scalable to other configurations.

The difference between the scheduled test and the Test Method D 7137/D 7137M lies in the fact that damage is not originated by any previous test, but artificially introduced by inserting a circular Kapton film at a specified location within the AS4/PEEK panel. Specimen rupture is

not desired as it may damage the support fixture, which should be, consequently, replaced after each test. C-scan will be carried out at different crosshead displacement levels to provide damage maps to which compare progressive debonding predicted by numerical models (see Appendix A).

7.2 Description of the FEM models

Geometry, boundary conditions and mesh pattern of the investigated specimens are discussed in this Section.

7.2.1 Geometry of the damaged specimens

According to the Test Method D 7137/D 7137M, nominal length and width of the plate specimen are 150 and 100mm respectively, whereas thickness shall be 4.0 to 6.0mm, with a target value of 5.0mm. However, small variations in geometry can be accommodated as well within the adjustable test fixture (see Subsection 7.2.2). A sketch of the specimens containing a circular delamination is shown in Figure 7.1.

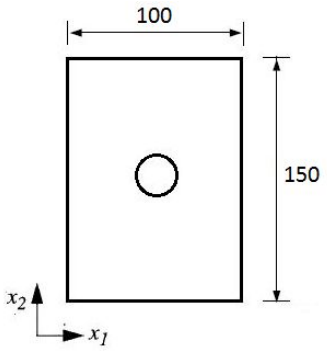

Figure 7.1: Sketch of the AS4/PEEK panel with a circular delamination.

Laminate construction shall consist of the appropriate number of UD plies to achieve a total cured thickness nearest to 5.0mm with a stacking sequence of $[45/0/-45/90]_{\mathrm{NS}}$ (symmetric and balanced), where N is a whole number. The laminated plate layup is defined such that the 0^{o} fiber orientation is aligned with the loading direction. Recommended layups for various nominal cured ply thicknesses are reported in [58]. Particularly, for a nominal cured ply thickness of 0.21mm, recommended N is 3. Thus, the laminate consists of 24 plies, which yields to a total thickness t of 5.04mm.

Delamination-related dimensions, which vary among the different configurations analyzed, are depicted in Figure 7.2, which also evidences the

ratio h/t, employed to define the through-the-thickness position of the Kapton insert. Characteristic initial delamination size a_0 denotes the diameter for the circular damage and the side length for the square damage.

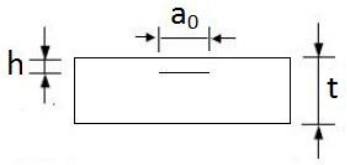

Figure 7.2: Delamination-related dimensions of the AS4/PEEK panels.

Delamination sizes

The Test Method D 7137/D 7137M recommends that the damage size be limited to half the unsupported specimen width to minimize interaction between damage and edge-related stress/strain fields. Indeed, as the specimen has a small length-to-width aspect ratio of 1.5, edge effects, boundary constraints and the damaged stress/strain field can interact if the damage size becomes to large relative to the plate dimensions. Thus, $a_{0\text{MAX}} = 42mm$.

Accounting for the upper bound defined by the standard test method, characteristic delamination dimension a_0 was computed from a set of prespecified A_d/A ratios, where A_d is the initial damaged area and A is the unsupported area of the panel, evidenced in Figure 7.4. Examined delamination sizes are summarized in Table 7.1:

A_d/A	a_0 (mm)	
	Circular	Square
0.02	17.72	15.70
0.04	25.06	22.21
0.06	30.69	27.20
0.08	35.44	31.40
0.10	39.62	35.11

Table 7.1: Investigated delamination sizes.

Delamination depths

Through-the-thickness location of the Kapton inserts are presented in Table 7.2, which reports the damage depth in terms of the distance h with

respect to the upper surface of the plate as well as the corresponding h/t ratio and position within the layup.

h/t	h (mm)	z-location plies
0.125	0.63	3/4
0.25	1.26	6/7
0.375	1.89	9/10
0.5	2.52	12/13

Table 7.2: Investigated delamination depths.

7.2.2 Boundary conditions

Boundary conditions were introduced into the model considering the constraints provided by the anti-buckling support fixture used in the Test Method D 7137/D 7137M. Detailed drawings for its manufacturing are provided in [58].

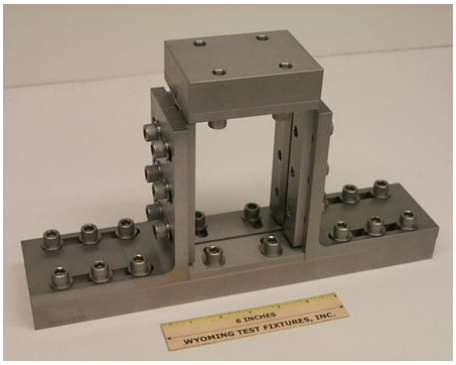

Figure 7.3: Assembled test fixture, without specimen.

The compressive test fixture, shown in Figure 7.3 [61], utilizes adjustable retention plates to accommodate small variations in specimen length (from 146 to 150mm), width (from 98 to 116mm), and thickness (up to 20mm). It consists of one base plate, two base slideplates, two angles, four side plates, one top plate and two top slideplates. The assembled fixture, with a specimen installed, is positioned unconstrained on the flat base of the testing machine, the compressive displacement rate being applied directly to the top plate by a platen until failure.

The side supports are knife edges, which provide no restraint to local out-of-plane rotation. The side rails are short enough to ensure that a gap

between them and the top plate, which is not directly attached to the lower portion of the fixture, is mantained during the test. The top and bottom supports provide no clamp-up. However, since the base and top slideplates have a squared geometry and overlap the specimen by 8mm, they provide some out-of-plane rotational restraint.

Boundary conditions and prescribed displacement applied to the models are shown in Figure 7.4, in which the initial 4mm gap between the side rails and the top plate can be noticed as well.

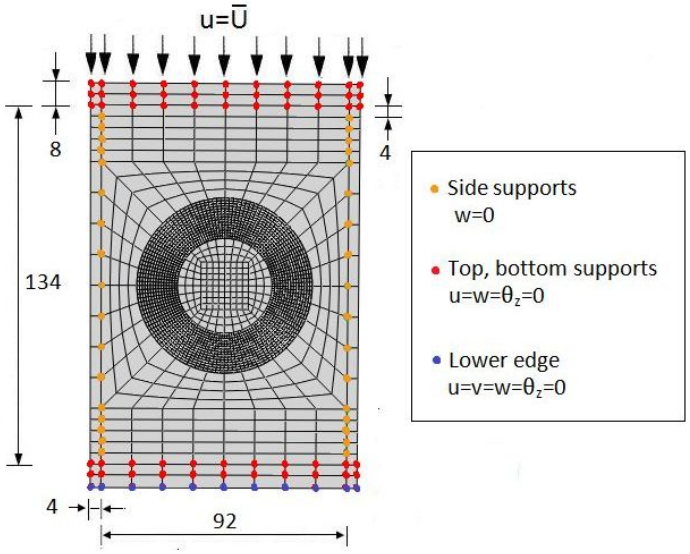

Figure 7.4: Boundary conditions and prescribed displacements in the AS4/PEEK models.

These boundary conditions are realistic enough unless there exist gaps between the slide plates and the specimen, which can reduce the effective edge support and can result in concentrated load introduction conditions at the top and bottom specimen surfaces, and as long as torque aplied to the slide plate fasteners ensures an effective edge support. Nonperfect out-of-plane rotational restraint provided by the base and top slideplates may be modeled or not: obtained results, in fact, do not significantly differ among them.

The inner 92x134mm rectangle confined by the slideplates constitutes the unsupported area of the panels, A, which is used to normalize the delaminated area A_d.

7.2.3 Mesh pattern

The damaged AS4/PEEK panels were modeled with two layers of reduced-integrated S4R shell elements. Thickness of each of the sublaminates varies according to the damage depth. Similarly to HTA/6376C specimen, the model was divided into three parts connected together by tie constraints to allow for rapid transitions in mesh density across their interfaces:

- *Delaminated region*, corresponding to the area of the circular or square Kapton film, in which contact was implemented to prevent mutual interpenetration between the upper and lower sublaminates.
- *Cohesive zone region*, where a layer of cohesive elements was located to simulate damage propagation and material softening.
- *Undamaged region*, in which the upper and lower layers of shell elements were tied together by means of beam type multi-point constraints to reproduce a perfect bond throughout the simulation.

Mesh pattern of the panels are reported in Figures 7.5 and 7.6, which evidence the circular and square delamination areas for the different initial damage sizes.

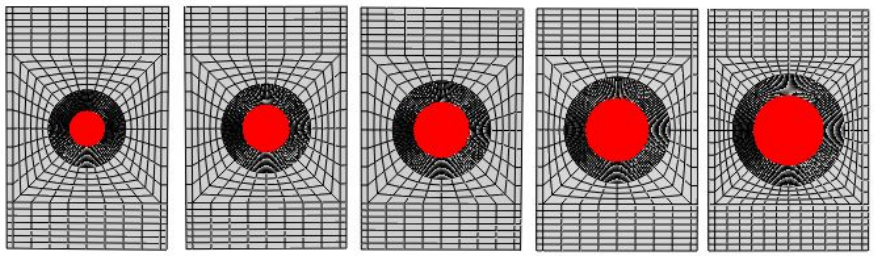

Figure 7.5: Mesh pattern, $A_d/A = 0.02, 0.04, 0.06, 0.08, 0.10$ (circular).

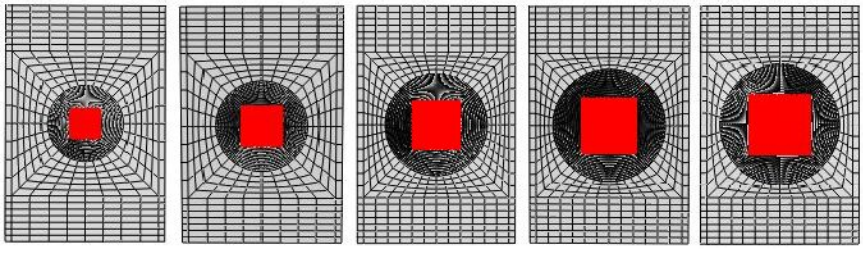

Figure 7.6: Mesh pattern, $A_d/A = 0.02, 0.04, 0.06, 0.08, 0.10$ (square).

7.2.4 Set of model parameters

The set of parameters employed to simulate the fracture and buckling mechanisms involved in the compressive response of the AS4/PEEK panels with artificial damage are reported in Table 7.3.

Mesh parameters	
Imperfections	amplitude: 3% buckling eigenmodes: 1-2
Fine-coarse ratio, fc	4
Element size in the cohesive zone, $size$ (mm)	1.0
Cohesive zone model parameters	
Penalty stiffness, K_p (N/mm^3)	10^6
Viscous regularization factor, μ	10^{-4}

Table 7.3: Set of model parameters to simulate the compressive response of AS4/PEEK panels.

It can be pointed out that the only difference with respect to values used in the simulation of delamination buckling of a damaged HTA/6376C plate performed in Chapter 6 lays in the imperfection definition. In fact, while experimental data for the HTA/6376C specimens was available in literature and, consequently, the perturbation amplitude could be accurately set to achieve a good agreement with test results, reference data for the AS4/PEEK panels is still to be generated in compression tests left as future work and, thus, the amplitude had to be set arbitrarily. Because of the dominant role played by imperfection size in numerical solutions computed by FEM models, shown in parametric studies presented in Subsection 6.2, results obtained without experimental validation of the imperfection amplitude may be highly inaccurate and, consequently, not reliable from a quantitative point of view. Nevertheless, buckling analyses carried out in this Chapter could be used to reach qualitative conclusions on the effect of geometry and through-the-thickness position of delamination by introducing the same arbitrary imperfection amplitude into all models and examining the qualitative differences among the compression response of the various analyzed configurations. As shown in Table 7.3, this arbitrary maximum out-of-plane displacement was set to a commonly used 3% of the panel thickness.

The geometric imperfection was constructed with the first two buckling eigenmodes of the panel, displayed in Figure 7.7, as they yielded the most

conservative results. Corresponding eigenvalues are not reported because they change slightly from one model to another. Additional eigenmodes were not included, being their influence on results negligible.

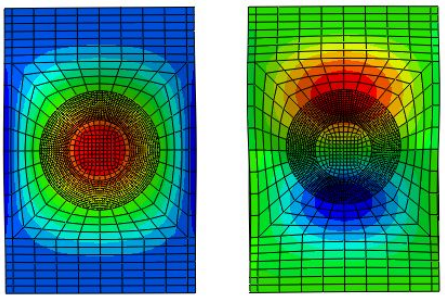

Figure 7.7: Global buckling modes used to construct the imperfection.

7.3 Buckling analyses of AS4/PEEK panels with delamination

In this Section, results obtained by FEM models with different delamination sizes, depths and shapes are discussed in a qualitative manner. To mantain the gap between side rails and the top plate during the whole analysis, simulation was terminated at a maximum axial displacement of 3.5mm whenever failure was not observed.

7.3.1 Effect of area and depth of a circular delamination

Computed results for all combinations of sizes and through-the-thickness locations of the circular artificial damage are reported in Table 7.4. P_{LB} denotes the local buckling load, namely, the load at which delamination opening initiates. Commencement of the sublaminates separation was evidenced by means of the load versus central transverse deflection curves. P_{growth} refers to the load at which delamination growth occurs and was determined through damage maps obtained by plotting the value of the overall damage variable ($SDEG$ in Abaqus/Standard) during the simulation. Finally, P_{max} indicates the residual compressive strength, which was computed as the maximum load of the load-shortening curve. Due to the symmetry of the laminate, results for $h/t = 0.625$, $h/t = 0.75$ and $h/t = 0.875$ can be take to be the same as those obtained in $h/t = 0.125$, $h/t = 0.25$ and $h/t = 0.375$ respectively.

It can be noticed that local buckling may manifest itself only when the upper sublaminate is much thinner than the lower one; otherwise, both arms buckle out together without any delamination opening. Particularly, differential transverse deflection of sublaminates was only observed for the most superficial damage condition, i.e., $h/t = 0.125$ (and $h/t = 0.875$), disregarding the delamination area. However, as damage size increases, estimated local buckling load decreases, as shown in Figure 7.8.

A_d/A	h/t	P_{LB} (KN)	P_{growth} (KN)	P_{max} (KN)
0.02	0.125	67.81	-	-
	0.25	-	-	-
	0.375	-	332.68	332.75
	0.50	-	279.36	281.06
0.04	0.125	32.26	-	-
	0.25	-	-	-
	0.375	-	290.38	290.633
	0.50	-	258.95	259.98
0.06	0.125	25.8	-	-
	0.25	-	303.07	303.31
	0.375	-	266.87	266.91
	0.50	-	241.22	243.10
0.08	0.125	12.90	-	-
	0.25	-	277.76	277.93
	0.375	-	251.43	251.45
	0.50	-	227.30	227.99
0.10	0.125	6.45	-	-
	0.25	-	259.41	259.74
	0.375	-	238.39	238.40
	0.50	-	214.55	215.38

Table 7.4: Results for different circular delamination sizes and depths.

Failure, contrarily, was predicted to occur at all through-the-thickness locations (yet not for all sizes within each depth level) except for $h/t = 0.125$. Computed maximum loads of configurations, for which collapse was predicted, are diplayed in Figure 7.9. As onset of debonding propagation arises at a load slightly below or equal to the ultimate strength, failure is assumed to be promoted by delamination growth. Indeed, only configurations in which fracture propagation takes place lead to collapse.

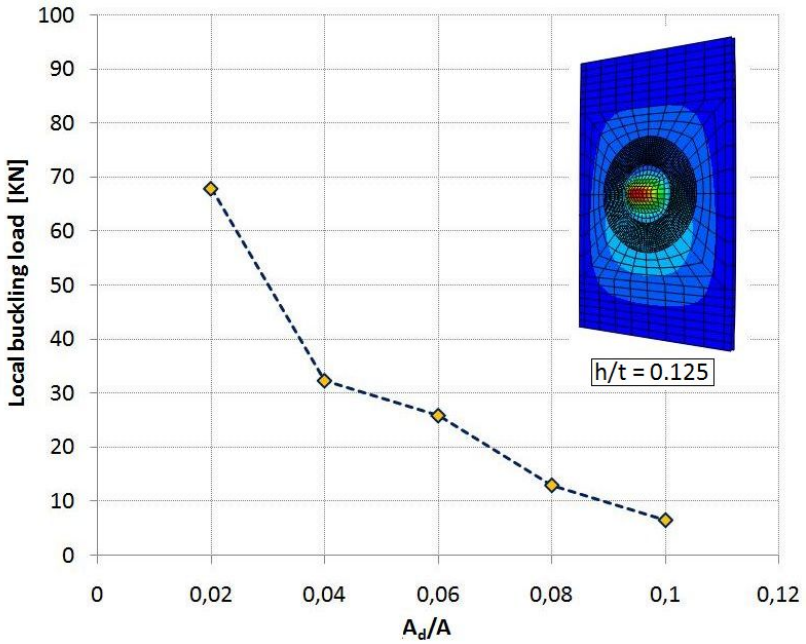

Figure 7.8: Local buckling load vs. circular delamination area.

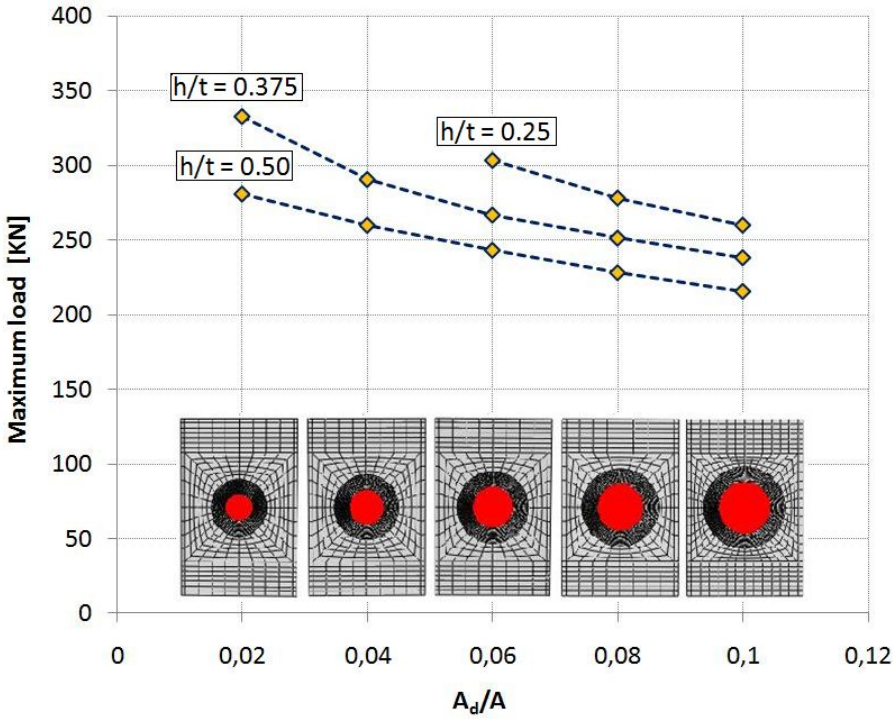

Figure 7.9: Maximum load vs. circular delamination area and depth.

Figure 7.9 evidences that loss of compressive strength induced by a circular Kapton inserts is greater when thicknesses of the two sublaminates into which the panel is divided are similar. Particularly, for a given initial damaged area, ultimate strength is minimum when the initial debonding is located at the midsurface of the panel.

For a given depth position, in turn, loss of maximum load increases with delamination size. Load versus axial displacement curves corresponding to different delamination sizes for $h/t = 0.50$ are plotted against the undamaged response in Figure 7.10.

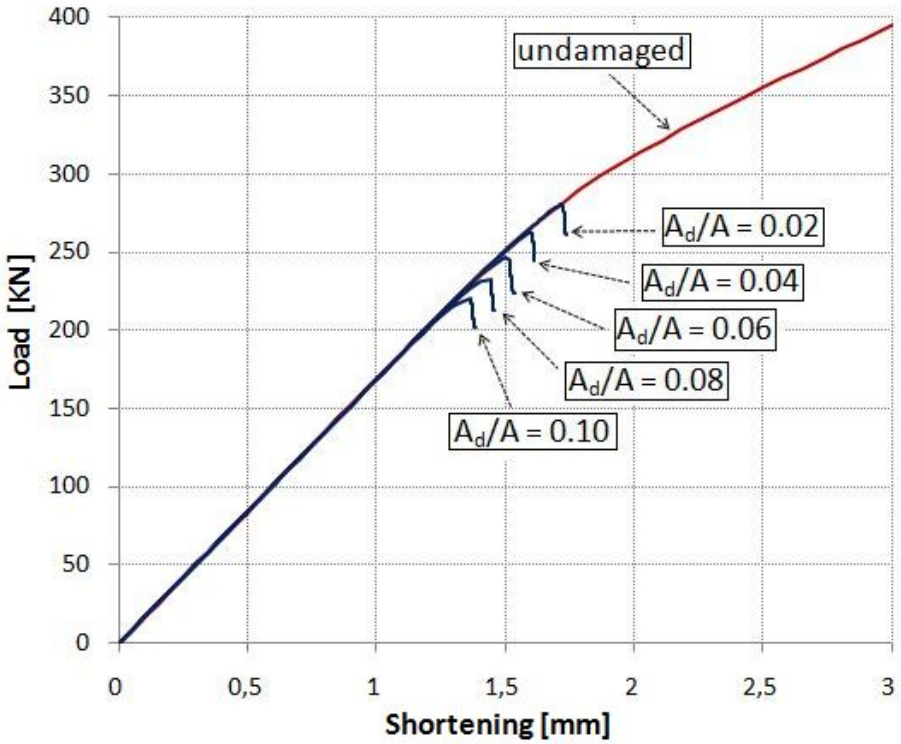

Figure 7.10: Load vs. shortening for different sizes of a circular delamination at midsurface.

7.3.2 Effect of delamination shape

The effect of delamination shape was investigated by computing the residual compressive strength of panels with a circular or square insert at their midsurface. Obtained results for different initial debonding sizes are shown in Figure 7.11 and in Table 7.5.

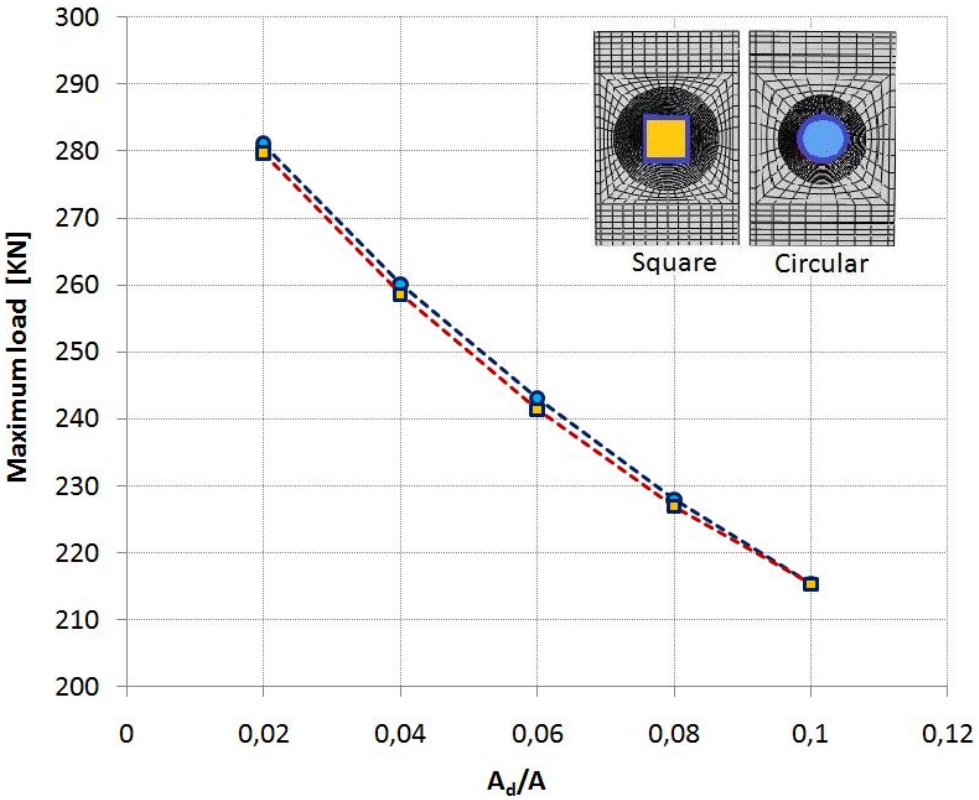

Figure 7.11: Maximum load vs. size of circle and square delaminations at midsurface.

h/t	A_d/A	$P_{\max}$ (KN)	
		Circular	Square
0.50	0.02	281.06	279.73
	0.04	259.98	258.59
	0.06	243.10	241.38
	0.08	227.99	226.90
	0.10	215.38	215.34

Table 7.5: Maximum load vs. size of circle and square delaminations at midsurface.

Maximum loads are slightly higher for circular delaminations. Negligible differences, however, indicate that degradation of the compressive strength does not significantly depend on the insert shape (circular or square), but rather on the initial debonded area.

7.4 Concluding remarks

A numerical research on the effect of delamination upon the compressive response and failure of a rectangular AS4/PEEK laminated panel was conducted in this Chapter. Attention was focused on the influence of size, through-the-thickness location and shape of the Kapton film inserted to simulate an impact-induced delamination.

Cohesive model parameters and mesh desity pattern establihed in Chapter 4 to reach a good compromise between accuracy and computational cost in simulations of delamination propagation within unidirectional AS4/PEEK laminates under general loading conditions (see Chapter 5), and succesfully used to model the delaminatin buckling of a damaged HTA/6376 plate in Chapter 6, were employed to reproduce damage evolution within the different investigated configurations.

The introduction of geometrical imperfections was necessary to trigger the finite out-of-plane deflections involved in the buckling response. Sensitivity studies in Chapter 6 demonstrated the large influence of imperfection amplitude on the computed solution and evidenced that the scale factor associated to each eigemode must be carefully selected to obtain realistic results. Since compression tests are left as future work, experimetal data was not available to carry out an accurate setting of the imperfection amplitude, which, as a consequence, could only be set arbitrarily basing on commonly used values (3%). Therefore, reliability of obtained results cannot be guaranteed from quantitative point of view until tests are performed. This is illustrated in Figure 7.12, in which different imperfection amplitudes are used to simulate the compressive response of a panel containing a 30.69mm diameter delamination ($A_d/A = 0.06$) at $h/t = 0.375$. It can be noticed that, for this damage condition, a greater amplitude yields a much lower ultimate strength, whereas, a smaller amplitude does not even predict the panel failure.

Nevertheless, since the same geometric perturbation was applied into all models, results could be analyzed in a qualitative manner. The following conclusions, consistent with similar previous works regarding the effects of a single delamination on compressive failure [62], were reached:

- Results indicate that loss of compressive strength increases when thicknesses of the two sublaminates into which the panel is divided are similar, being the midsurface delamination the most critical case. Indeed, drop of load-carrying capacity was not predicted for specimens with the most superficial delamination, which, on the contrary, were the only configuration in which local buckling took place.

- Delamination size plays a dominant role as well, with a significant reduction of the maximum load as initial debonded area increases.

Besides, further conclusions were achieved:

- For models which collapsed within the maximum crosshead displacement simulated, failure was determined to occur just after onset of delamination growth.
- Studies on the influence of two delamination shapes (circular and square) located at midsurface showed negligible differences for a given size, which suggests that residual compressive strength depends on the delamination area rather than its circular or square shape.

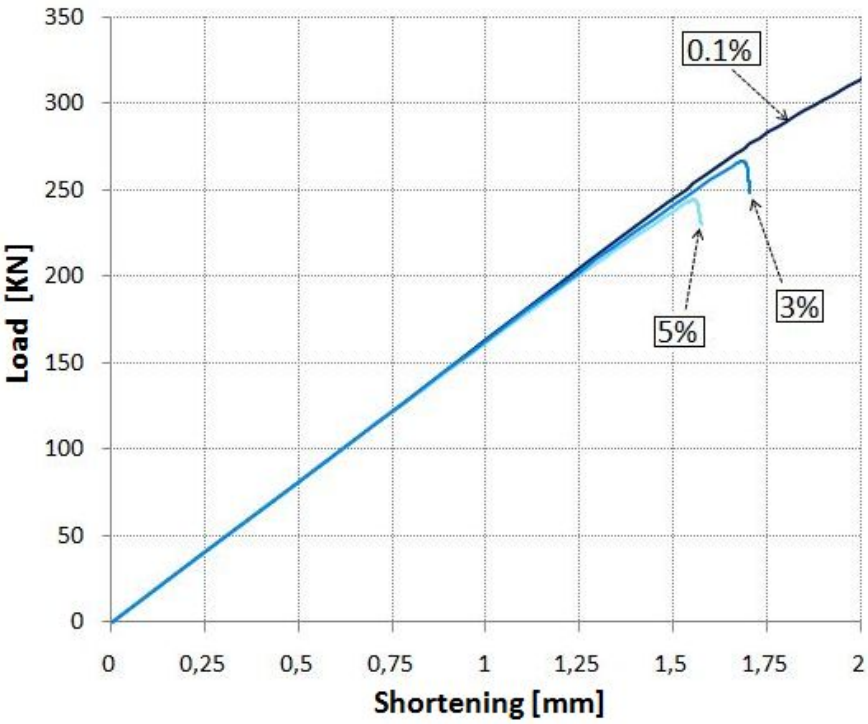

Figure 7.12: Sensitivity to imperfection amplitude (circular, $A_d/A = 0.06$, $h/t = 0.375$) .

Chapter 8

Conclusions and future work

Buckling response of composite laminated panels with an artificial delamination was numerically investigated.

Simulation of fracture propagation mechanisms demanded a careful setting of several model parameters related to the formulation of cohesive elements and the definition of a suitable discretization pattern. The proposed methodology to determine a set that provided a good compromise between accuracy and computational cost in finite-element analyses involving general mixed-mode loading conditions was based on comparison between results of sensitivity studies of simple DCB and ENF models to experimental data found in literature. A series of subsequent crossed analyses showed that, for the AS4/PEEK, requirements imposed by the ENF model were not critical and thus, the set of parameters could be simply derived from parametric studies on the DCB model. Reduced-integration S4R elements showed to aid in significantly reducing the CPU times without altering the accuracy of results. The MMB test was then simulated to check the mixed-mode case. Load-displacement response under both single-mode and mixed-mode loading conditions was reproduced well even during fracture propagation and maximum loads were predicted within an accuracy of $\pm 9\%$ with respect to the real test values extracted from literature, thus confirming the reliability of results obtained with the determined set. The most significant discrepance between numerical and experimental data was obtained for a mode ratio equal to 0.20, for which the largest difference between the fracture toughness experimentally measured and predictions computed by the B-K criterion was observed. The slight underestimation of the initial stiffness in the MMB simulations was not believed to be related to the selected parameter values: previous sensitivity studies evidenced, in fact, their negligible influence on the structural response prior to delamination growth.

The obtained set was expected to yield realistic results also for the HTA/6376C because of its comparable fracture-related properties. Therefore, it was employed in a delamination buckling analysis of an HTA/6376C

plate containing a circular non adhesive insert. Influence of model parameters involved in the nonlinear static approach adopted to solve the buckling problem was investigated, evidencing that the dominant role played by geometric imperfections introduced into the model was due to the great sensitivity to the amplitude rather than to the much smaller effect of the number of buckling eigenmodes considered. A convergence check validated the spatially-variable dicretization pattern determined in the previous fracture analyses. It was concluded, hence, that mesh requirements in delamination buckling models are primarily established by the refinement level required to correctly capture the delamination mechanisms under general loading conditions. The set of cohesive-model-related parameters together with a proper imperfection definition showed to yield estimations of the onset of delamination growth responsible for the failure of the plate in good agreement with experimental results found in literature, with an error of less than 10%. Discrepancy with experimental data was thought to be caused mainly by differences between the perfect boundary conditions applied into the numerical model and the non perfect clamping conditions of real specimen. According to the authors of the test, the flexibility of the clamped ends observed during compression of the plate might have promoted a reduction of the collapse load.

A study was finally undertaken about the effect of embedded delaminations of different sizes, shapes and through-the-thickness locations on the compressive strength of an AS4/PEEK panel. Because of the lack of experimental results to which compare numerical results, the imperfection amplitude could not be carefully set and, hence, only qualitative considerations could be achieved. This was done by introducing the same arbitary imperfection amplitude into all models. Conclusions were consistent with similar previous works conducted by other authors, showing a reduction of the residual compressive strength with delamination size and depth (until midsurface) and evidencing the failure due to fracture propagation. Models with circular and square delamination shapes, on the contrary, yielded almost identical results, given a certain delamination size. Local buckling, on the other hand, was only predicted for the most superficial damage locations and its initation load decreased with delamination area.

To consent a precise setting of the models, reference data needs to be generated to eliminate the arbitrarity of the imperfection amplitude. At this aim, experimental compression tests should be carried out on the same AS4/PEEK panels for a quantitative assessment of the influence of the different delaminations investigated. In doing so, accuracy of the numerical models could be evaluated and enhanced through further parametric studies and comparison against experimental results, not only in

terms of load-shortening curves and residual compressive strengths, but also in terms of post-buckling shapes and, particularly, fracture evolution. Indeed, progressive debonding predicted using the set of cohesive-model-related parameters determined in this work could be compared to the delamination growth measured, for instance, by means of an ultrasonic system at different load steps during the test. To explore the potential of this NDT Non Destructive Technique, the pulse-echo technique with a single contact transmitting/receiving transducer was employed on a CFRP plate with impact-induced damage and an HTA/RTM6 NFC plate with artificial delaminations (see Appendix A). Different signal processing techniques were used to obtain C-scan and B-scan representations from the acquired waveforms, which enabled not only to detect the presence of a damaged area but also to distinguish its geometry and depth within the CFRP specimen. On the other hand, large superficial roughness of the HTA/RTM6 NFC plates, caused by poor manufacturing practices, prevented to obtain accurate damage representations. Ultrasonic testing showed, therefore, to be a very useful tool to detect embedded damage within composite specimens, provided that their manufacturing process was correct.

Appendix A

Ultrasonic testing

Ultrasonic testing is a type of NDT (Non Destructive Testing) commonly used to detect typical flaws within aerospace composite structures, such as cracks and interlaminar debonding. Therefore, this technique may be employed to evaluate the progressive delamination growth throughout the experimental compression tests on AS4/PEEK specimens with different delamination sizes, depths and shapes to be carried out to aid in setting the FEM models implemented in Chapter 7. Once the imperfection amplitude was precisely set, C-scan and B-scan images, namely, an in-plane bidimensional damage representation and a depth damage visualization on a selected cross section, may be compared to damage maps obtained by numerical analyses at different load steps to assess the reliability of predictions obtained with the set of parameters obtained from the DCB and ENF simulations.

The US (ultrasonic) method adopted to measure the debonding propagation during compression tests will be the pulse-echo technique with a single contact probe that will work as a transmitting/receiving transducer. This method is based on partial reflections (echoes) of the US beam generated when the signal encounters a discontinuity surface where material acoustic impedance changes, such as a flaw or the opposite specimen surface (back echo reflection). Identification of additional peaks prior to the back echo as well as attenuation of the back echo peak may indicate the presence of an internal flaw.

To gain understading of this technique, a damaged composite specimens was inspected. Results are reported in Section A.3.

A.1 Ultrasonic testing system

The ultrasonic probe is a Krautkramer contact alpha series transducer DFR-P 16390, a high frequency US probe (22 MHz) suitable for applications such as thin thickness measurements and near-surface flaw detection.

The contact diameter is equal to 7.6 mm and the measuring range is between 0.13 and 3.8 mm.

To generate and receive US pulses, a Panametrics-NDT pulser/receiver 5800 PR characterized by 35 MHz (-3 dB) ultrasonic bandwidth is used. To acquire US waveforms a LECROY Wave Surfer 422 digital oscilloscope is used. Finally, the stored waveforms are analyzed through a software developed in Matlab to obtain C-scan and B-scan representations of the specimens.

A sketch of the ultrasonig testing system is shown in Figure A.1 [63].

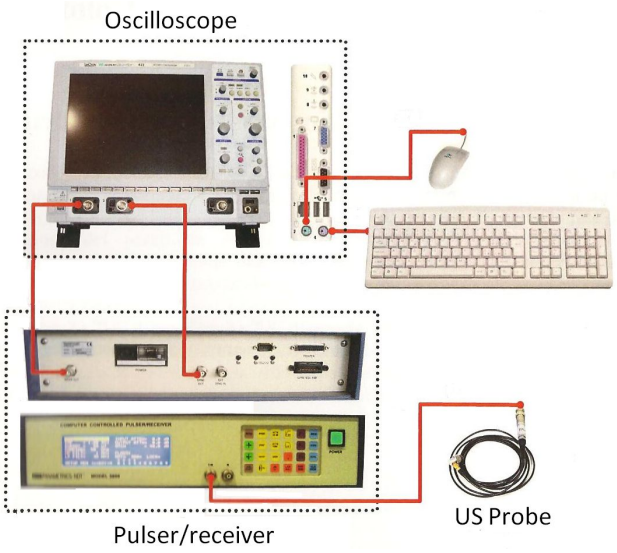

Figure A.1: Sketch of the ultrasonic testing system.

A.2 Signal processing techniques

Signal processing techniques employed to process acquired waveforms are presented in this Section.

TOF (Time-of-Flight)

C-scan representations may be generated using the TOF (Time-of-Flight) method, which measures the time that it takes for the emitted US beam to travel back to the probe after being reflected by the flaw, in a damaged area, or by the specimen back surface, in an undamaged region. At this purpose, sample time points of acquired signals must be correlated to the spatial distance traveled by the US pulse, accounting for the fact that

time-of-flight of the back echo reflection corresponds to two times the distance to the discontinuity surface.

Let n_{BE} be the position of the back echo peak within the vector containing the sample points of the acquired signal in a generic location of the scanning grid. The distance of the discontinuity surface from the US probe, s_{US}, is derived from the following expression:

$$s_{\mathrm{US}} = \frac{V_{\mathrm{US}}}{2}\frac{(n_{\mathrm{BE}} - 1)}{SR} \tag{A.1}$$

where, V_{US} is the propagation speed of ultrasonic waves within the material (for carbon fiber, $V_{\mathrm{US}} = 3000m/s$) and SR is the sampling rate, equal to 10 MS/s (MegaSample/s).

C-scan representations obtained through this technique provide information about through-the-thickness location of damage as well. However, its usage is limited to cases in which back echo peak is clearly identifiable.

MAC (Modal Assurance Criterion)

The MAC (Modal Assurance Criterion) was used to obtain C-scan representations of the damaged specimen. This technique, usually employed as a modal identification method in modal testing, was used to evidence damaged areas within damaged composite specimens in [63].

The function of the MAC is to provide a measure of consistency (degree of linearity) between two vectors ψ_a and ψ_x:

$$MAC(A, X) = \frac{\left\|\{\psi_x\}^T\{\psi_a\}\right\|^2}{\left(\{\psi_x\}^T\{\psi_x\}\right)\left(\{\psi_a\}^T\{\psi_a\}\right)} \tag{A.2}$$

The modal assurance criterion is normalized by the magnitude of vectors. Therefore, it is bounded between zero to one, representing no consistent correspondence and consistent correspondence respectively.

Similarly to modal analysis, in which the modal vectors from a finite element analysis can be compared and contrasted with those determined experimentally, a signal or combination of signals corresponding to undamaged areas of the specimen can be compared to waveforms obtained at each point of the scanning grid. In this manner, a MAC value close to unity may denote the absence of damage while a poor consistence may correspond to a damaged region.

The main drawback of this method is that undamaged regions with slight different thicknesses with respect to the nominal value may be identified as damaged areas, as low MAC values are compupted when position

of the back echo peaks are not coincident. To overcome this problem, reference signals are rescaled by a thickness correction factor that accounts for local specimen thickness in each point of the scanning grid, interpolated from thicknesses in reference points determined by means of the TOF method. In this manner, MAC with signal rescaling may provide accurate results even when the back echo peak cannot be easily identified within the stored waveforms, for instance, when damage size is smaller that the US probe diameter. However, through-the-thickness position of damage cannot be determined.

B-scans

B-scan representation on a selected cross-section may be obtained by correlating sample positions to spatial locations of signals acquired along the corresponding row/column of points of the scanning grid. At this aim, Equation (A.1) is employed.

Subsequently, these waveforms are represented on a bidimensional map, in which columns correspond to grid points along the inspected cross-section and rows represent sample points of their signals. This map evidences the location of the back echo peak as the spatial point where intensity of the reflection is maximum. In this manner, discontinuity surfaces such as damage, flaws or back surface are detected.

A.3 Ultrasonic analysis on a damaged CFRP plate

Inspected specimen consists of a rectangular 68x108mm CFRP plate, with a layup of $[0^o/90^o/45^o/-45^o]$ and a nominal thickness of 1mm. The panel was previously impacted and exhibits some damage, specially on the back side. The scanning grid was limited to a central window of 55x70mm around the damaged area.

TOF (Time-of-flight)

C-scan was firstly performed using the TOF method, whose representation is shown in Figure A.2.

A central damaged area which extends laterally and towards the back side of the specimen can be easily evidenced. Slight thickness variations with respect to the nominal value can be observed as well in undamaged regions around the upper and lower right corners of the specimen.

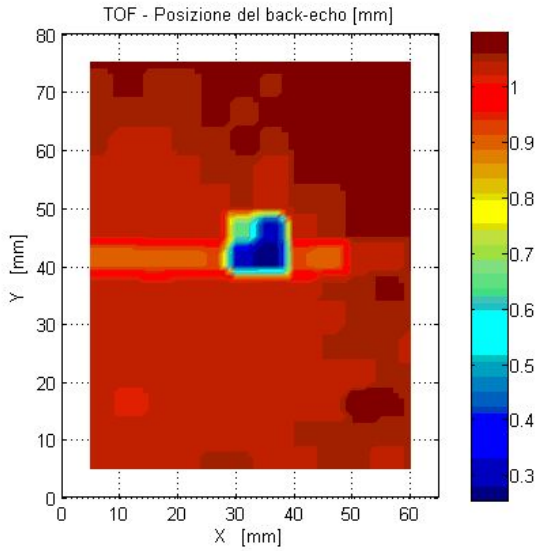

Figure A.2: C-scan obtained with the Time-of-Flight technique.

MAC (Modal Assurance Criterion)

C-scan obtained through the MAC without accounting for local variations of specimen thickness are displayed in Figure A.3a, which actually reports the value of (1-MAC) in each point of the scanning grid. Hence, values that approach unity denote a low consistency with the reference signals and, thus, may correspond to damaged areas.

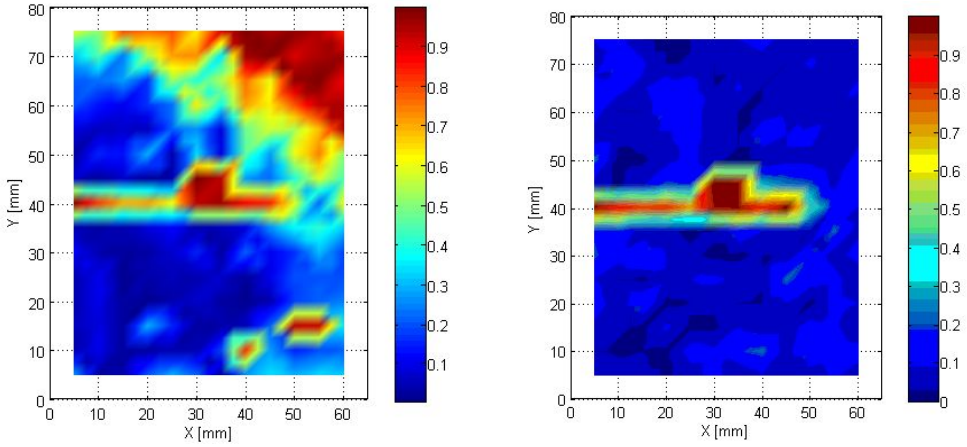

(a) *MAC.* (b) *MAC with signal rescaling.*

Figure A.3: C-scans obtained with MAC.

The previous TOF analysis showed that damage is confined around the central impact point and evidences that C-scan in Figure A.3a identifies wrongly as damaged regions some intact areas. This appears to happen in undamaged zones where local specimen thickness deviates from the nominal value.

Rescaling waveforms with the thickness correction factor, the representation depicted in Figure A.3b is obtained. In this manner, damaged areas are identified correctly and match well with preliminary TOF results. Nonetheless, unlike the TOF method, depth of damage cannot be determined.

B-scan

B-scans enable to evidence through-the-thickness location of damage on a selected cross-section. An example is shown in Figure A.4a, which corresponds to the cross-section along $y = 40mm$. B-scans may be used as well to detect local thickness variations in undamaged areas. Figure A.4b evidences this variations on the cross-section along $y = 10mm$.

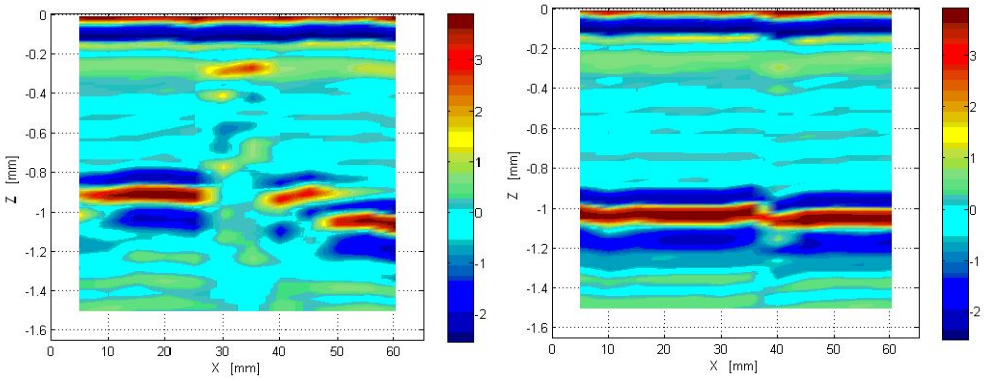

(a) *B-scan along* $y = 40mm$. (b) *B-scan along* $y = 10mm$.

Figure A.4: B-scans.

A.4 Ultrasonic analysis on an artificially damaged HTA/RTM6 NFC plate

Analyzed specimen consists of a 300x300mm HTA/RTM6 NFC (Non Crimp Fabric) plate with a stacking sequence of $[(0°/90°)_{4S}]$ and a nominal ply thickness of 0.25mm. The plate was supposed to be cut into four smaller

150x150mm plates that were to be subjected to a static compressive loading to track the growth of the initial artificial delamination. Each of these smaller plates, contains, in fact, a circular or elliptical Teflon insert located at a precise through-the-thickness location with the purpose to investigate the effect of delamination shape and depth on the compressive response.

Geometry of the HTA/RTM6 NFC plate is depicted in Figure A.5. The whole specimen and the US inspected area are shown in Figures A.6a and A.6b respectively.

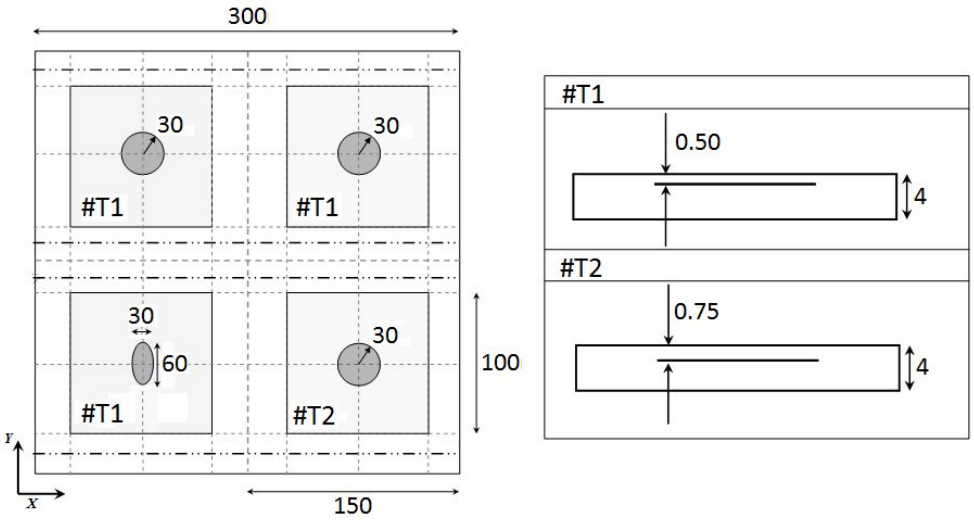

Figure A.5: Geometry of the HTA/RTM6 NFC plate.

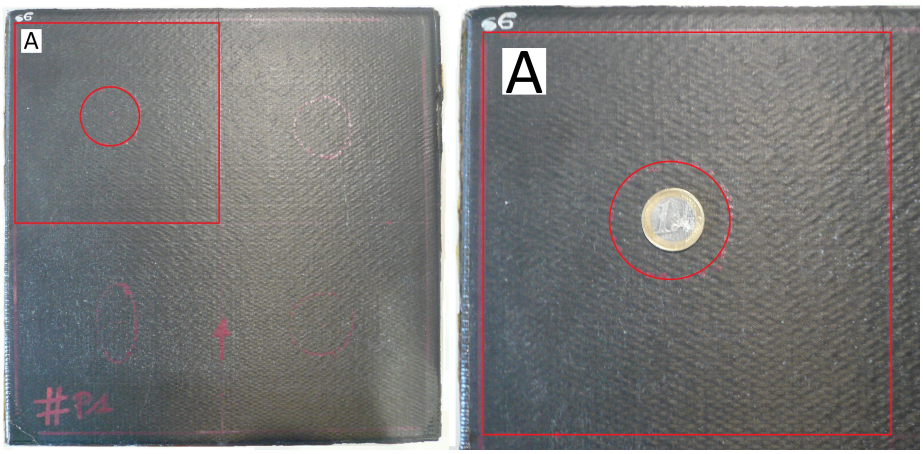

(a) *HTA/RTM6 NFC specimen.* (b) *US inspected area.*

Figure A.6: HTA/RTM6 NFC plate with artificial damage.

The scanning grid was defined on a 80x80mm region around the circular insert. C-scans obtained by means of the TOF and the MAC (accounting for the local thickness correction) are reported in Figures A.7a and A.7b respectively.

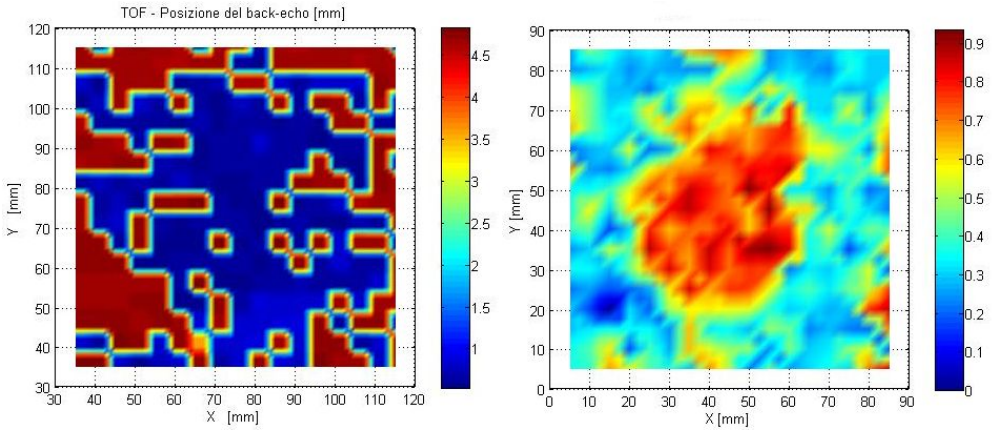

(a) *TOF.* (b) *MAC.*

Figure A.7: C-scans of the US inspected area (circular insert, depth = 0.5mm).

It can be noticed that circular embedded damage could not be accurately represented through C-scans. Manufacturer of the plates, in fact, admitted errors in the manufacturing process regarding the peel ply, whose large roughness prevented a stable contact of the US probe on the whole specimen surface and altered the acquired signals.

Bibliography

[1] http://www.flickr.com.

[2] R. Degenhardt, R. Rolfes, R. Zimmermann, and K. Rohwer. COCOMAT-Improved Material Exploitation at Safe Design of Composite Airframe Structures by Accurate Simulation of Collapse. *Journal of Composite Structures*, 73(2):175–178, 2006.

[3] N.J. Pagano and G.A. Schoeppner. Delamination of Polymer Matrix Composites: Problems and Assessment. In A. Kelly and C. Zweben, editors, *Comprehensive Composite Materials*, pages 433–528. Elsevier Science, Oxford, 2000.

[4] K. Schulte and W.W. Stinchcomb. Delamination of Polymer Matrix Composites: Problems and Assessment. In K. Friedrich, editor, *Application of Fracture Mechanics to Composite Materials*, volume 6 of *Composite Materials Series*, pages 273–325. Elsevier, 1989.

[5] G. Marom. Environmental Effects on Fracture Mechanical Properties of Polymer Composites. In K. Friedrich, editor, *Application of Fracture Mechanics to Composite Materials*, volume 6 of *Composite Materials Series*. Elsevier, 1989.

[6] J.A. Nairn. *Polymer Composites*, chapter 6, pages 123–120. 1985.

[7] M.J. Pavier and M.P. Clarke. Experimental Techniques for the Investigation of the Effects of Impact Damage on Carbon-Fibre Composites. *Composites Science and Technology*, 55:157–169, 1995.

[8] S.F. Hwang and G.H. Liu. Buckling Behavior of Composite Laminates with Multiple Delaminations Under Uniaxial Compression. *Composite Structures*, 53:235–243, 2001.

[9] A. Tafreshi and T. Oswald. Global Buckling Behaviour and Local Damage Propagation in Composite Plates with Embedded Delaminations. *International Journal of Pressure Vessels and Piping*, 80:9–20, 2003.

[10] C. Bisagni and P. Cordisco. Testing of Stiffened Composite Cylindrical Shells in the Postbuckling Range until Failure. *AIAA Journal*, 42(9):1806–1817, 2004.

[11] A.A. Griffith. The Phenomena of Rupture and Flow in Solids. *Philosophical Transactions of the Royal Society of London*, 221:163–198, 1921.

[12] G.P. Cherepanov. The propagation of Cracks in a Continuous Medium. *Journal of Applied Mathematics and Mechanics*, 31(3):503–512, 1967.

[13] J.R. Rice. A Path Independent Integral and the Approximate Analysis of Strain Concentration by Notches and Cracks. *Journal of Applied Mathematics and Mechanics*, 35:379–386, 1968.

[14] C. Fan, P.Y.B. Jar, and J.J.R. Cheng. Prediction of Energy Release Rates for Crack Growth Using FEM-based Energy Derivative Technique. *Engineering Fracture Mechanics*, 74(8):1243–1254, 2007.

[15] D.M. Parks. A Stiffness Derivative Finite Element Technique for Determination of Crack Tip Stress Intensity Factors. *International Journal of Fracture*, 10(4):487–502, 1974.

[16] G.R. Irwin. Fracture I. In S. Flügge, editor, *Handbuch der Physik VI*, pages 558–590. Springer, Berlin, 1958.

[17] R. Krueger. The Virtual Crack Closure Technique: History, Approach and Applications. *NASA/CR-2002-211628*, October 2002.

[18] M.F. Rybicki, E.F. abnd Kanninen. A Finite Element Calculation of Stress Intensity Factors by a Modified Crack Closure Integral. *Engineering Fracture Mechanics*, 9:931–938, 1977.

[19] K.N. Shivakumar, P.W. Tan, and J.C. Newman. A Virtual Crack-Closure Technique for Calculating Stress Intensity Factors for Cracked Three Dimensional Bodies. *International Journal Fracture*, 36:R43–R50, 1988.

[20] D.S. Dugdale. Yielding of Steel Sheets Containing Slits. *Journal of the Mechanics and Physics of Solids*, 8:100–104, 1960.

[21] G. Barenblatt. *Advances in Applied Mechanics*, chapter The Mathematical Theory of Equilibrium Cracks in Brittle Fracture, pages 55–129. III. Academic Press, 1962.

[22] H. Suemasu, W. Sasaki, T. Ishikawa, and Y. Aoki. A Numerical Study on Compressive Behavior of Composite Plates with Multiple Circular Delaminations considering Delamination Propagation. *Composites Science and Technlogy*, 68:2562–2567, 208.

[23] P.P. Camanho, C.G. Dávila, and S.T. Pinho. Fracture Analysis of Composite Co-Cured Structural Joints Using Decohesion Elements. *Fatigue Fract. Engng. Mater. Struct.*, 27:745–757, 2003.

[24] C. Fan, P.Y. Ben Jar, and J.J. Roger Cheng. Cohesive Zone with Continuum Damage Properties for Simulation of Delamination Development in Fibre Composites and Failure of Adhesive Joints. *Engineering Fracture Mechanics*, 75:3866–3880, 2008.

[25] P.P. Camanho, C.G. Dávila, and D.R. Ambur. Numerical Simulation of Delamination Growth in Composite Materials. *NASA-TP-211041*, 75, 2001.

[26] P.P. Camanho, C.G. Dávila, and M.F. de Moura. Numerical Simulation of Mixed-Mode Progressive Delamination in Composite Materials. *Journal of Composite Materials*, 37(16):1415–1438, 2003.

[27] Dassault Systèmes Simulia Corp. *Abaqus 6.9. Analysis User's Manual, Vol.4.*

[28] J. Schellekens and R. de Borst. A Nonlinear Finite-Element Approach for the Analysis of Mode-I Free Edge Delamination in Composites. *International Jourrnal of Solids and Structures*, 30(9):1239–1253, 1993.

[29] W. Cui, M.R. Wisnom, and M. Jones. A Comparison Failure Criteria to Predict Delamination of Unidiectional Glass/Epoxy Specimens Waisted Through the Thickness. *Composites*, 23(3):158–166, 1992.

[30] E.M. Wu and R.C. Reuter Jr. Crack Extension in Fiberglass Reinforced Plastics. T and M Report 275, University of Illinois, USA, 1965.

[31] M.L. Benzeggagh and M. Kenane. Measurement of Mixed-Mode Delamination Fracture Toughness of Unidirectional Glass/Epoxy Composites with Mixed-Modee Bending Apparatus. *Composite Science and Tecnology*, 56:439–449, 1996.

[32] J. Reeder, S. Kyongchan, P.B. Chunchu, and R. Ambur. Postbuckling and Growth of Delaminations in Composite Plates

Subjected to Axial Compression. Technical report, 43rd AIAA/ASME/ASCE/AHS/ASC Structures, Structural Dynamics, and Materials Conference, Denver, Colorado, 2002.

[33] J.R. Reeder. An Evaluation of Mixed-Mode Delamination Failure. *NASA-TM-104210*, 1992.

[34] J.K. Li, J. ad Sen. Analysis of Frame-to-Skin Joint Pull-Off Tests and Prediction of the Delamination Failure. Technical report, 42nd AIAA/ASME/ASCE/AHS/ASC Structures, Structural Dynamics and Materials Conference, Seattle,WA, USA, 2000.

[35] M.L. Benzeggagh and M. Kenane. Three-Dimensional Effects in the Prediction of Flange Delamination in Composite Skin-Stringer Debonding Under Multi-Axial Loading. *Journal of Composite Materials*, 23(15):1263–1300, 2000.

[36] A. Turon, P.P. Camanho, J. Costa, and C.G. Dávila. A Damage Model for the Simulation of Delamination in Advanced Composites under Variable-Mode Loading. *Mechanics of Materials*, 38:1072–1089, 2006.

[37] J.R. Reeder and J.R. Crews. Mixed-Mode Bending Method for Delamination Testing. *AIAA Journal*, 28:1270–1276, 1990.

[38] ASTM International. *Standard Test Method for Mode I Interlaminar Fracture Toughness of Unidirectional Fiber-Reinforced Polymer Matrix Composites, ASTM D5528-01e3*, 2007.

[39] J.R. Reeder, K. Demarco, and K.S. Whitley. The Use of Doubler Reinforcement in Delamination Toughness Testing. *Composites: Part A*, 35:1337–1344, 2004.

[40] J.G. Williams. The Fracture Mechanics of Delamination Tests. *J. Strain. Anal. Eng. Des.*, 24:207–214, 1989.

[41] F.A. McKlintock and G.R. Irwin. Plasticity Aspects of Fracture Mechanics. In *Fracture Toughness Testing and its Applications*, pages 84–113. ASTM STP 381, 1965.

[42] M. Wang, W-X.and Nakata, Y. Takao, and T. Matsubara. Experimental Investigation on Test Methods for Mode II Interlaminar Fracture Testing of Carbon Fiber Reinforced Composites. *Composites*, A: 40:1447–1455, 2009.

[43] Japanese Industrial Standards. *Testing Methods for Interlaminar Fracture Toughness of Carbon Fibre Reinforced Plastics, JIS K7086*, 1993.

[44] K. Kageyamaa, M. Kikuchi, and N. Yanagisawa. Stabilized End Notched Flexure Test Characterization of Mode II Interlaminar Crack Growth. *ASTM STP 1110*, pages 210–225, 1991.

[45] D.R. Moore, A. Pavan, and J.G. Williams. *Fracture Mechanics Testing Methods for Polymers, Adhesives and Composites*. Elsevier Science Ltd. ESIS Publication 28, 2001.

[46] K. Tanaka, T. Yuasa, and K. Katsura. Continuous Mode II Interlaminar Fracture Toughness Measurement by Over Notched Flexure Test. In *Proceedings of the 4th European Conference on Composites: Tessting and Stadardisation*, pages 171–179, Lisbon, Portugal, 1998.

[47] R.H. Martin and B.D. Davidson. Mode II Fracture Toughness Evaluation using a Four Point Bend End Notched Flexure Test. In *Proceedings of the 4th International Conference on Deformation and Fracture of Composites*, pages 243–253, Manchester, 1997.

[48] ASTM International. *Standard Test Method for Mixed Mode I-Mode II Interlaminar Fracture Toughness of Unidirectional Fiber-Reinforced Polymer Matrix Composites, ASTM D 6671/D 6671M*, 2006.

[49] J.R. Reeder and J.H. Crews Jr. Refinements to the Mixed-Mode Bending Test for Delamination Toughness. In *Proceedings of the American Society for Composites-Fifteenth Technical Conference*, Texas, USA, 2000.

[50] L. Hamitouche, M. Tarfaoui, and A. Vautrin. Modélisation du Délaminage par la Méthode de la Zone Cohésive et Problèmes d'Instabilité. *JNC*, 16, 2009.

[51] A. Turon, C.G. Dávila, P.P. Camanho, and J. Costa. An Engineering Solution for Mesh Size Effects in the Simulation of Delamination Using Cohesive Zone Models. *Engineering Fracture Mechanics*, 74(10):1665–1682, 2007.

[52] J. Rice. *The Mechanics of Earthquake Rupture*, chapter Physics of the Earth's interior, pages 555–649. Italian Physical Society and North-Holland Pub. Co., 1980.

[53] A. Hillerborg, M. Modéer, and P.E. Petersson. Analysis of Crack Formation and Crack Growth in Concrete by means of Fracture Mechanics and Finite Elements. *Cement and Concrete Research*, 6:773–782, 1976.

[54] C. Balzani and W. Wagner. An Interface Element for the Simulation of Delamination in Unidirectional Fiber-Reinforced Composite Laminates. *Engineering Fracture Mechanics*, 75:2597–2615, 2008.

[55] K.-F. Nilsson, L.E. Asp, J.E. Alpman, and L. Nystedt. Delamination Buckling and Growth for Delaminations at Different Depths in a Slender Composite Panel. *International Journal of Solids and Structures*, 38:3039–3071, 2001.

[56] M. Juntti, L. Asp, and R. Olsson. Assessment of Evaluation Methods for the Mixed-Mode Bending Testing. *Journal of Composites Techonology and Research*, 21:37–48, 1999.

[57] A. Turon, J. Costa, P.P. Camanho, and C.G. Dávila. Simulation of Delamination in Composites under High-Cycle Fatigue. *Composites:Part A*, 38:2270–2282, 2007.

[58] ASTM International. *Standard Test Method for Compressive Residual Strength Properties of Damaged Polymer Matrix, ASTM D 7137/D 7137M-07*, 2007.

[59] ASTM International. *Standard Test Method for Measuring the Damage Resistance of a Fiber-Reinforced Polymer-Matrix Composite to a Concentrated Quasi-Static Indentation Force, ASTM D 6264/D 6264M-07*, 2007.

[60] ASTM International. *Standard Test Method for Measuring the Damage Resistance of a Fiber-Reinforced Polymer Matrix Composite to a Drop-Weight Impact Event, ASTM D 7136/D 7136M-07*, 2007.

[61] http://www.wyomingtestfixtures.com.

[62] M.J. Pavier, G.J. Short, and F.J. Guild. The Effect of Delamination Geometry on the Compressive Failure of Composite Laminates. *Composites Science and Technology*, 61:2075–2086, 2001.

[63] Mezzanzanica, D. Indagini ad Ultrasuoni per l'Analisi di Danneggiamenti nei Materiali Compositi. Master's thesis, Politecnico di Milano, 2009.